Relative Orbit Propagation and Control for Satellite Formation Flying using Continuous Low-thrust
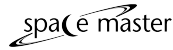
Eric Reinthal

Space Engineering, masters level (120 credits)
2017

Luleå University of Technology
Department of Computer Science, Electrical and Space Engineering

LULEÅ
UNIVERSITY
OF TECHNOLOGY

JULIUS-MAXIMILIANS-UNIVERSITÄT WÜRZBURG

LULEÅ UNIVERSITY OF TECHNOLOGY

spa**C**e master

MASTER'S THESIS

Relative orbit propagation and control for satellite formation flying using continuous low-thrust

---

Author:
Eric REINTHAL

Supervisor:
Julian SCHARNAGL

Examiner:
Prof. Dr. Klaus SCHILLING
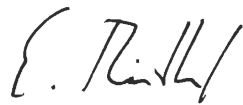Dr. Johnny EJEMALM

November 15, 2016

Abstract

For the upcoming formation flying technology demonstration mission *NetSat* a relative orbit propagator as well as a relative orbit controller were developed The formation will consist of four equal nano-satellites with an electric propulsion system for orbit correction manoeuvres. This demands the use of continuous low-thrust models for relative orbit control, which is a novel field. A software framework was developed which allows orbit simulations of the whole fleet in a fully non-linear environment. The final on-board relative propagator is based on the Gim-Alfriend STM and incorporates eccentricity and the non-spherical shape of the Earth. The controller uses control Lyapunov function-based design and model predictive control, depending on the task. The guidance and control system is able to safely govern the relative motion for one-, two- and three-dimensional formation configurations with inter-satellite distances as low as $50\,\mathrm{m}$. Based on these results, a complete mission plan is proposed.

Declaration of Authorship

I, Eric Reinthal, declare that the work in this Master's thesis was carried out in accordance with the requirements of the regulations of both universities and code of practice for research degree programmes and that it has not been submitted for any other academic award. Except where indicated by specific reference in the text, the work is the candidate's own work. Work done in collaboration with, or with the assistance of, others is indicated as such. Any views expressed in this thesis work are those of the author.

Signed:

Date: November 15, 2016

Contents

List of Figures

List of Tables

List of Abbreviations

ARE	**A**lgebraic **R**iccati **E**quation
ATF	**A**long **T**rack **F**ormation
CLF	**C**ontrol **L**yapunov **F**unction
CLT	**C**ontinuous **L**ow **T**hrust
COE	**C**lassical **O**rbital **E**lements
CWF	**C**art**w**heel **F**ormation
DEM	**D**igital **E**levation **M**odel
DOE	**D**ifferential **O**rbital **E**lements
ECI	**E**arth-**C**entred **I**nertial coordinate system
EME2000	same as J2000
EOE	**E**quinoctial **O**rbital **E**lements
GA	**G**im-**A**lfriend
GPS	**G**eneral **P**ositioning **S**ystem
GTO	**G**eostationary **T**ransfer **O**rbit
HCW	**H**ill-**C**lohessy-**W**iltshire
IP	**I**n-**P**lane (motion)
J2000	common ECI definition
LCF	**L**yapunov **C**ontrol **F**unction
LEO	**L**ow **E**arth **O**rbit
LQR	**L**inear **Q**uadratic **R**egulator
LTI	**L**inear **T**ime-**I**nvariant
LVLH	**L**ocal-**v**ertical local-**h**orizontal coordinate system
MIMO	**M**ultiple-**I**nput **M**ultiple-**O**utput
MOEA	**M**ulti-**O**bjective **E**volutionary **A**lgorithm
MPC	**M**odel **P**redictive **C**ontrol
NOE	**N**on-singular **O**rbital **E**lements
ODE	**O**rdinary **D**ifferential **E**quation
OOP	**O**ut-**O**f-**P**lane (motion)
PCO	**P**rojected **C**ircular **O**rbit
PV	**P**ostion-**V**elocity vector
RK	**R**unge-**K**utta
ROE	**R**elative **O**rbital **E**lements
RTN	**R**adial-**T**angential-**N**ormal coordinate system
SEZ	**S**outh-**E**ast-**N**ormal coordinate system (topocentric-horizon)
STM	**S**tate-**T**ransition **M**atrix
TAI	International Atomic Time (**T**emps **A**tomique **I**nternational)
TH	**T**schauner-**H**empel

TT	**T**errestrial **T**ime
UTC	**U**niversal **T**ime **C**oordinated
YA	**Y**amanaka-**A**nkerson
ZOH	**Z**ero-**O**rder **H**old

List of Symbols

$(\cdot)_0$	subscript for chief satellite's coordinates	
$(\cdot)_1$	subscript for deputy satellite's coordinates	
$\dot{\ }$	first derivative w.r.t. time	
$\ddot{\ }$	second derivative w.r.t. time	
$(\cdot)'$	first derivative w.r.t. true anomaly	
$(\cdot)''$	second derivative w.r.t. true anomaly	
a	semi-major axis	m
$\mathbf{a}$	state vector (orbital frame)	
$\bar{\mathbf{a}}$	mean state (orbital frame)	
d	distance	m
$\mathbf{D}$	mean-to-osculating partial derivative matrix	
e	eccentricity	
f	true anomaly	rad
$\mathbf{h}$	angular momentum vector	$\mathrm{kgm^2/s}$
$\mathscr{H}$	Hill frame	
$\mathfrak{H}$	Hamiltonian	
i	inclination	rad
$\mathbf{I}$	Identity matrix	
$\mathbf{J}$	Jacobian matrix	
J_2	Earth oblatness factor	
	(WGS84, $-1.082\,626\,683\,553\,15 \times 10^{-3}$)	
$\mathscr{I}$	ECI frame	
$\mathscr{L}$	LVLH frame	
$\mathfrak{L}$	Lagrangian	
M	mean anomaly	rad
n	mean motion	s^{-1}
p	semi-latus rectum	m
$\mathbf{p}$	conjugate momenta	
$\mathbf{q}$	generalised position coordinates	
$\mathbf{r}$	position vector	m
R_E	Equatorial radius of the Earth	
	(GRS80, $6.378\,137 \times 10^6\,\mathrm{m}$)	
T_O	orbital period	s
u	mean argument of latitude	rad
$\mathbf{v}$	velocity vector	$\mathrm{m\,s^{-1}}$

xviii

$\mathbf{x}$	state vector (Cartesian frame)	m
$\delta\mathbf{a}$	state vector (differential orbit)	
$\delta\mathbf{o}$	state vector (relative orbit)	
ϵ	perturbation factor	
η	eccentricity dependent factor	
θ	true argument of latitude	rad
λ	mean longitude	rad
μ	Earth gravitational parameter $(3.986\,004\,418 \times 10^{14}\,\text{m}^3\text{s}^{-2})$	
$\boldsymbol{\Phi}$	state transition matrix	
ω	argument of perigee	rad
Ω	right ascension of ascending node	rad
$\dot{\boldsymbol{\Omega}}$	angular velocity vector	m s^{-1}

Chapter 1

Introduction

A paradigm shift is emerging in spacecraft engineering from single and large multi-functional satellites towards cooperating groups of small satellites, forming a constellation, cluster or formation. This will enable innovative approaches in areas like Earth observation, scientific exploration or telecommunication. This introduction covers the history of satellite formation flying and the benefits of using this technology over single satellites. This is followed by a presentation of the *NetSat* mission. The chapter closes with an outline for the thesis.

1.1 From constellations to formations

Walker (1984) provided the first mathematical description for placing spacecraft in different orbits around the Earth. The so called Walker-constellation places multiple satellites in each orbit, while the different orbital planes are inclined against each other. By this, an almost global coverage (except the pole regions) may be obtained with a minimal number of satellites. Early use of the Walker-constellation was made by the first global navigation satellite system GPS, which consisted of ten spacecraft in its first phase (Green, Massatt, and Rhodus, 1989). Other applications are satellite-based voice and data transfer around the world, which is provided by the constellations Iridium (Maine, Devieux, and Swan, 1995) and Globalstar (Smith, 1996). In contrast to constellations, the satellites in a cluster or formation are closer together. One of the first mission concepts (including an early controller design) that makes relevant use of a satellite formation in orbit is a proposed infra-red space interferometer by Sholomitsky (1977). A satellite cluster consists of multiple spacecraft, which are placed in similar orbits, maintaining a bounded relative motion. A notable mission in this field is ESA's first cornerstone project Cluster-II, which was finally launched in the year 2000 after a failed start in 1996 (Escoubet, Fehringer, and Goldstein, 2001). The tetrahedron cluster consists of four spacecraft with inter-satellite distances between 100 and $2000\,\mathrm{km}$ and measures the magnetic field of the Earth. The use of a cluster in this field of research enables spatially distributed measurements at the same time, since the magnetic field can only be measured in-situ. The distinction to a satellite formation lies in the nature of the orbit control. While in the cluster each spacecraft is controlled individually to a certain absolute orbit, the satellites of a formation are controlled relative to each other. Although the whole

formation may be controlled to follow a certain absolute orbit, main focus is directed to autonomously maintain or reconfigure the relative states between the satellites. Satellite formations are an emerging field of research and not many missions have been flown up to today. A comprehensive introduction to distributed space missions with an emphasis on formations is given in D'Errico (2013). One of the first two-satellite formations was GRACE, a joint mission of DLR and NASA (Kirschner, Massmann, and Steinhoff, 2013). They maintain a relative distance of $220\,\text{km}$ in the same orbit and measure the gravity field of the Earth. A further noteworthy formation is DLR's TanDEM-X mission, which extended the single-satellite TerraSAR-X mission to a two-satellite formation in 2010. The two satellites maintain a relative distance of $200\,\text{m}$ to sub-meter accuracy and created a digital elevation model of the Earth with unprecedented resolution and precision. It is a leader-follower formation, where only the second satellite actively maintains the relative state (Ardaens et al., 2008). The first small- and pico-satellite formations are the technology demonstrator missions Prisma (D'Amico, Gill, and Montenbruck, 2006) and CanX-4&5 (Bonin et al., 2015). They also consisted of two satellites and tested new propulsion techniques as well as novel navigation and relative control algorithms.

A key element of successful formation flying missions is the ability to accurately maintain or alter the inter-satellite distances. Relative orbit control was firstly developed for automated on-orbit rendezvous. Substantial progress in docking manoeuvres was accomplished by Soyuz (Polites, 1999) and the Space Shuttle (Goodman, 2006) approaching a space station. The mathematical distinction to satellite formations is the ultimate relative state vector, which evaluates to zero for rendezvous manoeuvres. This terminal approach is similar, but not equal, to formation-hold and -reconfiguration manoeuvres. As rendezvous is a well-studied field with more sophisticated analyses compared to satellite formations, some conclusions turn out to be helpful for formation flying. Sengupta (2007) provides an analysis of rendezvous under the influence of perturbations. In this kind of manoeuvres, the relative non-spherical influence of the Earth vanishes in the terminal manoeuvre phase due to (almost) equal state vectors of the spacecraft. Results of the relative orbit control method used in the early formation mission Prisma give insight into real mission data (D'Amico, Ardaens, and Montenbruck, 2009), (D'Amico, 2010). Although a double impulsive thrust scheme is used there, one can draw conclusions about the order of magnitude of thrust needed to perform reconfiguration manoeuvres in a real environment. This control scheme, which initially used the Hill-frame, was later extended to use state vectors consisting of relative orbital elements by D'Amico, Ardaens, and Larsson (2011).

Difficulties of satellite formation flying emerge from the need for very accurate relative position and velocity data. For very close formations, radar-based tracking and position estimation for the single satellites may become infeasible, since all spacecraft may return a single echo. This can be overcome with GNSS receivers on-board the satellites. Furthermore, inter-satellite communication has to be provided to exchange relative state

vectors, when the formation should maintain its configuration autonomously. It is especially challenging to accommodate all this technology in nano-satellites with an edge length of around $10 \, \text{cm}$. Another design goal of small satellites designated for formation flying is to have the same ballistic coefficient for all spacecraft, which also includes the need for fuel balancing among the fleet. Otherwise, the satellites are differently influenced by atmospheric drag and may drift apart.

An important benefit of using formations instead of single large satellites is the increased temporal and spatial resolution, which distributed spacecraft can provide. This is advantageous for research fields which require in-situ measurements (e.g. magnetic field measurements) or different viewing angles at a common target at the same time (e.g. 3D images of the Earth). Beyond this, single-satellite failures or launch fails of a part of satellites do not result in total mission loss. For many applications, the concept of graceful degradation can be used. For example, a formation resembling a synthetic aperture radar (SAR) suffers from resolution decrease when single satellites cease to work, but is still operable. These single satellites can even be replaced at much lower cost, compared to single-satellite missions. If demanded, a SAR array could also be extended in orbit with additional satellites, which increases total resolution. When using many equal satellites, they may be produced in an assembly line. This could lower expenses compared to multi-million dollar singleton spacecraft.

1.2 The *NetSat* mission

NetSat is a satellite formation mission by Zentrum für Telematik e.V. (Germany). It will consist of four equal nano-satellites and is tentatively scheduled to be launched in the period 2017/2018. This technology demonstration mission is enabled by the outcomes of the preceding UWE missions, University of Würburg's series of nano-satellites. It started with UWE-1 in 2005, which examined internet-based communication in space and tested novel solar arrays (Barza, Aoki, and Schilling, 2006). The follow-up mission, UWE-2, verified new attitude determination methods in orbit (Schmidt et al., 2008). The still operational satellite UWE-3, started in 2013, is the first one in the series which is equipped with active attitude control (Busch, Bangert, and Schilling, 2014). The next start is planned for the first quarter of 2017 with UWE-4, which will be equipped with active attitude and orbit control. This is a cornerstone for the subsequent *NetSat* mission, which will demonstrate novel autonomous relative orbit determination and control techniques. *NetSat* will be the first-ever formation mission using continuous low-thrust for orbit control. Planned are reconfiguration and maintenance manoeuvres in one-, two- and three-dimensional configurations. Expectations on the mission include contributions to the fields on-board autonomy, distributed formation control, relative navigation, inter-satellite communication, and miniaturised attitude and orbit control systems. The electric propulsion system, which will provide a total control force in the order of magnitude of $1 \times 10^{-5} \, \text{N}$, will be tested on-board the upcoming UWE-4 satellite. The inter-satellite separation will be in the range from $100 \, \text{km}$ down to the distance

permitted by the relative navigation and control system. An initial guess on required accuracies is given in table 1.1, which states the expected relations between the different GNC parts (Schilling et al., 2009).

TABLE 1.1: Scaling laws for GNC systems in satellite formation flying.

Parameter	Variable/Relation	Sample Scenario
Spacecraft separation	d_1	$5\,\text{km}$
Control window size	$d_{cw} = d_1 \cdot 10^{-1}$	$500\,\text{m}$
Control accuracy requirement	$\sigma_c = d_{cw} \cdot 10^{-1}$	$50\,\text{m}$
Navigation accuracy requirement	$\sigma_n = \sigma_c \cdot 10^{-1}$	$5\,\text{m}$

The characteristics of the *NetSat* satellites will mainly match the design of UWE-4, a $1.3\,\text{kg}$ cubesat with $10\,\text{cm}$ edge length. The electric propulsion system for orbit manoeuvres will likely provide a maximum thrust of

$$c_{max} = 7.9 \times 10^{-6}\,\text{N} \tag{1.1}$$

in one direction. For the given weight, the satellite is able to produce a maximum control acceleration of

$$u_{max} = 6.07 \times 10^{-6}\,\text{m}\,\text{s}^{-2} \tag{1.2}$$

The total delta-v for the planned amount of fuel is limited to $30\,\text{m}\,\text{s}^{-1}$. The absolute orbit of the satellites, as for all cubesat missions, will be determined by the launch system provider, where the cubesats are the piggyback payload. Presumably, this orbit will be similar to that of UWE-3, which is given in table 1.2. This orbit will be used as an absolute reference for most of the calculations in this work.

TABLE 1.2: UWE-3 Kepler elements at 2016-5-1 UTC00:00.

Parameter	Value
semi-major axis	$7014.5\,\text{km}$
eccentricity	$0.007\,20$
inclination	$1.705\,\text{rad}$
argument of perigee	$0.7892\,\text{rad}$
right ascension of ascending node	$1.906\,\text{rad}$
true anomaly	$0.1542\,\text{rad}$

This technology demonstration mission will be the base for the planned follow-up *NetSat* SPG (StereoPhotoGrammetry) mission. It shall provide three-dimensional pictures of the Earth in the visible and thermal IR-spectrum. Especially the research areas of volcanology, geology, cartography and meteorology could benefit from the mission outcomes. Also the prediction and monitoring of natural disasters may be facilitated with data from the *NetSat* SPG mission (Schilling et al., 2015).

1.3   Scope of this work

The main task of this work is to assess different relative navigation and control techniques, which could be used on-board the *NetSat* satellites. Existing relative GNC techniques may be adapted to match the requirements of the mission. For relative control, focus is directed to the given constraints of an electric propulsion system. Promising relative GNC systems should be implemented in a to-be-developed software framework. This framework shall feature a complete satellite model as well as accurate orbit simulations with realistic perturbation forces. With this, it has to be ascertained, if the desired formation geometries are possible with the given constraints of the satellites. Furthermore, control strategies should be developed with regard to the power system (limiting the thruster duty-cycle per orbit) and the satellites' attitude systems. The power system, which is yet to be defined, is assumed to provide thruster power for roughly half an orbit per orbit. The thrusters, which provide the combined control force stated in equation (1.1), are directed in the same direction. This means, the attitude of a satellite during controlled phases is restricted to the needs of the relative orbit controller. Other tasks may also need a certain attitude, for what reason active control intervals have to be limited. For example, the inter-satellite communication system likely will use directed antennas. A favourable final result of the thesis would be a mission plan, which incorporates all possible formation types to be flown. Attitude and absolute orbit control are not part of this work and developed simultaneously for the *NetSat* mission.

1.4   Thesis outline

Chapter 2 investigates the theoretical background for relative navigation and control. Existing work in this field is examined and rated in applicability for the *NetSat* mission. It contains discussions on coordinate frames, relative motion description, perturbation forces, and finally orbit propagation and relative orbit control. Chapter 3 illuminates different types of possible formation to be flown, from a one-dimensional along-track configuration to the three-dimensional cartwheel formation. The developed software framework is presented in chapter 4. It comprises the developed satellite model, the configuration databases, the realistic orbit propagator and an extensible debug interface. The implemented on-board relative orbit propagators are described in detail in chapter 5. This is followed by the implementation details of the relative orbit controllers in chapter 6. Different techniques are compared and a final solution is presented. The work is closed by the conclusion in chapter 7, which provides a preliminary mission plan and suggestions for further work.

Chapter 2

Theoretical background

This chapter will introduce the basics of relative spacecraft motion to the reader. Essential coordinate frames as well as relative equations of motion are presented. After that, linearised equations of motion are developed and controllers based on these linearised propagator equations are discussed. In this work the time derivative of a vector will be denoted by (˙) and the second time derivative by (¨). Vectors will be denoted by bold lower case letters ($\mathbf{v}$) and matrices by bold upper case letters ($\mathbf{M}$). A six-field column vector consisting of concatenated position ($\mathbf{r}$) and velocity ($\mathbf{v}$) vectors of a certain satellite will be called $\mathbf{pv}$-vector:

$$\mathbf{pv} = \begin{pmatrix} \mathbf{r} \\ \mathbf{v} \end{pmatrix} \tag{2.1}$$

Focus of concern will be directed to bounded relative motion of the satellites, which gives a stable formation. Although any two Keplerian orbits (around the same central body) result in a globally bounded motion, only orbits with a commensurable orbital period T_O (e.g. same semi-major axis a) give a locally bounded motion. If the orbital periods are different, the relative motion is quasi-periodic with the least common multiple of the two periods. This renders the local relative motion unbounded and stable formation design is impossible.

A formation consists of one reference (or chief) satellite and multiple deputy satellites. When all satellites need to be treated equally, a virtual chief satellite will be introduced. This virtual chief will be located at the geometric centre of the whole formation.

2.1   Coordinate frames

The coordinate frames used to describe the state of a satellite can be distinguished by their inherent setup into two groups, Cartesian and orbital frames. This section will introduce these frames and the reasoning on using either one in a particular use case. Furthermore, each group is divided into global frames, which describe the absolute state of a satellite, and local frames, which describe the relative states between multiple satellites of a formation.

2.1.1   Cartesian frames

To describe the relative motion of two or more satellites, an inertial and a local coordinate system are needed. The state vector in the inertial system, which is fixed to the Earth, describes the absolute motion of a satellite with respect to the Earth. The local frame is fixed to the formation and thus able to describe the relative distances and velocities between the satellites.

Inertial frame

The inertial frame used throughout this work is the Earth-centred inertial (ECI) coordinate system. It will be denoted with the symbol $\mathscr{I}$. This geocentric frame is defined through the equatorial plane of the Earth with $\hat{\mathbf{X}}$ pointing to the vernal equinox, $\hat{\mathbf{Z}}$ being normal to the fundamental plane and pointing to the north pole and $\hat{\mathbf{Y}}$ completing a positive triad (see figure 2.1). The state vector of a satellite in this frame is defined by:

$$\mathbf{x} = \begin{pmatrix} x & y & z & v_x & v_y & v_z \end{pmatrix}^T = \begin{pmatrix} x & y & z & \dot{x} & \dot{y} & \dot{z} \end{pmatrix}^T \tag{2.2}$$

with position $\mathbf{r} = (x\ y\ z)^T$, velocity $\mathbf{v} = (\dot{x}\ \dot{y}\ \dot{z})^T$ and distance from the centre of the Earth $r = ||\mathbf{r}|| = \sqrt{x^2 + y^2 + z^2}$. The angular momentum of the satellite, which is normal to the position and the velocity vector, is defined by (Chobotov, 2002):

$$\mathbf{h} = \mathbf{r} \times \dot{\mathbf{r}} \tag{2.3}$$

The reference for the ECI frame will be the J2000 (or EME2000) definition. It corresponds, in accordance with the definition above, to Earth's mean equatorial plane at 12:00 Terrestrial Time (TT) on 1 January 2000 (Montenbruck and Gill, 2012).

Local frame

The local frame $\mathscr{L}$ of a satellite has its origin in the satellite's centre of mass. The fundamental plane of this local-vertical local-horizontal (LVLH) frame will be defined through the orbital plane of the satellite. $\hat{\mathbf{e}}_\mathbf{x}$ points radially outward (seen from the centre of the Earth), $\hat{\mathbf{e}}_\mathbf{z}$ is normal to the orbital plane (positive in the direction of the orbit's angular momentum) and $\hat{\mathbf{e}}_\mathbf{y}$ completes a positive triad (see figure 2.1). This rotating frame moves with the satellite and is sometimes referred to as RTN-frame (for radial, tangential, normal). When a deputy satellite is viewed in the chief's $\mathscr{L}$-frame, the frame is called Euler-Hill-frame $\mathscr{H}$ (or Hill-frame for brevity). Although the $\mathscr{L}$- and $\mathscr{H}$-frame of a deputy are very similar in terms of orientation for close formations, this distinction renders pretty useful for later analysis. While the $\mathscr{L}$-frame of a deputy depicts the true transformation w.r.t. the $\mathscr{I}$-frame, the satellite's state in the $\mathscr{H}$-frame will always have small errors induced through using a reference at a slightly different position (e.g. the position offset between chief and deputy). However, all satellites of a formation share the same $\mathscr{H}$-frame, which is essential for relative motion models. By
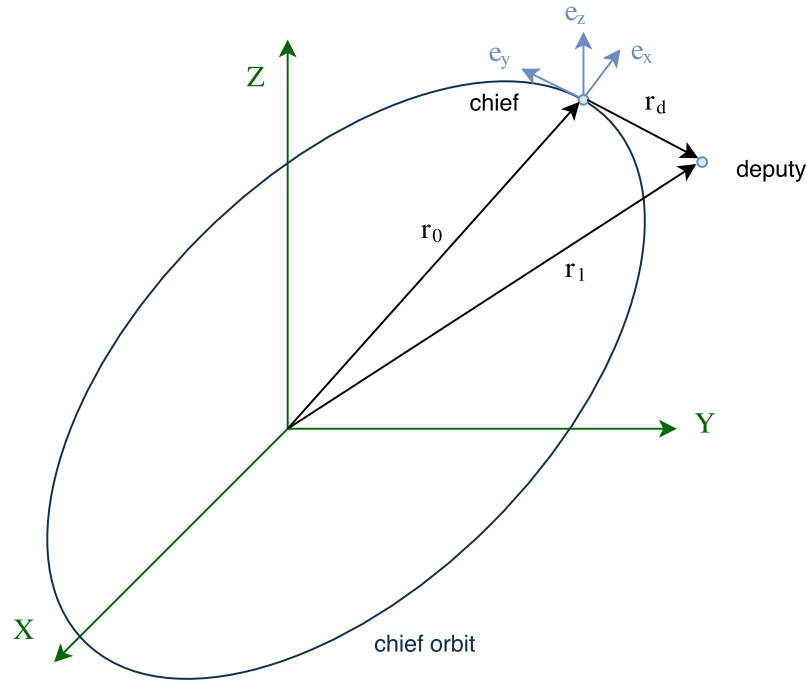
FIGURE 2.1: Cartesian inertial and local coordinate frames. ECI is
depicted in green, LVLH of the chief in blue.

definition of the Hill-frame, $\mathscr{L} \hat{=} \mathscr{H}$ holds for the (virtual) chief and it will always be located at $\mathbf{r}^{\mathscr{H}} = (0 \ 0 \ 0)^T$. When mapping between ECI, orbital elements and $\mathscr{H}$ the Hill-frame has a satisfactory level of accuracy only for low-eccentric chief orbits ($e << 1$) and close formations (relative distances between the satellites smaller than $\sim 100\,\mathrm{km}$). Thus, whenever mapping into the Hill-frame is applied, the just mentioned constraints are assumed to be satisfied (Alfriend et al., 2010).

Transformation between ECI and Euler-Hill-frame

Let $\mathbf{r_0}$ be the position vector of the chief satellite and $\mathbf{v_0}$ its velocity. The origin of the $\mathscr{H}$-frame viewed in the $\mathscr{I}$-frame is therefore at $\mathbf{r_0}$. The rotation vector between the two frames will be denoted by $\mathbf{\Omega}$ (with $\dot{\mathbf{\Omega}}$ being the angular velocity of $\mathscr{H}$ relative to $\mathscr{I}$). The **pv**-vector of another satellite (called deputy or chaser spacecraft) consists of $\mathbf{r_1}$ and $\mathbf{v_1}$. The 3×3 direction cosine matrix $\mathbf{C}$ between the $\mathscr{H}$- and the $\mathscr{I}$-frame can be computed as follows (Nicholas, 2013):

$$\hat{\mathbf{e}}_{\mathbf{x}}^{\mathscr{L}} = \frac{\mathbf{r_0}^{\mathscr{I}}}{||\mathbf{r_0}||^{\mathscr{I}}} \tag{2.4a}$$

$$\hat{\mathbf{e}}_{\mathbf{z}}^{\mathscr{L}} = \frac{\mathbf{r_0}^{\mathscr{I}} \times \mathbf{v_0}^{\mathscr{I}}}{||\mathbf{r_0} \times \mathbf{v_0}||^{\mathscr{I}}} \tag{2.4b}$$

$$\hat{\mathbf{e}}_{\mathbf{y}}^{\mathscr{L}} = \hat{\mathbf{e}}_{\mathbf{z}}^{\mathscr{L}} \times \hat{\mathbf{e}}_{\mathbf{x}}^{\mathscr{L}} \tag{2.4c}$$

$$\mathbf{C} = \left[\begin{array}{ccc} \hat{\mathbf{e}}_{\mathbf{x}}^{\mathscr{L}} & \hat{\mathbf{e}}_{\mathbf{z}}^{\mathscr{L}} & \hat{\mathbf{e}}_{\mathbf{y}}^{\mathscr{L}} \end{array} \right]^{T} \tag{2.5}$$

Note that the direction cosine matrix $\mathbf{C}$ can be used to translate ECI coordinates to any satellite's LVLH-frame by using its corresponding $\mathbf{pv}$-vector. The position and velocity difference between the chief and the deputy satellite will be:

$$\mathbf{pv_d} = \left(\begin{array}{c} \mathbf{r_d} \\ \mathbf{v_d} \end{array} \right) = \left(\begin{array}{c} \mathbf{r_1} - \mathbf{r_0} \\ \mathbf{v_1} - \mathbf{v_0} \end{array} \right) \tag{2.6}$$

For the deputy's $\mathbf{pv}$-vector in the $\mathscr{H}$-frame follows with the theorem of rotating reference frames:

$$\mathbf{p} = \left(\begin{array}{c} x \\ y \\ z \end{array} \right) = \mathbf{r_d}^{\mathscr{H}} = \mathbf{C r_d}^{\mathscr{I}} \tag{2.7a}$$

$$\mathbf{v} = \dot{\mathbf{p}} = \left(\begin{array}{c} v_x \\ v_y \\ v_z \end{array} \right) = \mathbf{v_d}^{\mathscr{H}} = \mathbf{C v_d}^{\mathscr{I}} + \mathbf{r_d}^{\mathscr{H}} \times \dot{\mathbf{\Omega}} \tag{2.7b}$$

The state vector, which only describes the local motion of a deputy satellite in the $\mathscr{H}$-frame is therefore

$$\mathbf{x} = \left(\begin{array}{c} \mathbf{p} \\ \mathbf{v} \end{array} \right) = \left(\begin{array}{cccccc} x & y & z & \dot{x} & \dot{y} & \dot{z} \end{array} \right)^{T} \tag{2.8}$$

However, only the above state vector in combination with the chief's absolute state fully describes the absolute orbit of the deputy. The back transformation is given by the rotation to the $\mathscr{I}$-frame

$$\mathbf{r_d}^{\mathscr{I}} = \mathbf{C}^{-1} \mathbf{p} \tag{2.9a}$$

$$\mathbf{v_d}^{\mathscr{I}} = \mathbf{C}^{-1} \left(\mathbf{v} - \mathbf{p} \times \dot{\mathbf{\Omega}} \right) \tag{2.9b}$$

followed by a translation of the vectors by the chief's state:

$$\mathbf{r_1} = \mathbf{r_0} + \mathbf{r_d} \tag{2.10a}$$

$$\mathbf{v_1} = \mathbf{v_0} + \mathbf{v_d} \tag{2.10b}$$

With this back transformation, the Keplerian orbit of the deputy can be calculated from the chief's absolute state in $\mathscr{I}$ and the deputy's relative state in $\mathscr{H}$.
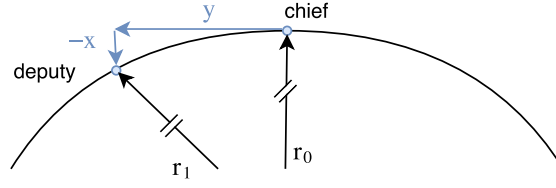
FIGURE 2.2: ECI-to-Hill transformation error induced through orbit curvature (highly exaggerated).

Curvilinear transformation

Vallado and Alfano (2011) suggested a curvilinear transformation between the ECI and the Euler-Hill-frame to compensate the transformation error induced through the curvature of the orbits. Figure 2.2 shows the Cartesian transformation error highly exaggerated. Two satellites at different positions in the same circular orbit have an offset in $\hat{e}_x$ in the $\mathscr{H}$-frame. But since they share the same distance from the centre of the Earth, the radial component of the Hill-frame should be zero. To overcome this error, the transformation is done in a coordinate system which is based on the equidistant cylindrical system (Weisstein, 2016). A topocentric-horizon system $\mathscr{T}$ (or SEZ, for South-East-Normal) is generated for the chief. The offset to the deputy is measured in angle offsets from the centre of the Earth. Let the $\mathscr{R}$-frame be defined through the rotation of the $\mathscr{I}$-frame by $\mathbf{C}$ (without translation). This means, $\mathscr{T}$ is a cylindrical representation of $\mathscr{R}$. It follows for the two rotation angles ϕ and λ (from chief to deputy) in the $\mathscr{T}$-frame:

$$\mathbf{r_1}^{\mathscr{R}} = \mathbf{Cr_1}^{\mathscr{I}} \tag{2.11}$$

$$\phi^{\mathscr{T}} = \arcsin\left(\frac{r_z^{\mathscr{R}}}{||\mathbf{r_1}||}\right) \tag{2.12}$$

$$\lambda^{\mathscr{T}} = \text{atan2}\left(r_y^{\mathscr{R}}, r_x^{\mathscr{R}}\right) \tag{2.13}$$

$$\dot{\lambda}_0^{\mathscr{T}} = \frac{\hat{\mathbf{e}}_\mathbf{y}\mathbf{Cv}_0^{\mathscr{I}}}{||\mathbf{r_0}||^{\mathscr{I}}} \tag{2.14}$$

The position of the deputy in the Euler-Hill-frame $\mathscr{H}$ finally computes to:

$$x = r_x^{\mathscr{H}} = ||\mathbf{r_1}|| - ||\mathbf{r_0}|| \tag{2.15a}$$

$$y = r_y^{\mathscr{H}} = ||\mathbf{r_0}||\,\lambda \tag{2.15b}$$

$$z = r_z^{\mathscr{H}} = ||\mathbf{r_0}||\,\phi \tag{2.15c}$$

To find the velocity, the angular rates between $\mathscr{I}$ and $\mathscr{T}$ have to be known. Let $\mathbf{P}$ be the transformation matrix $\mathscr{R} \rightarrow \mathscr{T}$. With

$$\mathbf{v_1}^{\mathscr{T}} = \mathbf{PCv_1}^{\mathscr{I}} \tag{2.16}$$

holds for the deputy's derivatives of the rotation angles in $\mathscr{T}$:

$$\dot{\phi} = -\frac{\hat{\mathbf{e}}_{\mathbf{x}}\mathbf{v_1}^{\mathscr{T}}}{\|\mathbf{r_1}\|} \tag{2.17}$$

$$\dot{\lambda} = \frac{\hat{\mathbf{e}}_{\mathbf{y}}\mathbf{v_1}^{\mathscr{T}}}{\|\mathbf{r_1}\|\cos\phi} \tag{2.18}$$

Finally, the curvature-corrected velocity in the Euler-Hill-frame $\mathscr{H}$ is:

$$v_x = \hat{\mathbf{e}}_{\mathbf{z}}\mathbf{v_1}^{\mathscr{T}} - \hat{\mathbf{e}}_{\mathbf{x}}\mathbf{C}\mathbf{v}_0^{\mathscr{I}} \tag{2.19a}$$

$$v_y = \|\mathbf{r_0}\|\left(\dot{\lambda} - \dot{\lambda}_0^{\mathscr{T}}\right) \tag{2.19b}$$

$$v_z = \|\mathbf{r_0}\|\,\dot{\phi} \tag{2.19c}$$

Although this correction is not significant for close formations, it has a non-negligible influence for larger distances between the satellites, especially in the phase of initial formation acquisition. Since the computational effort is comparable to the transformation in Cartesian coordinates, the curvilinear approach will be used for propagator and controller implementation when converting between the $\mathscr{I}$- and the $\mathscr{H}$-frame. Under strict consideration, using the above transformation routine does result in another non-Cartesian frame, and not in $\mathscr{H}$. However, the non-Cartesian part is wrapped in the transformation and the resulting frame may be used fully commensurable compared to $\mathscr{H}$, while at the same time having a higher accuracy in the $\hat{e}_x$-, $\hat{e}_y$- and $\hat{e}_z$-directions.

2.1.2   Orbital frames

The relative motion model in the Cartesian Hill-frame lacks the insight of orbital mechanics from the state vector. This insight, however, can be used beneficially in controller design through thrusting action at geometrically advantageous locations in orbit (Schaub et al., 2000). Therefore, absolute and relative orbital elements are needed to represent the states of the satellites in an orbital frame.

Classical orbital elements

The classical orbital elements (COE), also known as the Kepler elements, are a set of six parameters which describe the absolute motion of an (artificial) satellite around a central body. Let the state vector in classical orbital elements be

$$\mathbf{a_C} = \begin{pmatrix} a & e & i & \omega & \Omega & M \end{pmatrix}^T \tag{2.20}$$

with semi-major-axis a [m], eccentricity e (dimensionless), inclination i [rad], argument of perigee ω [rad], right ascension of ascending node Ω [rad] and mean anomaly M [rad] (figure 2.3). The transformation between a Cartesian state vector in the ECI-frame and
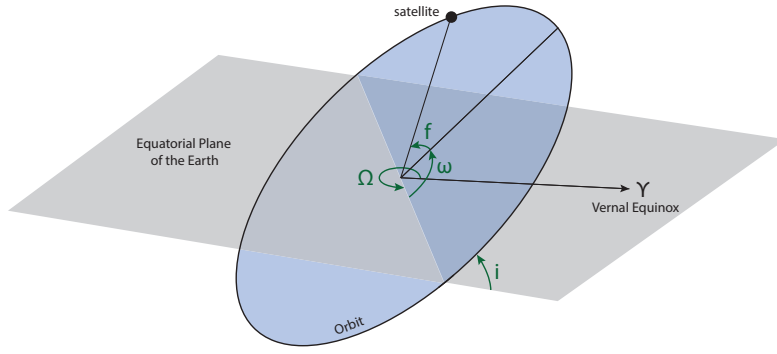
FIGURE 2.3: Geometry of a Keplerian orbit.

COE can be found in Chobotov (2002). For the unperturbed motion, all components of the state vector except the anomaly are constants. Depending on the application, it can be useful to transform the independent variable to the eccentric anomaly E or the true anomaly f. While the mean anomaly increases linearly with time (with 2π-periodicity), the true anomaly is related to the real position of the satellite. The transformation between M and f uses the eccentric anomaly E with the relation:

$$M = E - e \sin E \tag{2.21}$$

This demands an iterative solution when converting from M to E, while the reverse transformation can be solved directly. The following formula describes the relation between E and the true anomaly f:

$$\cos f = \frac{\cos E - e}{1 - e \cos E} \tag{2.22}$$

The relation between f and M and vice versa is obtained by concatenation of equations (2.21) and (2.22). Further characteristics of a Keplerian orbit, which are used later, include the semi-latus rectum p, an eccentricity dependent factor η, the mean motion n and the Keplerian period of the orbit T_O:

$$p = a \left(1 - e^2 \right) \tag{2.23}$$

$$\eta = \sqrt{1 - e^2} \tag{2.24}$$

$$n = \sqrt{\frac{\mu}{a^3}} \tag{2.25}$$

$$T_O = 2\pi \sqrt{\frac{a^3}{\mu}} = 2\pi n^{-1} \tag{2.26}$$

Non-singular orbital elements

The classical orbital elements have singularities for circular orbits and for $i = \{0°, 90°\}$. Since the nominal *NetSat* orbit is almost circular, numerical instabilities may occur when using COE. Furthermore, the orbit may become singular when propagating it under the influence of perturbations. Therefore, the first singularity ($e = 0$) is further investigated. For circular orbits the argument of perigee ω is not defined uniquely. More precisely, ω becomes an arbitrary angle measured from the ascending node (the intersection of the orbit with the equatorial plane of the Earth). However, the sum of the argument of perigee and the anomaly stays unique and is called the argument of latitude θ:

$$\theta = \omega + f \tag{2.27}$$

When only describing the position of a satellite in a circular orbit, the argument of latitude will be used. For more complex calculations (like transforming to/from Cartesian state vectors), a set of six non-singular elements is needed. In this work two different element sets will be used, depending on the application. The first set is called non-singular orbital elements (NOE) with the state vector

$$\mathbf{a_N} = \left(\begin{array}{cccccc} a & \theta & i & q_1 & q_2 & \Omega \end{array} \right)^T \tag{2.28}$$

where $q_1 = e \cos \omega$ and $q_2 = e \sin \omega$. The NOE set is the simplest transformation to overcome the COE-singularity at $e = 0$, since the ambiguous argument of perigee ω has been eliminated. Another set used in this work will be the equinoctial orbital elements (EOE) set, based on Walker, Ireland, and Owens (1985):

$$\mathbf{a_E} = \left(\begin{array}{cccccc} a & e_x & e_y & i_x & i_y & l_v \end{array} \right)^T \tag{2.29}$$

where $(e_x \; e_y)^T$ is called equinoctial eccentricity vector, $(i_x \; i_y)^T$ equinoctial inclination vector and l_v true longitude. They do not have any singularities (including cases stated above) and have a simple transformation from COE. If the initial COE are non-singular, the transformation is described by:

$$e_x = e \cos (\omega + \Omega) \tag{2.30a}$$

$$e_y = e \sin (\omega + \Omega) \tag{2.30b}$$

$$i_x = \tan (i/2) \cos \Omega \tag{2.30c}$$

$$i_y = \tan (i/2) \sin \Omega \tag{2.30d}$$

$$l_v = f + \omega + \Omega \tag{2.30e}$$

Sometimes closely related transformations (e.g. using $\tan i$ for the inclination vector) are utilised, but they lead to singularities at polar orbits. The set obtained from equation

(2.30) is guaranteed to be non-singular and has the additional advantage of highly reducing the number of secular terms in its Jacobian, compared to COE and NOE (Broucke and Cefola, 1972). This makes it ideal to use in numerically intensive calculations like orbit propagation. However, the NOE set allows a clearer geometrical insight into the orbit and is thus used for geometric calculations.

Differential orbital elements

There are two ways to describe the local, or relative, motion of two or more satellites in an orbital frame – differential orbital elements and relative orbital elements (see next section). Relative orbital elements comprise an own frame. Differential orbital elements (DOE) are just the element-wise difference between two satellites' orbital elements (e.g. the absolute difference between their states). For any pair of sets of commensurable orbital elements (COE, NOE, EOE) for the chief ($\mathbf{a_0}$) and the deputy ($\mathbf{a_1}$), they are defined through

$$\delta\mathbf{a} = \mathbf{a_1} - \mathbf{a_0} \tag{2.31}$$

Equation (2.31) has to be used circumspectly. It is very susceptible for numerical errors, especially in the last field of the vector (the differential anomaly). It is a crucial point to obey this inherent virtue or to find ways to bypass this drawback.

Relative orbital elements

The relative orbital elements (ROE) comprise the second local state vector in orbital means. They involve more mathematics than the differential orbital elements, but allow geometrical formation design. From two sets of classical orbital elements, the relative orbital elements $\delta\mathbf{o}$ are defined as follows (D'Amico et al., 2009):

$$\delta\mathbf{o} = \begin{pmatrix} \delta a \\ \delta e_x \\ \delta e_y \\ \delta i_x \\ \delta i_y \\ \delta u \end{pmatrix} = \begin{pmatrix} \delta a \\ \delta\mathbf{e}\cos\phi \\ \delta\mathbf{e}\sin\phi \\ \delta\mathbf{i}\cos\theta \\ \delta\mathbf{i}\sin\theta \\ \delta u \end{pmatrix} = \begin{pmatrix} (a_1 - a_0)/a_0 \\ e_1\cos\omega_1 - e_0\cos\omega_0 \\ e_1\sin\omega_1 - e_0\sin\omega_0 \\ i_1 - i_0 \\ (\Omega_1 - \Omega_0)\sin i_0 \\ u_1 - u_0 \end{pmatrix} \tag{2.32}$$

where $u = \omega + M$ is the mean argument of latitude. In order to have a dimensionless state vector, the relative semi-major axis has been divided by a_0. Some references use the relative mean longitude $\delta\lambda$ instead of δu. This is geometrically more intuitive for formation design, but more difficult to handle when transforming the state vector to the Euler-Hill-frame (Maessen and Gill, 2010). The relation between the two variables is:

$$\delta\lambda = \delta u + (\Omega_1 - \Omega_0)\cos i_0 \tag{2.33}$$

Neglecting any orbit perturbations only u is time dependent, but not δu. It follows that the ROE state vector $\delta\mathbf{o}$ is constant for a specific formation. A first-order mapping of the

relative orbital elements and the Euler-Hill-frame $\mathscr{H}$ providing the deputy's position w.r.t. the chief satellite as a function of $\delta\mathbf{o}$ is given by (D'Amico, Gill, and Montenbruck, 2006):

$$x/a_0 = \delta a - \delta e \cos\left(u - \phi\right) \tag{2.34a}$$

$$y/a_0 = \delta\lambda - \frac{3}{2}\delta a \delta u + 2\delta e \sin\left(u - \phi\right) \tag{2.34b}$$

$$z/a_0 = \delta i \sin\left(u - \theta\right) \tag{2.34c}$$

Equation (2.34) assumes small eccentricity of the chief orbit and small relative distances, e.g. close formations. For stable formations the orbital periods of the satellites have to be equal. Furthermore, centred motion of the deputy satellites around the chief or the virtual centre is achieved by equal mean longitudes, which imposes the following constraint on reasonable formations:

$$\delta a = \delta\lambda = 0 \tag{2.35}$$

For the ROE state vector (2.32) in combination with equation (2.33) this leads to:

$$\delta a = 0 \tag{2.36a}$$

$$\delta u = -\delta\Omega \cos i_0 \tag{2.36b}$$

For this reason, two of the six relative orbital elements are always fixed for centred force-free relative motion. The remaining four elements are composed of the eccentricity vector $\delta\mathbf{e}$ and the inclination vector $\delta\mathbf{i}$. The formation can be designed by defining the relative eccentricity and inclination vector in polar coordinates:

$$\delta\mathbf{e} = \left(\begin{array}{c} \delta e_x \\ \delta e_y \end{array}\right) = \delta e \left(\begin{array}{c} \cos\phi \\ \sin\phi \end{array}\right) \tag{2.37a}$$

$$\delta\mathbf{i} = \left(\begin{array}{c} \delta i_x \\ \delta i_y \end{array}\right) = \delta i \left(\begin{array}{c} \cos\theta \\ \sin\theta \end{array}\right) \tag{2.37b}$$

with δe and δi being the magnitudes and ϕ and θ the phases. ϕ relates to the relative perigee and θ to the relative ascending node, which renders this polar representation the most useful for geometric formation analysis.

The advantage of using $\delta\mathbf{o}$ instead of $\mathbf{x}$ is given in the possibility of geometrically understanding the formation with only $\delta\mathbf{o}$ being provided.

Figures 2.4i and 2.4ii show the relative motion of the deputy around the chief for one orbital period in the chief's LVLH-frame, divided into in-plane motion (IP) and out-of-plane motion (OOP). The IP motion is the projection of the relative motion into the $(\hat{\mathbf{e}}_{\mathbf{x}}, \hat{\mathbf{e}}_{\mathbf{y}})$-plane of $\mathscr{H}$ (which is by definition the orbital plane of the chief) and the OOP motion is the projection into the $(\hat{\mathbf{e}}_{\mathbf{x}}, \hat{\mathbf{e}}_{\mathbf{z}})$-plane. This analysis is done by using the

(I) In-plane motion (II) Out-of-plane motion
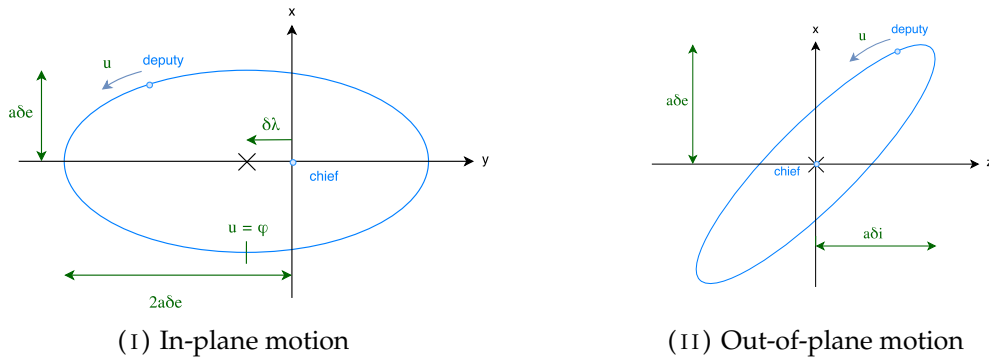
FIGURE 2.4: Relative motion in Hill-frame over one orbital period.

first-order mapping of $\delta\mathbf{o}$ into the $\mathscr{H}$-frame (equation 2.34) in combination with the constraints of centred force-free formations (equation 2.36), which gives:

$$x = a_0 \delta e \cos\left(u - \phi\right) \tag{2.38a}$$

$$y = 2a_0 \delta e \sin\left(u - \phi\right) \tag{2.38b}$$

$$z = a_0 \delta i \sin\left(u - \theta\right) \tag{2.38c}$$

The resulting ellipses for IP and OOP motion can be described with the elements of $\delta\mathbf{o}$ and the semi-major axis a_0 of the chief. The in-plane motion is always a 2-by-1 ellipse. The semi-major axis is defined by $2a_0\delta e$ and the semi-minor axis by $a_0\delta e$, as can be inferred from equations (2.38a) and (2.38b). Furthermore, the position on the ellipse is only dependent on the sine and cosine of the difference $u - \phi$. Apart from that, the out-of-plane motion is described by an oscillating sine-cosine motion with different phase shifts (equations 2.38a and 2.38c), namely $u - \phi$ and $u - \theta$, leading to a tilted ellipse. The maximum extents in radial (x) and normal (z) direction are given by $a_0\delta e$ and $a_0\delta i$, respectively. Assuming the special case of $\delta e = \delta i$ and $\phi - \theta = 0$, the OOP motion is a circle. For a phase shift difference of $\phi - \theta = 90°$, the OOP motion degrades to a straight line going through the chief's position twice per orbit.

While the relative eccentricity δe and the relative inclination δi define the shape of the ellipses, the relative perigee ϕ and the relative ascending node θ define the positions on the ellipses. The mean argument of latitude u (the only time dependent parameter in the discussed equations) is a measure of the satellite's position on its orbit in the ECI reference frame. If $u = \phi$, the deputy satellite is at its maximum extent underneath the chief satellite, assuming circular reference orbits. For that reason, the time at which the deputy is at a specific position on its bounded motion around the centre is controlled by defining ϕ. Similar, when $u = \theta + \pi/2$, the deputy has its maximum relative distance in positive normal direction.

2.2 Relative motion

This section derives differential equations in Cartesian coordinates for the relative state vectors. This includes the central attraction force described by Newton's law of universal gravitation and other perturbing forces, which are exerted to the satellites. This is followed by an analysis in orbital frames, where the motion is split into mean and osculating terms, partitioned into absolute mean and relative mean motion.

2.2.1 Equations of relative motion

Neglecting any perturbing forces and assuming a spherical Earth, the motion of a satellite in $\mathscr{I}$-frame is fully described with the restricted two-body problem (Keplerian equation of motion):

$$\ddot{\mathbf{r}} + \frac{\mu \mathbf{r}}{r^3} = 0 \tag{2.39}$$

With the relative position

$$\mathbf{r_d} = \mathbf{r_1} - \mathbf{r_0}\,, \tag{2.40}$$

the relative equation of motion becomes:

$$\ddot{\mathbf{r}}_d = -\frac{\mu\left(\mathbf{r_0} + \mathbf{r_d}\right)}{\left\|\mathbf{r_0} + \mathbf{r_d}\right\|^3} + \frac{\mu}{r_0^3}\mathbf{r_0} \tag{2.41}$$

With the help of equation (2.7), Alfriend et al. (2010) state equation (2.41) componentwise in Euler-Hill-frame $\mathscr{H}$:

$$\ddot{x} - 2\dot{\theta}_0\dot{y} - \ddot{\theta}_0 y - \dot{\theta}_0^2 x = -\frac{\mu\left(r_0 + x\right)}{\left[\left(r_0 + x\right)^2 + y^2 + z^2\right]^{3/2}} + \frac{\mu}{r_0^2} \tag{2.42a}$$

$$\ddot{y} + 2\dot{\theta}_0\dot{x} + \ddot{\theta}_0 x - \dot{\theta}_0^2 y = -\frac{\mu y}{\left[\left(r_0 + x\right)^2 + y^2 + z^2\right]^{3/2}} \tag{2.42b}$$

$$\ddot{z} = -\frac{\mu z}{\left[\left(r_0 + x\right)^2 + y^2 + z^2\right]^{3/2}} \tag{2.42c}$$

with θ_0 being the z-component of the frame rotation. The magnitude of θ_0 is equal to the magnitude of $\boldsymbol{\Omega}$, since through definition of the frames holds $\boldsymbol{\Omega}^{\mathscr{H}} = (0 \ \ 0 \ \ \theta_0)^T$. This system of non-linear differential equations has a single equilibrium at $\mathbf{p} = (0 \ \ 0 \ \ 0)^T$ and infinitely many equilibria for circular chief orbits. For $e_0 = 0$ every position on the chief's orbit is a stable point and the two spacecraft are in a co-orbital motion. Although these equations can be simplified by changing the independent variable from time t to true anomaly f (Szebehely and Giacaglia, 1964), there is no analytical solution at hand. However, equation (2.42) is the origin of the linearised models developed later.

2.2.2 Perturbation forces

The orbits of the satellites are perturbed by the Earth's non-spherical gravity field, solar radiation pressure, atmospheric drag and the forces exerted by other celestial bodies and thus deviate from a sole Keplerian shape. Most perturbing forces f_i for Earth orbiting satellites may be divided into short-periodic and long-periodic perturbations, where the period used for distinction is in the order of magnitude of the orbital period of the satellite:

$$f_i\left(t\right) = f_{i,sp}\left(t\right) + f_{i,lp}\left(t\right) \tag{2.43}$$

The total force seen by a satellite at any time instant is therefore

$$f_{total}\left(t\right) = f_N\left(t\right) + \sum_i \left(f_{i,sp}\left(t\right) + f_{i,lp}\left(t\right)\right) + f_c\left(t\right) \tag{2.44}$$

where f_N is the idealised central-body attraction and f_c is the total applied control force. f_N is accurately known (equation 2.39), as well as the control input f_c. The evolution of the relative state of two satellites is driven by the differential force between the two satellites, namely:

$$\Delta f\left(t\right) = f_{1,total}\left(t\right) - f_{0,total}\left(t\right) \tag{2.45}$$

For the analysis of relative motion, only the differential perturbing acceleration due to the Earth's oblateness is of higher interest. While the differential acceleration caused by the oblateness of the Earth (J_2-term) is of order $10^{-6} - 10^{-5}\ \mathrm{m\,s^{-2}}$ (for formations of up to $100\,\mathrm{km}$ separation), all other differential perturbing forces do not exceed a magnitude of two decimal powers less (D'Amico, 2010). This analysis is valid for CubeSats with the same ballistic coefficient, which applies to the *NetSat* formation. Furthermore, the *NetSat* satellites use continuous low-thrust propulsion, which means the total propellant mass compared to the whole satellite mass is negligible ($< 1\%$). Thus, fuel-balancing between the satellites may be ignored, which facilitates controller design. Considering this, to accurately model the relative motion to a decent but practical level, the J_2-term of the Earth will be taken into account, while all other perturbing forces are neglected. This reduces the unknowns in equation (2.45) to $\Delta f_{J2,sp}$ and $\Delta f_{J2,lp}$. Analysis of the gravity field influence shows that short-periodic oscillations induced by J_2 are very small for close formations ($\Delta f_{J2,sp} \approx 0$), while the secular variations on a larger time scale have a more significant influence on the relative motion. Hence, for a first approximation, $\Delta f_{J2,sp}$ may be neglected. The two-body problem (see equation 2.39) with a non-spherical gravity model transforms to

$$\ddot{\mathbf{r}} = -\nabla_{\mathbf{r}}\mathscr{V} + \mathbf{u}, \tag{2.46}$$

where $\mathscr{V}$ is the sum of the Keplerian attraction and the J-terms of the Earth and $\nabla_{\mathbf{r}}$ is the Nabla-operator at current position $\mathbf{r}$. $\mathbf{u}$ indicates further perturbation and control forces. Kaplan (1976) developed an explicit formulation for $\mathscr{V}$, when only the second

dynamic form factor of the Earth (J_2) is taken into account:

$$\mathscr{V} = -\frac{\mu}{r}\left\{1 - \frac{J_2 R_E^2}{2r^2}\left[\frac{3}{r^2}\left(\mathbf{r}\hat{\mathbf{K}}\right)^2 - 1\right]\right\}\tag{2.47}$$

Here, $\hat{\mathbf{K}}$ is the unit vector along the $\mathscr{I}$-frame's polar-axis. An explicit formulation of the gravitational acceleration in x, y and z of the $\mathscr{I}$-frame is derived in Bate, Mueller, and White (1971), but there is no known direct transformation into the $\mathscr{H}$-frame (like equation (2.42) for the unperturbed model) with gravitational perturbations. Alfriend et al. (2010) formulated the relative motion states in terms of the angular momentum $\mathbf{h_0}$ (see equation 2.3) of the chief satellite in the Euler-Hill-frame:

$$x = \frac{\delta\mathbf{r}^\mathbf{T}\mathbf{r_0}}{r_0}\tag{2.48a}$$

$$y = \frac{\delta\mathbf{r}^\mathbf{T}\left(\mathbf{h_0} \times \mathbf{r_0}\right)}{||\mathbf{h_0} \times \mathbf{r_0}||}\tag{2.48b}$$

$$z = \frac{\delta\mathbf{r}^\mathbf{T}\mathbf{h_0}}{h_0}\tag{2.48c}$$

The relative velocities can be derived by differentiating equation (2.48). To accurately model a deputy's PV-vector in the Euler-Hill-frame with the above equation, the angular momentum vector of the chief (which is subject to J_2 perturbations) has to be known for all times. This induces an impracticable constraint for controller design. This again demands the development of relative propagation equations linearised around the chief satellite's PV-vector.

2.2.3   Osculating and mean motion

The preceding section analysed the influence of perturbations in Cartesian frames. This can also be done in orbital frames, where motion description can then be split into mean and osculating terms. For the unperturbed case, considering only the Newtonian attraction f_N, all orbital elements – except those including anomaly – stay constant over time. The mean anomaly is related linearly to time, while the other anomaly types are connected by transformation functions (equations 2.21 and 2.22). When perturbing or control forces are considered, all orbital elements change over time. Let $\mathbf{a}$ be the COE state vector of a certain satellite (without loss of generality also applicable for other orbital frames). The time-dependent, or osculating, orbit of the satellite may now be described with

$$\mathbf{a_{osc}}\left(t\right) = \mathbf{A} + \mathbf{a_n} + \mathbf{\Delta a}\left(t\right)\tag{2.49}$$

where $\mathbf{a_n}$ is the nominal (unperturbed) orbital element state at a certain time instant t and $\mathbf{\Delta a}\left(t\right)$ the perturbation-induced change. $\mathbf{A}$ accommodates the mean Keplerian

motion, which influences the anomaly:

$$\mathbf{A} = \begin{pmatrix} 0 & 0 & 0 & 0 & 0 & nt \end{pmatrix}^T \tag{2.50}$$

where n is the mean motion. The last part of equation (2.49) can be split into short-, long-periodic and drift effects:

$$\Delta \mathbf{a}(t) = \Delta \mathbf{a_{sp}}(t) + \Delta \mathbf{a_{lp}}(t) + \Delta \mathbf{a_d}(t) \tag{2.51}$$

In this partition, all oscillating terms must be part of the short- and long-periodic parts and linear terms must be in the drift part. From that, one can define the relationship between an osculating and a mean orbit $\bar{\mathbf{a}}$:

$$\mathbf{a_{osc}}(t) = \bar{\mathbf{a}}(t) + \Delta \mathbf{a_{osc}}(t) \tag{2.52}$$

where

$$\bar{\mathbf{a}}(t) = \mathbf{A} + \mathbf{a_n} + \Delta \mathbf{a_d}(t) \tag{2.53a}$$

$$\Delta \mathbf{a_{osc}}(t) = \Delta \mathbf{a_{sp}}(t) + \Delta \mathbf{a_{lp}}(t) \tag{2.53b}$$

The nominal orbit $\mathbf{a_n}$ coincides with the mean orbit at $t = 0$, so $\bar{\mathbf{a}}_0 = \mathbf{a_n}$. Due to the fact that the drift part contains only linear terms, equation (2.53a) can be written as:

$$\bar{\mathbf{a}}(t) = \mathbf{A} + \bar{\mathbf{a}}_0 + \frac{d\bar{\mathbf{a}}}{dt}\Delta t = \mathbf{A} + \bar{\mathbf{a}}_0 + \begin{pmatrix} d\bar{a}/dt \\ d\bar{e}/dt \\ d\bar{i}/dt \\ d\bar{\omega}/dt \\ d\bar{\Omega}/dt \\ d\bar{M}_0/dt \end{pmatrix} \Delta t \tag{2.54}$$

With this correlation between a mean orbit $\bar{\mathbf{a}}$, which is subject to a constant drift, and an osculating orbit $\mathbf{a_{osc}}$, the effects of perturbation forces on the orbital elements may be investigated. Using the development above, one can infer that the osculating orbit describes the real position at a given time instant (which is directly related to the current **pv**-vector) and the mean orbit describes an averaged position over multiple orbital periods. The transformation between osculating and mean orbit can be done numerically or with analytic methods. The computationally intensive numeric approach is done in orbit propagation tools, like OREKIT (Maisonobe and Parraud, 2016). Any combination of perturbing forces can be used as input for the averaging process, whereby all oscillating terms can be eliminated from the mean orbit without the need for explicit equations of the perturbation influence.

The drawback of this approach is the large computational effort for each single transformation, whereby the need for analytic models arises for on-board propagators and controllers. Since only the J_2-perturbation is of greater interest for formation flying (see section 2.2.2), only this force will be investigated further. This being by far the largest

perturbing force for LEO satellites, many investigations have been undertaken, for example by Walter (1967) and Weisman, Majji, and Alfriend (2014). Most are based on Brouwer's transformation, which provides a transformation function solely based on the orbital elements and independent of time (Brouwer, 1959). Brouwer normalised the J_2 disturbance force (see equation 2.47) with $\epsilon = J_2 R_E^2$ and found an explicit expression for (2.53b) with a change of dependent variables from time t to current mean orbit $\bar{\mathbf{a}}$:

$$\Delta \mathbf{a_{osc}}(\bar{\mathbf{a}}) = -\epsilon \left(\Delta \mathbf{a_{sp,1}}(\bar{\mathbf{a}}) + \Delta \mathbf{a_{sp,2}}(\bar{\mathbf{a}}) + \Delta \mathbf{a_{lp}}(\bar{\mathbf{a}}) \right) \tag{2.55}$$

The short-periodic influence is further split into two parts to accommodate all present perturbation frequencies. The explicit formulation of the right-hand-side of (2.55) for the NOE set can be found in appendix A. Brouwer found them by using a generating function, where the orbit is represented in normalised Delaunay variables. The Delaunay variables are obtained by describing the satellite motion in Hamiltonian mechanics. The Hamiltonian $\mathfrak{H}$ is a function of time t, generalised position coordinates $\mathbf{q}$ and conjugate momenta $\mathbf{p}$:

$$\mathfrak{H}(\mathbf{q}, \mathbf{p}, t) = \mathbf{p}^T \dot{\mathbf{q}} - \mathfrak{L}(\mathbf{q}, \dot{\mathbf{q}}, t) \tag{2.56}$$

The conjugate momenta $\mathbf{p}$ are derived from the generalised velocity coordinates $\dot{\mathbf{q}}$ with

$$\mathbf{p} = \frac{\delta \mathfrak{L}}{\delta \dot{\mathbf{q}}} \tag{2.57}$$

which are defined through Lagrangian mechanics. The Lagrangian of a dynamic system is described through its kinetic energy $\mathfrak{K}$ and potential energy $\mathfrak{U}$:

$$\mathfrak{L}(\mathbf{q}, \dot{\mathbf{q}}, t) = \mathfrak{K} - \mathfrak{U} \tag{2.58}$$

The corresponding relationship between general coordinates and classical orbital elements are the Delaunay elements

$$l = M \tag{2.59a}$$

$$g = \omega \tag{2.59b}$$

$$h = \Omega \tag{2.59c}$$

$$L = \sqrt{\mu a} \tag{2.59d}$$

$$G = \sqrt{\mu a (1 - e^2)} \tag{2.59e}$$

$$H = G \cos i \tag{2.59f}$$

The first three elements (lower case letters) of the Delaunay elements comprise the generalised Hamiltonian coordinates and the latter three (upper case letters) the conjugate momenta:

$$\mathbf{q} = (l, g, h)^T \tag{2.60a}$$

$$\mathbf{p} = (L, G, H)^T \tag{2.60b}$$

Since $\mathfrak{H}$ spans a cotangent space, the time derivatives of the Delaunay elements are:

$$\dot{l} = \frac{\delta \mathfrak{H}}{\delta L}, \quad \dot{g} = \frac{\delta \mathfrak{H}}{\delta G}, \quad \dot{h} = \frac{\delta \mathfrak{H}}{\delta H} \tag{2.61a}$$

$$\dot{L} = \frac{\delta \mathfrak{H}}{\delta l}, \quad \dot{G} = \frac{\delta \mathfrak{H}}{\delta g}, \quad \dot{H} = \frac{\delta \mathfrak{H}}{\delta h} \tag{2.61b}$$

In this representation, the orbit is split into a nominal and a perturbed part:

$$\mathfrak{H} = \mathfrak{H_o} + \epsilon \mathfrak{H_1} \tag{2.62}$$

Since G is the orbital momentum and H its polar component, the unperturbed part $\mathfrak{H_o}$ (Keplerian motion) is only a function of L:

$$\mathfrak{H_o} = -\frac{\mu^2}{2L^2} \tag{2.63}$$

Thus, all conjugate momenta and g and h are constant in $\mathfrak{H_o}$. Brouwer's generating function for the mean-to-osculation transformation is an explicit formulation of $\mathfrak{H_1}$ in terms of the Delaunay elements, which can be transformed to obtain an explicit formulation for equation (2.55). For further information about Hamiltonian orbit representation, the reader is referred to Hori (1966) and Chang and Marsden (2003). This energy-based orbit representation also proves useful to mitigate perturbation influences (see section 3.5).

Since the norm of $\boldsymbol{\Delta}\mathbf{a_{osc}}\,(\bar{\mathbf{a}})$ is very small compared to $\bar{\mathbf{a}}\,(t)$, for the inverse transformation holds:

$$\bar{\mathbf{a}}\,(\mathbf{a_{osc}}) = \mathbf{a_{osc}} - \boldsymbol{\Delta}\mathbf{a_{osc}}\,(\mathbf{a_{osc}}) \tag{2.64}$$

To describe the evolution of the mean and osculating orbit of a satellite with time, additionally the change of the mean orbit $d\bar{\mathbf{a}}/dt$ is needed. Schaub et al. (2000) state that the semi-major axis, the eccentricity and the inclination do not suffer from J_2-drift, hence $d\bar{a}/dt = d\bar{e}/dt = d\bar{i}/dt = 0$. The other mean orbital elements are subject to the following quasi-constant drift rates:

$$\frac{d\bar{\omega}}{dt} = \frac{3}{4}J_2\left(\frac{R_E}{\bar{p}}\right)^2 \bar{n}\left(5\cos^2\bar{i} - 1\right) \tag{2.65a}$$

$$\frac{d\bar{\Omega}}{dt} = -\frac{3}{2}J_2\left(\frac{R_E}{\bar{p}}\right)^2 \bar{n}\cos\bar{i} \tag{2.65b}$$

$$\frac{d\bar{M_0}}{dt} = \frac{3}{4}J_2\left(\frac{R_E}{\bar{p}}\right)^2 \bar{n}\sqrt{1 - \bar{e}^2}\left(3\cos^2\bar{i} - 1\right) \tag{2.65c}$$

Inserting equations (2.55) and (2.65) into equation (2.52) gives an explicit formulation for the transformation between osculating and mean orbital elements and vice versa.

An explicit formulation for equation (2.65) with equinoctial orbital elements (EOM) can be found in Gim and Alfriend (2005).

2.2.4   Mean relative motion

The derivations from the preceding section can also be applied to differential orbital elements. Equation (2.31) may be used with osculating or mean orbital elements in any orbital frame. With the differential orbital elements and the reference orbit in osculating elements, a transformation to mean differential orbital elements would be possible with equation (2.64). For this, the differential orbit has to be transformed to an absolute orbit with equation (2.31), then transformed (along with the reference orbit) to a mean orbit and then transformed back to differential elements. This can be simplified by using a direct mean-to-osculating transformation in differential elements (Gim and Alfriend, 2003). The relation is approximated with a Jacobian-like transformation matrix $\mathbf{D}$:

$$\delta \mathbf{a_{osc}} = \mathbf{D} \delta \bar{\mathbf{a}} \tag{2.66}$$

where $\mathbf{D}$ is a 6×6 matrix with the partial derivatives of the osculating elements with respect to the mean elements. Using equation (2.55), they derived the following representation of $\mathbf{D}$ with dependency solely on the current mean reference orbit $\bar{\mathbf{a}}(t)$:

$$\mathbf{D}\left(\bar{\mathbf{a}}\right) = \frac{\delta \mathbf{a_{osc}}}{\delta \bar{\mathbf{a}}} = \mathbf{I} - \left(J_2 R_E^2\right) \left(\mathbf{D_{sp,1}}\left(\bar{\mathbf{a}}\right) + \mathbf{D_{sp,2}}\left(\bar{\mathbf{a}}\right) + \mathbf{D_{lp}}\left(\bar{\mathbf{a}}\right)\right) \tag{2.67}$$

The elements $\mathbf{D_{sp,1}}$, $\mathbf{D_{sp,2}}$ and $\mathbf{D_{lp}}$ depend on the reference orbit $\bar{\mathbf{a}}$ and make use of the transformation vectors $\Delta a_{sp,1}$, $\Delta a_{sp,2}$ and Δa_{lp} of the Brouwer transformation (equation 2.55). For small eccentricity orbits, terms of $\mathbf{D}$ which include multiplications of e with J_2 almost vanish. Alfriend et al. (2010) derived a simplified version

$$\mathbf{D_s} \approx \mathbf{D} \quad \forall \; e \ll 1 \tag{2.68}$$

where these terms have been dropped. The elements of this simplified version $\mathbf{D_s}$ for differential NOE can be found in appendix B. For the vice versa conversion from osculating to mean differential elements, $\mathbf{D}^{-1}$ has to be found. Since $\mathbf{D}$ is almost an identity matrix due to the small perturbation coefficient, this can be omitted and the following relation holds to a high level of accuracy:

$$\delta \bar{\mathbf{a}} = -\mathbf{D}\left(\mathbf{a_{osc}}\right) \delta \mathbf{a_{osc}} \tag{2.69}$$

2.3   Relative orbit propagation

In the previous section, differential equations of relative motion and mean motion descriptions have been developed. This section will focus on using these equations as inputs for (linearised) relative motion models to find state transition matrices (STMs)

for relative motion. With these STMs, the evolution of the relative state may be predicted. These matrices also are the foundation for controller plant matrices investigated in the next section. The first investigated relative orbit propagation model is a rather simple solution, where orbit eccentricity and perturbations are neglected. The following models will include either of the two, or both, and grow in complexity. Hence they show a higher congruency with the real relative motion.

2.3.1 Hill-Clohessy-Wiltshire equations

The first STM to be investigated, namely the HCW equation (from Hill, Clohessy and Wiltshire), is one of the first motion descriptions for relative orbital motion (Clohessy and Wiltshire, 1960). It is obtained by linearising equation (2.42) about the position of the chief satellite, e.g. the origin of the $\mathcal{H}$-frame. The eccentricity of the chief's orbit is assumed to be zero. With a Taylor series expansion around the chief for the first-order terms, one gets (Montenbruck and Gill, 2012):

$$\ddot{x} - 2n\dot{y} - 3n^2 x = a_x \tag{2.70a}$$

$$\ddot{y} + 2n\dot{x} = a_y \tag{2.70b}$$

$$\ddot{z} + n^2 z = a_z \tag{2.70c}$$

One can directly see that the IP motion (xy-plane) is coupled, but decoupled from the OOP motion (z-direction). For simplification, the perturbing and control accelerations (a_i) are set to zero, leading to the homogeneous form of the second-order ODE (2.70) in matrix form:

$$\dot{\mathbf{x}}(t) = \mathbf{A}\mathbf{x}(t) \tag{2.71}$$

where

$$\mathbf{x}(t) = \begin{pmatrix} x & y & z & \dot{x} & \dot{y} & \dot{z} \end{pmatrix}^T \tag{2.72}$$

and

$$\mathbf{A} = \begin{bmatrix} 0 & 0 & 0 & 1 & 0 & 0 \\ 0 & 0 & 0 & 0 & 1 & 0 \\ 0 & 0 & 0 & 0 & 0 & 1 \\ 3n^2 & 0 & 0 & 0 & 2n & 0 \\ 0 & 0 & 0 & -2n & 0 & 0 \\ 0 & 0 & -n^2 & 0 & 0 & 0 \end{bmatrix} \tag{2.73}$$

For an orbit propagator, the state transition matrix (STM) $\mathbf{\Phi}(t,0)$, which maps the state at time $t_0 = 0$ to the state at time t, is needed:

$$\mathbf{x}(t) = \mathbf{\Phi}(t,0)\mathbf{x}(0) \tag{2.74}$$

The STM is the solution of the HCW equation. Since equation (2.71) is a LTI system, $\boldsymbol{\Phi}$ can be obtained with the matrix exponential of $\mathbf{A}$:

$$\boldsymbol{\Phi}\left(t,0\right) = e^{\mathbf{A}t} = \begin{bmatrix} 4-3c & 0 & 0 & s/n & 2n^{-1}(1-c) & 0 \\ 6(s-nt) & 1 & 0 & 2n^{-1}(c-1) & 4sn^{-1}-3t & 0 \\ 0 & 0 & c & 0 & 0 & sn^{-1} \\ 3ns & 0 & 0 & c & 2s & 0 \\ 6n(c-1) & 0 & 0 & -2s & 4c-3 & 0 \\ 0 & 0 & -ns & 0 & 0 & c \end{bmatrix} \tag{2.75}$$

with $c = \cos(nt)$ and $s = \sin(nt)$. This STM is the basis for many further developments of more accurate relative motion models. The HCW solution is only accurate for circular chief orbits and very small formations, since the neglected differential perturbations are indirectly proportional to the distances between the spacecraft. Investigation of equation (2.75) shows that the in-track position y (second row) is subject to drift through the term

$$\alpha = -6ntx(0) - 3t\dot{y}(0) \tag{2.76}$$

Only formations where this term vanishes are stable, e.g. α has to be zero in order to establish a drift-free formation. This leads to the initial condition of stable formations:

$$\dot{y}(0) = -2nx(0) \tag{2.77}$$

2.3.2 STMs for eccentric chief orbits

The most widespread method of obeying the eccentricity in the relative motion models is to change the independent variable in equation (2.42) from time t to true anomaly f. This is achieved by inserting equations (2.22) and (2.21) into equation (2.42) and setting $M = 2\pi t T_O^{-1}$. The whole transformation is stated in Alfriend et al. (2010) and uses normalised position components $\bar{x}_i = x_i r^{-1}$. With a non-dimensional potential function in $\mathscr{H}$-frame

$$\mathfrak{U} = -\frac{1}{\left[(1+\bar{x})^2 + \bar{y}^2 + \bar{z}^2\right]^{0.5}} + 1 - \bar{x} \tag{2.78}$$

and a pseudo-potential function

$$\mathfrak{W} = \frac{1}{1 + e_0 \cos f_0} \left[0.5\left(\bar{x}^2 + \bar{y}^2 - e_0\bar{z}^2 \cos f_0\right) - \mathfrak{U}\right] \tag{2.79}$$

The final transformation of (2.42) to anomaly-dependent form using equation (2.79) is:

$$\bar{x}'' - 2\bar{y}' = \frac{\delta\mathfrak{W}}{\delta\bar{x}} \tag{2.80a}$$

$$\bar{y}'' + 2\bar{x}' = \frac{\delta\mathfrak{W}}{\delta\bar{y}} \tag{2.80b}$$

$$\bar{z}'' = \frac{\delta \mathfrak{W}}{\delta \bar{z}} \tag{2.80c}$$

The notation $(\cdot)'$ denotes the derivative with respect to true anomaly f. It is obtained by the chain rule:

$$\frac{d(\cdot)}{dt} = (\cdot)' \, \dot{f} \tag{2.81a}$$

$$\frac{d^2(\cdot)}{dt^2} = (\cdot)'' \, \dot{f}^2 + \dot{f} \dot{f}' \, (\cdot)' \tag{2.81b}$$

Tschauner and Hempel (1964) developed a linearised form of equation (2.80), which is referred to as TH equations in literature. Similar to the HCW equations, the development around the chief orbit leads to the following differential equations:

$$\bar{x}'' = \frac{3}{k} \bar{x} + 2\bar{y} \tag{2.82a}$$

$$\bar{y}'' = -2\bar{x} \tag{2.82b}$$

$$\bar{z}'' = -\bar{z}' \tag{2.82c}$$

where $k = 1 + e \cos f$. As in the HCW equations, the decoupling of IP and OOP motion also holds for the eccentric model. A closed-form solution to equation (2.82) was obtained by Lawden (1963), resulting in a STM for relative motion which incorporates the eccentricity of the chief orbit and thereby giving a major improvement compared to the HCW solution. This STM was extended by Carter (1998), who eliminated a singularity of Lawden's STM for $f = i\pi$, $i \in \mathbb{N}$. Carter's STM is therefore a particular solution to equation (2.82) and uses a partly-normalised state vector $\mathbf{x} = (\bar{x} \ \bar{x}' \ y \ \bar{y}' \ z \ \bar{z}')^T$. The closed-form solution is given by:

$$\boldsymbol{\Phi}_{\mathbf{C}}(f) = \begin{bmatrix} \bar{x}_1 & \bar{x}_2 & \bar{x}_3 & 0 & 0 & 0 \\ \bar{x}_1' & \bar{x}_2' & \bar{x}_3' & 0 & 0 & 0 \\ -2S_1 & -2S_2 & -S_3 & -1 & 0 & 0 \\ -2\bar{x}_1 & -2\bar{x}_2 & -(2\bar{x}_3 + 1) & 0 & 0 & 0 \\ 0 & 0 & 0 & 0 & \cos f & \sin f \\ 0 & 0 & 0 & 0 & -\sin f & \cos f \end{bmatrix} \tag{2.83}$$

where

$$K_2 = \left(1 - e^2\right)^{-5/2} \left(\frac{1}{2}E - \frac{1}{4}\sin(2E) - \frac{e}{3}\sin^3 E\right) \tag{2.84a}$$

$$\bar{x}_1 = k \sin f \tag{2.84b}$$

$$\bar{x}_2 = 2e\bar{x}_1 K_2 - \frac{\cos f}{k} \tag{2.84c}$$

$$\bar{x}_3 = -2k \sin f K_2 - \cos^2 \frac{f}{k} - \cos^2 f \tag{2.84d}$$

$$S_1 = -\cos f \left(1 + 0.5e \cos f\right) \tag{2.84e}$$

$$S_2 = 3ek^2 K_2 - \frac{\sin f}{k} \tag{2.84f}$$

$$S_3 = -6k^2 K_2 - \frac{2+k}{2k} \sin\left(2f\right) \tag{2.84g}$$

Another notable STM in this field is the STM by Yamanaka and Ankersen. The YA STM eliminates Lawden's singularity for circular orbits and is very compact (Yamanaka and Ankersen, 2002). Starting from the Lawden STM, the state vectory can also be represented in arc lengths on a spherical triangle in a projection of the relative motion onto the celestial sphere, which improves accuracy, as conducted by Jiang, Li, and Baoyin (2007). In contrast to the preceding STMs, there are also analytical solutions to the relative motion in elliptic orbits. They incorporate complex operations like solving Kepler's equation or finding derivatives of the chief's orbital elements in each time step. For more information on this class of STMs, the reader is referred to Broucke (2003) and Lee, Cochran, and Jo (2007).

2.3.3   STMs incorporating a non-spherical attraction model

Many of the eccentricity-obeying STMs from the previous section were developed under the motivation to find relative motion STMs for terminal rendezvous manoeuvres. With this focus, the J_2-effect may obviously be neglected, since there is no differential perturbation force due to the non-spherical Earth when the spacecraft are at the same position. For formations in the size of up to $100\,\mathrm{km}$ relative distance, like the largest planned *NetSat* configuration, this simplification leads to position errors in the propagation process. Notable STMs which incorporate the J_2-effect into the solution of the HCW equation can be found in Schweighart and Sedwick (2001), Morgan et al. (2012) and Djojodihardjo (2014). They also neglect the eccentricity. Another approach is to use the TH equations as starting point, like in Yamada et al. (2012). They provide an extended solution to the TH equations which solely uses osculating orbital elements and thus allows an analytical treatment of the state transition matrix. This is achieved by splitting the state into a nominal and an osculating part, which also allows to split the STM into the nominal TH-like STM and a perturbed STM. An input needed for the Yamada STM is the current osculating orbit of the chief. This constrains its applicability, because this information may not be available exactly. A solution where this information is not needed is the geometric method used in the GA STM (Gim and Alfriend, 2003). The method uses mean orbital elements for the chief's reference orbit and was later extended to the use of equinoctial orbital elements (Gim and Alfriend, 2005). The state vector in orbital frame uses the NOE set introduced in section 2.1.2. The Cartesian state vector used in the STM is, in contrast to section 2.1.1, ordered as follows:

$$\mathbf{x}\left(t\right) = \begin{pmatrix} x & \dot{x} & y & \dot{y} & z & \dot{z} \end{pmatrix}^T \tag{2.85}$$

The connection between the differential orbital elements and the current state in the Cartesian frame is described by:

$$\mathbf{x}(t) = \Sigma(t)\,\delta\mathbf{a}(t) = [\mathbf{A}(t) + \alpha\mathbf{B}(t)]\,\delta\mathbf{a}(t) \tag{2.86}$$

where $\mathbf{A}$ contains all terms of the unperturbed case and $\mathbf{B}$ all terms affected by J_2, with the leading perturbation coefficient $\alpha = 3J_2R_E^2$. The summarised matrix Σ is obtained through a method developed by Alfriend, Schaub, and Gim (2000), where the position and the velocity of the deputy are developed in a Taylor series expansion around the chief's state and split into nominal parts and osculating parts affected by J_2. For the inverse transformation from DOE to $\mathbf{x}$, the inverse Σ^{-1} is needed. The DOE set at t is acquired with a STM for the differential elements:

$$\delta\mathbf{a}(t) = \boldsymbol{\phi}(t, t_0)\,\delta\mathbf{a}(t_0) \tag{2.87}$$

Matrix ϕ is difficult to obtain, when it is striven for a high level of accuracy. All elements are non-linearly affected by the J_2 perturbation and lead to non-negligible linearisation errors. Therefore, the differential orbital elements are converted into mean element space, allowing to use a mean DOE STM:

$$\delta\bar{\mathbf{a}}(t) = \bar{\boldsymbol{\phi}}(t, t_0)\,\delta\bar{\mathbf{a}}(t_0) \tag{2.88}$$

In the differential mean element set, oscillations have been filtered out (see section 2.2.4), allowing an easier derivation of the STM. For that, the differential drift rates for θ, q_1, q_2 and Ω are calculated, starting from equation (2.65). Semi-major axis and inclination are not affected by this drift, leading to a slim STM for the differential mean elements. $\bar{\phi}(t, t_0)$ is a function of the mean chief orbit and time, which are known quantities – the mean orbit of the chief can be directly propagated with equation (2.65). Since Σ is a function of the (not known) osculating chief orbit, it has to be adapted to use the mean chief orbit as input. As stated before, $\mathbf{A}$ is independent of the J_2 perturbation and therefore not affected by the distinction between osculating and mean orbit. Only the $\mathbf{B}$-matrix has to be adjusted to mean element input, leading to

$$\bar{\Sigma}(t) = \mathbf{A}(t) + \alpha\bar{\mathbf{B}}(t) \tag{2.89}$$

$\bar{\Sigma}$ is now a function of mean absolute elements, but still transforms osculating differential elements into Cartesian space. The state $\delta\bar{\mathbf{a}}(t)$ must be converted into differential osculating space, using the partial derivatives matrix of equation (2.66). The transition for differential mean element state at $t = t_0$ to current state in the Cartesian frame then becomes:

$$\mathbf{x}(t) = \left[\mathbf{A}(t) + \alpha\bar{\mathbf{B}}(t)\right]\mathbf{D}(t)\,\bar{\boldsymbol{\phi}}(t, t_0)\,\delta\bar{\mathbf{a}}(t_0) \tag{2.90}$$

The initial state $\delta\bar{\mathbf{a}}(t_0)$ is obtained with the inverse matrices evaluated at $t = t_0$ from the initial Cartesian state:

$$\delta\bar{\mathbf{a}}(t_0) = \mathbf{D}^{-1}(t_0)\left[\mathbf{A}(t_0) + \alpha\bar{\mathbf{B}_0}(t)\right]^{-1}\mathbf{x}(t_0) \tag{2.91}$$

Combination of equations (2.90) and (2.91) leads to the complete GA STM to transition the state vector in Hill-frame from t_0 to t:

$$\mathbf{\Phi_{GA}}\left(t,t_0\right) = \left[\mathbf{A}\left(t\right) + \alpha\bar{\mathbf{B}}\left(t\right)\right]\mathbf{D}\left(t\right)\bar{\phi}\left(t,t_0\right)\mathbf{D}^{-1}\left(t_0\right)\left[\mathbf{A}\left(t_0\right) + \alpha\bar{\mathbf{B}_0}\left(t\right)\right]^{-1} \qquad (2.92)$$

The theoretical background presented in this section is the foundation of the relative orbit propagators developed in chapter 5.

2.4   Relative control

Formation control is the maintenance or alteration of the coupled relative state vectors of all satellites of the formation at the same time. In contrast to absolute control of LEO satellites, whose point of reference is usually the centre of the Earth, relative control uses a local point of reference. This point depends on the chosen control law and thereby on the utilised local coordinate frame. It can be, among others, the origin of the $\mathscr{H}$-frame or the absolute orbital element set of the chief. A lot of work on general relative control has already been conducted, but mostly is focused on impulsive control. This work will investigate continuous low-thrust control to meet the requirements of the *NetSat* mission. This section includes, after an overview and a classification of different control schemes, continuous thrust modelling, trajectory planning methods and relative control strategies.

2.4.1   Overview

The slowly emerging field of continuous low-thrust (CLT) relative control started with optimisation techniques. Early CLT relative control was conducted by posing an optimisation problem, preferably linearly. Armellin, Massari, and Finzi (2004) defined such a controller with linear optimisation for unperturbed dynamics of formations smaller than $1\,\mathrm{km}$. This is the basis for the model predictive controllers (MPC) described in section 2.4.7. Another notable work on CLT is a long-term asteroid rendezvous manoeuvre described by Schattel et al. (2016). Despite focusing on the rendezvous, it gives insight to thrust modelling techniques. The impeding mismatch to the pursued controller design is the absence of a guiding central gravity field in the vicinity of an asteroid in deep space. Gao and Li (2010) present a CLT control approach which combines global optimisation with Lyapunov functions (CLF, see section 2.4.6). It is an off-line control technique and on account of this rather a trajectory planner than a controller. A further approach in the field of CLT trajectory planning is the in-plane LEO-to-GEO transfer orbit (GTO) planner by Konstantinov, Nikolichev, and Thein (2016). The CLT relative controller by Edlerman and Kronhaus (2016) concentrates on long-term constraint fulfilling in terms of attitude manoeuvres and power budgeting. It is, however, only suitable to control one element of the ROE state vector, namely the relative semi-major axis δa. An on-line CLT relative controller for elliptic reference orbits is described by Sherrill (2013). It belongs to the class of Lyapunov controllers and uses Floquet's theory to exploit the periodicity

of the linear differential equations representing the relative dynamics. Again, this work focuses on rendezvous and very close formation configurations. Another type of CLT trajectory planners is comprised of non-linear multi-objective optimisations. Varga and Pérez (2016) uses a multi-objective evolutionary algorithm (MOEA, see section 2.4.4) to solve many-revolution low-thrust manoeuvres obeying J_2 and eclipse phases. Its underlying problem description is based on the Q-law by Petropoulos (2005). The Q-law is a complex Lyapunov controller, whose CLFs are proximity quotients to the target. They are obtained through analytical models of the maximum rate of change of the differential orbital elements. To better understand the influence of J_2 on controller performance, the reader is referred to Djojodihardjo (2014). His work extensively examines the J_2-effect, but is only valid for near-equatorial reference orbits. A conclusion about the importance of J_2 modelling in controller design is drawn in Breger and How (2007). They state that the delta-v consumption of a J_2-including controller used in a realistic environment is comparable to the consumption of a non-J_2-including controller used in a non-perturbed environment. This means most of the delta-v needed to mitigate the non-spherical relative effects of the Earth can be avoided by taking these effects into account during controller design.

The subsequent section will classify controllers based on the understanding of the formation structure, followed by thrust modelling techniques and a mathematical description of the various control approaches introduced above.

2.4.2 Classification

There are many criteria to classify different control strategies. One previously mentioned is the distinction by thrust model constraints. As position control is conducted with electric propulsion, it is necessary to have a continuous thrust model. The electric propulsion system of the *NetSat* satellites will provide a combined thrust in the order of magnitude of $1 \times 10^{-5}\,\mathrm{N}$. Using impulsive thrust models and control strategies would lead to significant errors with the ultra-low force provided by electrical propulsion. Even a very small orbit correction of $0.01\,\mathrm{m\,s^{-1}}$ takes approximately half an hour. In this time, the anomaly changes about $110°$ for the given mission specifications, which is clearly too large. It is important to note that a continuous thrust model is meant in the sense of long-duration thrusting action. This also includes time-discrete models where thrust is assumed to be constant over a short period.

Scharf, Hadaegh, and Ploen (2004) provide a classification into five different architectures of the formation structure. The structure of all types defined in this controller survey is shown in figure 2.5. Without loss of generality, all types are shown with four satellites in the formation. They are distinguished by inter-satellite connections (depicted in green) or by controller plant structure (depicted in blue). Multiple-Input Multiple-Output (MIMO, diagram 2.5i) controllers combine all satellites of a formation to a single plant. The state vector of this formation-level controller plant is the concatenation of the state vectors of all satellites. A leader/follower controller (diagram 2.5ii) is

(I) MIMO (II) Leader-Follower (III) Virtual Structure (IV) Cyclic (V) Behavioural
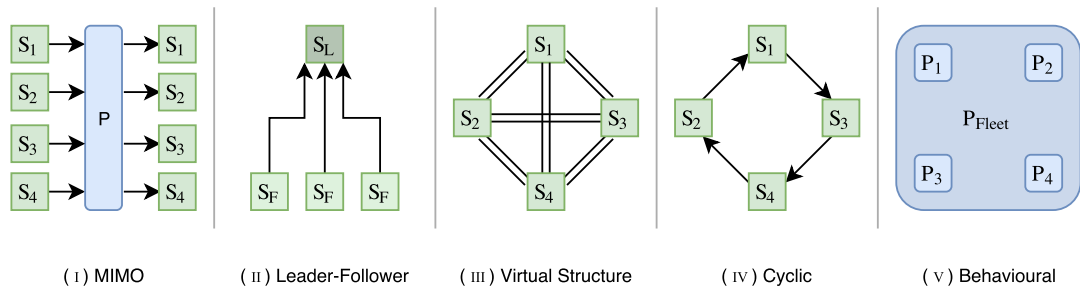
FIGURE 2.5: Formation control architectures as defined by Scharf, Hadaegh, and Ploen (2004). P = controller plant, S = satellite.

a hierarchical structure with one leader and multiple followers. This is the classical approach of relative satellite dynamics, which emerged from rendezvous manoeuvres. The followers (deputies) do not have knowledge about the relative states among themselves. They only control their state in reference to the leader. The leader can be a randomly defined chief satellite or a virtual formation centre without a spacecraft at the origin. As this is the most widespread controller architecture, the following parts of this section will concentrate on this type. In a controller based on a virtual structure (diagram 2.5iii), the formation is treated as a rigid body. The satellites are particles in this body, which are all connected by dynamic links. Each satellite has its own plant which includes rigid body motion and dynamics like contraction and expansion descriptions of the links. The links directly correspond to the relative distances between the spacecraft. A virtual satellite structure can always be broken down into a leader-follower or a cyclic controller, depending on the implementation. Like the virtual structure, also the cyclic method (diagram 2.5iv) is a non-hierarchical controller. This type can be understood as a cyclic connection of leader-follower pairs, where each leader is the follower of another spacecraft. This means that each satellite has exactly one leader and one follower. Cyclic controllers can be modelled with dependency digraphs or potential fields. Both cases make stability proofs of feedback controllers very complicated (or even impossible), since the feedback function grows in complexity with the number of spacecraft. The last controller type is the so-called behavioural plant architecture (diagram 2.5v). It consists of a hierarchical plant structure. Each satellite has (multiple) single-state controllers at the lower control level to pursue a desired satellite state. The higher level is the fleet or formation plant, which pursues high-level goals concerning all spacecraft. The name of this type comes from the contrary and sometimes mutual exclusive goals of the different plants. Thus, the satellites may show competing behaviours and a strategy has to be found which combines these to achieve the highest-level goal. Depending on the specific implementation, this control type can be broken down into a structured combination of MIMO, leader-follower and cyclic controllers.

Due to the two structural break-downs, the whole classification results in three independent structures, namely MIMO, leader-follower and cyclic. Scharf, Hadaegh, and Ploen (2004) conclude that MIMO is preferable in terms of delta-v, since its guaranteed global optimality is a direct consequence of the plant synthesis. Drawbacks are a possible high impact of single-satellite failures and the high amount of needed input information. To

synthesise the plant, each satellite must know the relative state to every other spacecraft of the formation. In contrast, a leader-follower architecture needs less information input. Each follower is only connected to one leader, reducing the necessary inter-satellite communication. The reduced connection amount also increases error robustness. An error in a deputy does not at all affect any other satellite of the formation. Even if a leader-follower configuration provides locally optimal solutions, a disadvantage arises when considering formation-level optimality – the combination of multiple locally optimal solutions must not result in a globally optimal solution. A cyclic architecture provides a mixture of the advantages and drawbacks of the two aforementioned strategies. They may perform better in terms of delta-v compared to leader-follower controllers and furthermore can provide a more even distribution of delta-v consumption. However, communication effort is increased due to the higher amount of inter-satellite connections. As mentioned above, a major downside of this structure is its lack of sophisticated stability-proving techniques. This is a very important step of controller design, since global as well as local stability of the controller has to be guaranteed. Considering all these properties, focus will be led to leader-follower and MIMO architectures.

Another scheme is to distinguish into open-loop and closed-loop controllers. Controllers without feedback may be further divided by their execution period. If this period extends over several orbits, the on-line controller may be viewed the same way as an off-line trajectory planner. In other words, a trajectory planner can be understood as a long-term controller without feedback. Other schemes are based on (non-) linearity or time invariance. Instances of those can belong to any combination of the previously mentioned classifications, as long as they are not mutually exclusive. Furthermore, the goal to be achieved may change the intrinsic behaviour of a controller. The type of the goal can be distinguished by the reference trajectory. In formation-hold phases, this reference is constant. During formation reconfiguration manoeuvres, which include the initial acquisition phase, the reference trajectory is time-varying until the desired formation is obtained. This may be modelled with a single target trajectory or a continuously altering reference, obtained by a so-called reference governor.

2.4.3 Thrust influence

The influence of the thrust, i.e. the control force, on the current state is normally divided by the spacecraft mass (to obtain an acceleration rather than a force) and given in the local LVLH-system of the satellite:

$$\mathbf{u} = \begin{pmatrix} u_x \\ u_y \\ u_z \end{pmatrix} = \begin{pmatrix} u_r \\ u_\theta \\ u_h \end{pmatrix} \tag{2.93}$$

where the acceleration components are labelled by their respective coordinate axes or by r, θ and h for radial, in-track and cross-track direction respectively, depending on the literature. Subject to the used reference frame of the controller, this influence has to
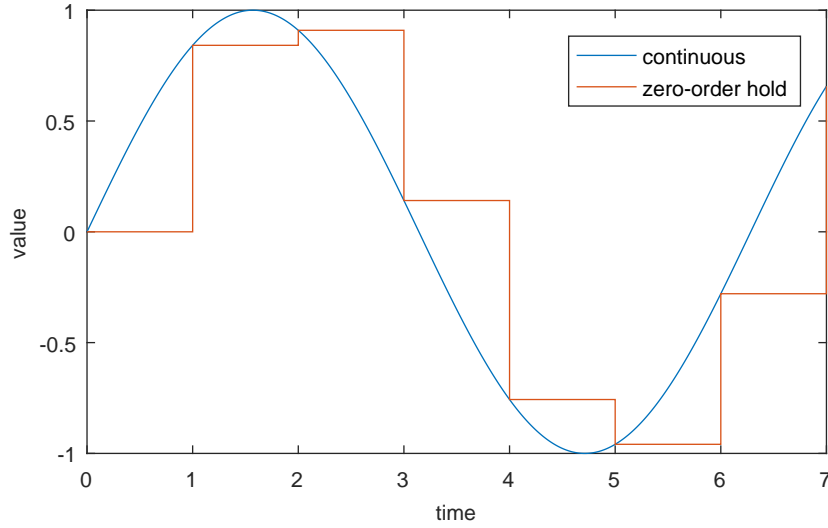
FIGURE 2.6: Continuous function ($f = \sin t$) and its discretised counterpart with zero-order hold assumption with $\Delta t = 1$.

be mapped to the appropriate state vector. In perturbation-free Hill-dynamics, this is a simple direct contribution to the derivative of the state. The state-space equation (2.71) extends to

$$\dot{\mathbf{x}}(t) = \mathbf{A}\mathbf{x}(t) + \mathbf{B}\mathbf{u}(t) \tag{2.94}$$

with the 6×3 control influence matrix $\mathbf{B}$:

$$\mathbf{B} = \begin{bmatrix} 0 & 0 & 0 \\ 0 & 0 & 0 \\ 0 & 0 & 0 \\ 1 & 0 & 0 \\ 0 & 1 & 0 \\ 0 & 0 & 1 \end{bmatrix} \tag{2.95}$$

When an orbital state vector is chosen, the thrust influence can be described with Gauss's variational equations (GVE). They describe the derivative of the classical orbital elements as a function of the current control acceleration (Battin, 1999):

$$\dot{\mathbf{a}}_{\mathbf{C}} = \mathbf{A} + \mathbf{B}(t)\mathbf{u}(t) \tag{2.96}$$

with the matrix elements

$$\frac{d}{dt}\begin{pmatrix} a \\ e \\ i \\ \omega \\ \Omega \\ M \end{pmatrix} = \begin{pmatrix} 0 \\ 0 \\ 0 \\ 0 \\ 0 \\ n \end{pmatrix} + \begin{bmatrix} \frac{2a^2 e \sin f}{h} & \frac{2a^2 p}{rh} & 0 \\ \frac{p \sin f}{h} & \frac{(p+r)\cos f + re}{h} & 0 \\ 0 & 0 & \frac{r \cos \theta}{h} \\ -\frac{p \cos f}{he} & \frac{(p+r)\sin f}{he} & -\frac{r \sin \theta \cos i}{h \sin i} \\ 0 & 0 & \frac{r \sin \theta}{h \sin i} \\ \frac{b(p \cos f - 2re)}{ahe} & -\frac{b(p+r)\sin f}{ahe} & 0 \end{bmatrix} \begin{pmatrix} u_r \\ u_\theta \\ u_h \end{pmatrix} \tag{2.97}$$

This equation is also assuming the perturbation-free case, since only the mean anomaly is subject to change by the mean motion. When thrust influence has to be modelled in perturbed environments, the state-space equations have to be adapted. This does not alter the control influence matrices **B**, whereby they comprise a sufficient thrust impact description for the different kinds of reference frames. In CLT models, as said by the name, the thrust may change continuously. To use the above introduced control influence matrices, the thrust input has to be discretised to an appropriate level of extent. Normally, this is done with a zero-order hold assumption (ZOH). Figure 2.6 shows this discretisation procedure at the example function $f(t) = \sin t$ with a discretisation step size of 1. ZOH means that the level of the very time instant of a discretisation step is maintained by the discretised function until the next discretisation step is reached. In the example figure, the step size is clearly too high to represent the original function to a decent level. In controller design, the step size has to be adapted to an extent that is small enough to only allow minor changes in thrust input during one time step. This is also applicable to continuous thrust inputs (from non-linear models), which should be accommodated in the state space equation of a relative orbit propagator. On the other hand, the derivative of the COE is the limiting factor in step size, if the thrust level is from the start defined to be constant over one time period. If the step size in such a case is too large, the time-varying control influence matrix $\mathbf{B}(t)$ in equation (2.97) produces an increasing error.

2.4.4 Long-term trajectory planning with MOEAs

Multi-objective evolutionary algorithms (MOEAs) are used to solve any kind of non-linear problem definition. The algorithm tries to minimise an arbitrary convex cost function to reach the target. This cost function can consist of orbit deviation quotients (like the already mentioned Q-law solver by Varga and Pérez (2016)) or thrusting values to minimise delta-v consumption. An ESA study on optimising interplanetary spacecraft trajectories deeply analyses and compares different algorithms for use in trajectory generating applications (Myatt et al., 2004). Although the environmental set-up is totally different, the implementation concerning problem definition, thrust modelling and trajectory parametrisation appears to be useful for CLT-transfers. With some adaption, the results can be used as a first draft for long-term formation reconfiguration manoeuvres.

As the name suggests, evolutionary algorithms use the basic ideas behind the theory of evolution. That is, a population of individuals (here solution candidates) with certain individual characteristics (genomes) is exposed to an environment (here the orbital dynamics). This exposure causes a natural selection of individuals (i.e. solutions), leading to a survival of the fittest (Eiben and Smith, 2003). In the beginning, a random population is generated. Each solution candidate has a certain value set for the input variables encoded in its genome. To promote the population, each candidate is then evaluated with a cost function (also fitness function). In the scope of formation control, the genome can consist of thrust inputs over a finite-time horizon. The fitness function is usually

a combination of terminal state vector error and used delta-v. Normally, the fitness function has to be a convex function which tends towards zero at the optimal solution. The reproduction step depends on the particular implemented algorithm. In general, the genomes of the fittest solution candidates are combined or mutated to generate a new generation of candidates. They are again evaluated and the process starts from the beginning. This iterative procedure is continued until a certain error level of the final solutions is undershot or a pre-defined number of generations is reached. In the case of MOEAs, the cost function tries to optimise for different, often competing, goals. As stated before, this is usually manoeuvre time versus delta-v consumption, which is clearly an opposing goal.

The difficulty in generating low-thrust trajectories with MOEAs lies in the problem formulation. A trajectory candidate has to be encoded as a genome, which should give the underlying thrust input vectors as much freedom as possible to not exclude any solutions. On the other hand, a longer genome exponentially increases the search space volume. A higher-dimensional search space requires a higher initial population and more generations to find good solutions. This trade-off has to be made individually for every problem. If a multi-objective fitness function is used, a MOEA (possibly) results in many optimal solutions, a so called Pareto front. In the solution set, no individual dominates another in all its objective values. The MOEA provides only one solution, if one single individual has the smallest value for all objectives. The vast field of MOEAs is subject to further study in the frame of relative formation maintenance and reconfiguration, but the sources cited above suggest their appropriateness for long-term trajectory optimisation.

2.4.5 Linear quadratic regulator

This section introduces the linear quadratic regulator (LQR). The derivation is based on Lunze (2012). LQR is an optimal feedback-based control scheme, which optimises a gain matrix $\mathbf{K}$ in a linear state-feedback control law

$$\mathbf{u} = -\mathbf{K}\mathbf{x} \tag{2.98}$$

with state deviation $\mathbf{x} = \mathbf{x_e} - \mathbf{x_r}$ being the difference between the current state estimate and the state reference (desired state). Equation (2.98) is subject to a state-space definition like the one stated in equation (2.94). The control input (i.e. thrust) is optimised with the use of a quadratic cost function (hence the name of the controller)

$$J_1 = \int_0^{t_1} \left(\mathbf{x}^T(t)\,\mathbf{Q}\mathbf{x}(t) + \mathbf{u}^T(t)\,\mathbf{R}\mathbf{u}(t) \right) dt \tag{2.99}$$

where the symmetric positive definite gain matrices $\mathbf{Q}$ and $\mathbf{R}$ weight the time-dependent state deviation and control inputs, respectively. When this cost function is minimised, the input is optimised over the planning horizon t_1. By varying the ratio between $\mathbf{Q}$ and $\mathbf{R}$, one can direct the attention to either one of the vectors $\mathbf{x}$ or $\mathbf{u}$. This means,

the chosen matrix ratio represents the trade-off between total delta-v consumption to achieve a target orbit and total time until this orbit is reached. With the definition above, J_1 is dependent on the target time t_1. To get a linear time-invariant system (LTI), the planning horizon for the cost function (2.99) is shifted to infinity:

$$J = \int_0^\infty \left(\mathbf{x}^T(t) \mathbf{Q} \mathbf{x}(t) + \mathbf{u}^T(t) \mathbf{R} \mathbf{u}(t) \right) dt \tag{2.100}$$

To get a finite value for the integral, $\mathbf{x} \to \mathbf{0}$ for $t \to \infty$ must hold, i.e. the solution must be feasible under the given constraints. The optimisation problem for thrust and manoeuvre time can now be stated as:

$$\min_{\mathbf{u}(t)} = J(\mathbf{x_0}, \mathbf{u}(t)) \tag{2.101}$$

This dynamic control law can be transformed to a static control law with the LTI feedback (2.98):

$$\min_{\mathbf{K}} = J(\mathbf{x_0}, -\mathbf{K}\mathbf{x}(t)) \tag{2.102}$$

The cost function J is now minimised over the control gain matrix and not the thrust input. It is static, because the control gain matrix is, in contrast to the thrust input, constant over time. To find the optimal control gain $\mathbf{K}$, equation (2.102) has to be solved. For this, the time-dependent state deviation $\mathbf{x}(t)$ is expressed in terms of the initial state and its state transition matrix, as defined in equations (2.73) and (2.75). The time-dependent thrust input is expressed in its state contribution with equations (2.94) and (2.98), leading to the new cost function

$$J = \int_0^\infty \left(\mathbf{x_0}^T e^{\mathbf{A}^T t} \mathbf{Q} e^{\mathbf{A} t} \mathbf{x_0} + \mathbf{x}^T(t) \mathbf{K}^T \mathbf{R} \mathbf{K} \mathbf{x}(t) \right) dt \tag{2.103}$$

This can be split and $\mathbf{x_0}$ can be extracted from the integral to give the form:

$$J = \mathbf{x_0}^T \mathbf{P} \mathbf{x_0} + \int_0^\infty \mathbf{x}^T(t) \mathbf{K}^T \mathbf{R} \mathbf{K} \mathbf{x}(t) \, dt \tag{2.104}$$

where

$$\mathbf{P} = \int_0^\infty e^{\mathbf{A}^T t} \mathbf{Q} e^{\mathbf{A} t} dt \tag{2.105}$$

With the calculus of variations, it is shown that $\mathbf{P}$ can be implicitly expressed as

$$\mathbf{A}^T \mathbf{P} + \mathbf{P} \mathbf{A} = -\mathbf{Q} \tag{2.106}$$

The expression is a Lyapunov equation, which is an important tool for stability analysis (see section 2.4.6). There exists a positive definite solution $\mathbf{P}$, if $\mathbf{Q}$ is positive definite (as is by definition 2.99) and $\mathbf{A}$ is asymptotically stable. Minding the feedback contribution (2.98) of $\mathbf{u}$ in the state space equation gives

$$\bar{\mathbf{A}} = \mathbf{A} - \mathbf{B} \mathbf{K} \tag{2.107}$$

With this transformation, the cost function can be expressed as

$$J = \int_0^\infty \mathbf{x}^T(t)\, \bar{\mathbf{Q}}\mathbf{x}(t)\, dt \tag{2.108}$$

with

$$\bar{\mathbf{Q}} = \mathbf{Q} + \mathbf{K}^T\mathbf{R}\mathbf{K} \tag{2.109}$$

If this is included to the definition of $\mathbf{P}$, one can write the minimisation problem as

$$\min_{\mathbf{K}} J = \min_{\mathbf{K}} \mathbf{x}_0^T\mathbf{P}\mathbf{x}_0 \tag{2.110}$$

where $\mathbf{P}$ is defined through the extended state equations:

$$\bar{\mathbf{A}}^T\mathbf{P} + \mathbf{P}\bar{\mathbf{A}} = -\bar{\mathbf{Q}} \tag{2.111}$$

The solution to equation (2.110) is found by differentiating J with respect to $\mathbf{K}$ and evaluates to

$$\mathbf{K} = \mathbf{R}^{-1}\mathbf{B}^T\mathbf{P} \tag{2.112}$$

or, back-transformed to input space, the optimal thrust profile is given by

$$\mathbf{u}(t) = -\mathbf{R}^{-1}\mathbf{B}^T\mathbf{P}\mathbf{x}(t) \tag{2.113}$$

The inverse of $\mathbf{R}$ exists, since it is positive definite. The optimisation problem is now broken down to finding an explicit expression for $\mathbf{P}$. This is found by inserting equation (2.113) into equation (2.111), which is known as the algebraic Riccati equation (ARE):

$$\mathbf{A}^T\mathbf{P} + \mathbf{P}\mathbf{A} - \mathbf{P}\mathbf{B}\mathbf{R}^{-1}\mathbf{B}^T\mathbf{P} + \mathbf{Q} = 0 \tag{2.114}$$

The ARE may be solved numerically or by matrix factorisation techniques provided by e.g. MATLAB. Ulybyshev (1998) verified the applicability of LQR control in the scope of formation maintenance and long-term tangential manoeuvres. In the CanX-4&5 mission, LQR control was used for formation keeping as well as formation reconfiguration (Eyer, 2009). They showed that it is favourable to select different gain matrix ratios during the two manoeuvre types. Both sources did not use CLT but rather a maximum thrust level in the order of magnitude of $1\,\mathrm{N}$. It has to be analysed, if LQR control can efficiently be used with continuous low-thrust manoeuvres for relative orbit control.

2.4.6 Lyapunov stability

Control-Lyapunov functions (CLF) are Lyapunov functions for controllable systems. With a valid CLF, a feedback matrix $\mathbf{K}$ can iteratively be found. This derivation is loosely based on Schaub et al. (2000) and Lunze (2012). The source was adapted to correspond to the state space of the latter section. As with LQR control, model fidelity but also complexity is adjusted with the selection of the state-space matrix $\mathbf{A}$ and the control influence matrix $\mathbf{B}$. CLF-based controller design in the scope of formation flying

is an emerging field, where some important works were presented in section 2.4.1.

In general, a state-dependent Lyapunov function proves the stability of an ordinary differential equation (ODE). The state space model (2.94) is a set of ODEs and may be controlled with a linear feedback gain. The target of CLF-based controller design is to find the feedback matrix $\mathbf{K}$. The difficult step in creating a CLF-based control law is to find a CLF which proves stability and minimises the thrust input. Often this can only be done with brute-force or trial-and-error techniques. The start of this process is a state-space dependent function which is subject to be proven to be stable in the sense of Lyapunov. Therefore, in the first place it is called a Lyapunov candidate function V and constrained to

$$V\left(\mathbf{x}\right) : \mathbb{R}^n \rightarrow \mathbb{R} \qquad V\left(\mathbf{0}\right) = 0,\, V\left(\mathbf{x}\right) > 0 \tag{2.115}$$

The candidate function maps from the state-space to a scalar and has to be positive definite except at the origin, where it has to evaluate to zero. An equilibrium point $\mathbf{x_e}$ of a system is stable in the sense of Lyapunov, if for any neighbourhood ϵ there exists a neighbourhood δ around $\mathbf{x_e}$, so that $\|\mathbf{x_0}\| < \delta$ leads to $\|\mathbf{x}\left(t\right)\| < \epsilon$. Or, in other words, it is stable, if any state in the local neighbourhood of an equilibrium stays in the vicinity of it for all times. The more restrictive asymptomatic stability demands $\lim_{t\rightarrow\infty} \|\mathbf{x}\left(t\right)\| = 0$. With this definition, a system is asymptotically stable, if any initial state in the local neighbourhood of an equilibrium point reaches this point at some time. Transferred to control Lyapunov functions, this is the same as to demand that V must be monotonically decreasing to reach the equilibrium point. Thus, a candidate function proves stability if and only if:

$$\dot{V}\left(\mathbf{x}\left(t\right), \mathbf{u}\left(t\right)\right) < 0 \qquad \forall t \tag{2.116}$$

The time-derivative of V is in fact a function of the state and the thrust input, since it influences the state derivative. Adapted to relative orbit control, this is illustrated with the linear feedback control law

$$\mathbf{u} = -\mathbf{B}^{-1}\left(\mathbf{A}\mathbf{x_e} + \mathbf{P}\mathbf{x}\right) \tag{2.117}$$

with a positive definite error influence matrix $\mathbf{P}$. Let the candidate Lyapunov function be

$$V\left(\mathbf{x}\right) = 0.5\mathbf{x}^T\mathbf{x} \tag{2.118}$$

The reference state is assumed to be constant in this case. Taking the derivative and inserting first the state space equation, then equation (2.117) gives

$$\dot{V}\left(\mathbf{x}\left(t\right),\mathbf{u}\left(t\right)\right)=\mathbf{x}^{T}\dot{\mathbf{x}}$$

$$=\mathbf{x}^{T}\left(\dot{\mathbf{x}_{e}}-\dot{\mathbf{x}_{r}}\right)$$

$$=\mathbf{x}^{T}\left(\mathbf{A}\mathbf{x_{e}}+\mathbf{B}\mathbf{u}-\mathbf{0}\right)$$

$$=\mathbf{x}^{T}\left\{\mathbf{A}\mathbf{x_{e}}-\mathbf{B}\mathbf{B}^{-1}\left[\mathbf{A}\mathbf{x_{e}}+\mathbf{P}\left(\mathbf{x_{e}}-\mathbf{x_{r}}\right)\right]\right\} \tag{2.119}$$

$$=-\mathbf{x}^{T}\mathbf{P}\left(\mathbf{x_{e}}-\mathbf{x_{r}}\right)$$

$$=-\mathbf{x}^{T}\mathbf{P}\mathbf{x}$$

This solution is strictly negative, since the feedback gain matrix $\mathbf{P}$ is positive definite. Thus, the proposed function (2.118) proves stability of the control law (2.117). This process of proving Lyapunov stability increases in complexity if a variable reference is chosen.

2.4.7   Model predictive control

Model predictive control (MPC) can be used as a trajectory planning tool or an on-board closed-loop controller, depending on the configuration. The outcome of a single MPC computation is a trajectory plan for the whole planning horizon. This makes MPC a very versatile instrument in formation controller design. MPC predicts the influence of the thrust input over a finite-time horizon and provides an optimal solution over this time interval. A MPC controller enforces various (in-)equality constraints on a cost function, which is minimised over the planning horizon. In general, this is done with linear programming. If this interval is extended, the far-time optimality increases at the cost of computational load. A quite short interval can be used in an on-board real-time controller. Also, MPC can be used as a closed-loop control system when only the first command of the plan is implemented and a new plan is generated in every time step. This section is based on Tillerson, Inalhan, and How (2002) and Breger and How (2005). It also uses the simple Hill-frame state-space definition (2.94) like the two preceding sections. Without loss of generality, this definition can be replaced with a linear time-varying model like the ones derived in sections 2.3.2 and 2.3.3.

A key parameter of the MPC is the sample period T_s, i.e. the interval for which thrust commands are generated. These commands can be implemented in the thrust system with a zero-order hold assumption (see section 2.4.3), limiting the maximum sample period. Discretisation of the state-space equation (2.94) is conducted with approximate integration, assuming a very small state and thrust change over one sample period. The ultimate goal of the following equation reshaping process is a form suited for linear

programming, starting with the state space equation of the system. The discretised form of equation (2.94) becomes:

$$\mathbf{x}(k+1) \approx e^{\mathbf{A}_k T_s} \mathbf{x}(k) + \int_0^{T_s} e^{\mathbf{A}_k \tau} d\tau \mathbf{B}(k) \mathbf{u}(k) \tag{2.120}$$

Or, with the definition of the discrete state transition matrix $\mathbf{\Phi}$ (see section 2.3.1) and the discrete control influence matrix $\mathbf{G}_k$:

$$\mathbf{x}(k+1) = \mathbf{\Phi} \mathbf{x}(k) + \mathbf{G}_k \mathbf{u}(k) \tag{2.121}$$

with $\mathbf{x} \in \mathbb{R}^n$ and $\mathbf{u} \in \mathbb{R}^m$, where

$$\mathbf{\Phi} = e^{\mathbf{A}_k T_s} \tag{2.122a}$$

$$\mathbf{G}_k = \int_0^{T_s} e^{\mathbf{A}_k \tau} d\tau \mathbf{B}(k) \tag{2.122b}$$

To let the controller predict all states in the time frame of the planning horizon, $\mathbf{x}(k)$ must be calculable from $\mathbf{x}(0)$ for any k. This is done with discrete convolution of the state and input matrices:

$$\mathbf{x}(k) = \mathbf{\Phi}^{(k,k)} \mathbf{x}(0) + \sum_{i=0}^{k-1} \mathbf{\Phi}^{(k-i-1,k)} \mathbf{G}_i \mathbf{u}(i) \tag{2.123}$$

where the convolution is defined with

$$\mathbf{\Phi}^{(j,k)} = \begin{cases} \mathbf{\Phi}_{k-1} \cdots \mathbf{\Phi}_{k-j+1} \mathbf{\Phi}_{k-j} & 2 \le j \le k \\ \mathbf{\Phi}_{k-1} & j = 1 \\ \mathbf{I} & j = 0 \end{cases} \tag{2.124}$$

Using this definition, the state $\mathbf{x}(0)$ is multiplied k times with the STM $\mathbf{\Phi}(0, T_s)$, propagating the initial state until $t = kT_s$. The control influence is propagated depending on the position in the planning horizon. While the first control influence at $t = 0$ is propagated $k - 1$ times, the last control input at the end of the planning horizon is not at all propagated with the STM. This procedure results in the exact contribution of each thrusting step to the final state. Equation (2.123) can be transformed into the following matrix form:

$$\mathbf{x}(k) = \mathbf{A}(k) \mathbf{U}_k + \mathbf{b}(k) \tag{2.125}$$

where $\mathbf{A} \in \mathbb{R}^{n \times (k+1)m}$ and $\mathbf{b} \in \mathbb{R}^{n \times 1}$. They are given by:

$$\mathbf{A}(k) = \begin{bmatrix} \mathbf{\Phi}^{(k-1,k)} \mathbf{G}_0 & \mathbf{\Phi}^{(k-2,k)} \mathbf{G}_1 & \cdots & \mathbf{\Phi}^{(0,k)} \mathbf{G}_{k-1} & \mathbf{0} \end{bmatrix} \tag{2.126a}$$

$$\mathbf{b}(k) = \mathbf{\Phi}^{(k,k)} \mathbf{x}(0) \tag{2.126b}$$

The control vector $\mathbf{U}_k \in \mathbb{R}^{(k+1)m \times 1}$ is a concatenation of all thrust input values for each time step:

$$\mathbf{U}_k = \left(\begin{array}{ccccc} \mathbf{u}(0)^T & \mathbf{u}(1)^T & \cdots & \mathbf{u}(k-1)^T & \mathbf{u}(k)^T \end{array} \right)^T \tag{2.127}$$

This dynamic model serves as the basis for the linear programme, which minimises the thrust input to achieve an optimal control. The optimisation problem can be stated with the equality constraint to reach the desired target state as:

$$\min_{U_k} \sum_{j=0}^{k} c_j \|\mathbf{u}(j)\| \quad \text{subject to } \mathbf{x}(k) = \mathbf{x_r}(k) \tag{2.128}$$

where the c_j weight the thrust input depending on the time instant in the event horizon. c_j can be a vector of ones or, for example, the vector can impose less weight on early thrust actions to motivate a faster target approach. The optimising function could also be altered to weight the sum over the individual thrusters of the satellite. When an error box around the target state is used, the equality constraint becomes an inequality constraint of the form

$$\|x_i(k) - x_{i,r}(k)\| \leq \epsilon_i \qquad \epsilon_i \geq 0 \ \forall i \in \{1, n\} \tag{2.129}$$

With error box dimensions ϵ_i for all state vector components. By enforcing such a constraint at every (other) time step, a formation maintenance controller can be designed which does not counteract every minor deviation. The controller just cares about holding the satellite in the defined error box around the reference state.

Additional constraints can be added to the linear optimisation problem (2.128) to cope with satellite-inherent properties. When the maximum thrust limit is defined with

$$u^{\min}(i) \leq u(i) \leq u^{\max}(i) \tag{2.130}$$

the inequality constraining thrust levels can be written as

$$\begin{bmatrix} \mathbf{I} \\ -\mathbf{I} \end{bmatrix} \mathbf{U}_k \leq \begin{pmatrix} \mathbf{U}_k^{\max} \\ \mathbf{U}_k^{\min} \end{pmatrix} \tag{2.131}$$

where $\mathbf{U}_k^{\max}$ and $\mathbf{U}_k^{\min}$ are appropriately dimensioned vectors of $u^{\max}(i)$ and $u^{\min}(i)$, respectively. This enforces the priorly stated scalar equation at all time steps. In the same manner, actuator rate limits can be enforced with

$$r^{\min}(i) \leq u(i+1) - u(i) \leq r^{\max}(i) \tag{2.132}$$

where r is the maximum rate change of a thruster during one time step T_s. Tillerson, Inalhan, and How (2002) furthermore provide a method to re-formulate the problem (2.128) as a minimisation problem. In the current form, it is impossible to minimise the input vector $\mathbf{U}_k$, since the individual thrust values may have negative and positive values. To overcome this, they introduce slack variables for positive and negative

contribution and double the size of the input vector:

$$\hat{\mathbf{U}}_k = \begin{pmatrix} \mathbf{U}_k^+ \\ \mathbf{U}_k^- \end{pmatrix} \tag{2.133}$$

where

$$\mathbf{U}_k = \mathbf{U}_k^+ - \mathbf{U}_k^- \tag{2.134}$$

subject to

$$\mathbf{U}_k^+ \geq 0, \quad \mathbf{U}_k^- \geq 0 \tag{2.135}$$

The positive and negative parts of the control input are simply concatenated, by what means the new extended input vector is positive definite. The numerically solvable linear minimisation problem is finally formulated as:

$$J = \min_{\hat{\mathbf{U}}_k} \mathbf{C}^T \hat{\mathbf{U}}_k \tag{2.136}$$

using an extended weighting vector $\mathbf{C}^T$ and being subject to the relative orbit constraint

$$\begin{bmatrix} +\mathbf{A}\,(k) & -\mathbf{A}\,(k) \\ -\mathbf{A}\,(k) & +\mathbf{A}\,(k) \end{bmatrix} \hat{\mathbf{U}}_k \leq \begin{pmatrix} +\mathbf{x_r}\,(k) - \mathbf{b}\,(k) + \boldsymbol{\epsilon} \\ -\mathbf{x_r}\,(k) + \mathbf{b}\,(k) + \boldsymbol{\epsilon} \end{pmatrix} \tag{2.137}$$

and the extended maximum thrust constraint

$$\begin{bmatrix} +\mathbf{I} & -\mathbf{I} \\ -\mathbf{I} & +\mathbf{I} \end{bmatrix} \hat{\mathbf{U}}_k \leq \begin{pmatrix} \mathbf{U}_k^{\max} \\ \mathbf{U}_k^{\min} \end{pmatrix} \tag{2.138}$$

In the same manner, the maximum rate constraint can be extended. Any other state space constraint (for example enforcing equation (2.77) in Hill-frame) can be accommodated as long as it follows the given form to minimise a matrix inequality subject to the thrust input vector.

Non-low-thrust examination of MPC in relative formation control was conducted by Breger and How (2005) with promising results. Later on, they extended their model to use equinoctial orbital elements to remove some singularities (Breger and How, 2007). A terminal-approach (rendezvous) manoeuvre analysis is given in Hartley et al. (2012). Both results encourage the use of MPC in formation control, no matter if using a Cartesian or an orbital state vector.

Chapter 3

Satellite formations

One aim of *NetSat* is to assess various formation types. Different applications impose distinct constraints on inter-satellite-movement, -speed, and formation shape. This demands the analysis of different formation geometries.

An along-track formation (ATF) or a projected circular orbit (PCO) can be used as synthetic aperture radar, optical interferometry or on-orbit servicing of other spacecraft, as examined in the CanX-4/5 mission (Bonin et al., 2015). Furthermore, a PCO can conduct gravitational and magnetic filed analysis and ground-moving target indication. Another well-known formation type is the Cartwheel formation (CWF), whose application can be a digital elevation model (DEM) or a gravity field determination. Applications for the Cross-Track pendulum formation (CTP) also are the optimised gravity field determination and a space-based gravitational wave detector, which is planned by ESA's "Evolved Laser Interferometer Space Antenna (eLISA)" mission. This mission is a planned successor of the cancelled LISA project with similar goals (Danzmann and Team, 2003).

A formation is characterised by its aforementioned type and its size. The size parameter is also called baseline and represents the average distance between the outermost satellites (ATF) or the diameter of the relative ellipses (PCO and CWF). Focus will be directed to ATF, PCO and CWF formations in that order. They describe one-, two- and three-dimensional configurations, allowing to investigate different levels of relative orbit complexity. Without loss of generality, all formation types will be described for four satellites. To design multi-satellite configurations for a different satellite quantity, the respective spacing parameters have to be adapted.

3.1 Initial acquisition phase

After deployment of the satellites (release from the launcher), a slight difference in semi-major axes can occur. In order to ensure a stable formation with bounded motion, i.e. all orbits having the same period, this mismatch has to be cancelled out. Right after deployment, the satellites should recover from possible disturbances. Afterwards, the satellites should perform an orbital manoeuvre in order to acquire the simplest configuration, namely along-track formation (see section 3.2). This can be divided into

acquiring the same semi-major axes first to counteract the initial drift as fast as possible, followed by the acquisition of an ATF formation. According to *Innovative Solutions In Space BV*, a well-known launch provider for nano-satellites, the maximal drift among two satellites after deployment does not exceed $0.1\,\mathrm{m\,s^{-1}}$, while the major fraction is along-track. Therefore, with a very rough estimation of the initial formation behaviour (the initial orbit is assumed to be the nominal *NetSat* orbit with $a = 7000\,\mathrm{km}$ and $e \ll 1$), all six relative orbital elements (ROEs) are zero except the difference in mean argument of latitude δu, which can be derived from equation (2.34). Assuming a non-controllable initial phase of two weeks (which has been the case in the preceding UWE-3 mission) for deployment, signal acquisition and testing, the maximum separation in along-track direction (δu or y in $\mathscr{H}$-frame) at the beginning of the controllable phase will be around $360\,\mathrm{km}$ with the remaining satellites spaced equally in between. This coarse estimation reflects a $360\,\mathrm{km}$ ATF configuration. Consequently, it seems natural to start the mission with a $100\,\mathrm{km}$ ATF formation, which resembles the largest intended baseline.

3.2   Along-track formation

In the along-track formation (ATF), which is also called String-of-Pearls, the four satellites are placed in the same orbit and are separated at a specific distance along the orbit. Since they have equal orbits, only the argument of latitude differs when describing the formation with ROEs. For formation design, it is useful to multiply the ROE vector by a_0, so all entries of the state vector have the dimension $[m]$. According to figures 2.4i and 2.4ii, this gives a direct insight into inter-satellite distances in Hill-frame and simplifies formation design. Following the definition of equation (2.32), the ATF is described by

$$
a_0 \delta \mathbf{o}_k = a \begin{pmatrix} \delta a_k \\ \delta (e_x)_k \\ \delta (e_y)_k \\ \delta (i_x)_k \\ \delta (i_y)_k \\ \delta u_k \end{pmatrix} = \begin{pmatrix} 0 \\ 0 \\ 0 \\ 0 \\ 0 \\ \delta u_{k-1} + \delta r_{max}/(n-1) \end{pmatrix} \tag{3.1}
$$

where index $k \in \{1, 2, 3\}$ denotes the follower satellites and $n = 4$ the number of satellites in the formation. The ROE state vector for the (arbitrary) chief satellite is the isotropic vector, resulting in $\delta u_0 = 0$. δr_{max} is the maximum distance between the satellites and will lie between $100\,\mathrm{km}$ and the closest possible separation. Since all satellites have the same orbit, ideally there is no relative movement between the satellites. Viewed in an idealised Hill-frame, the $\mathbf{p}$-vector is constant and $\mathbf{v}$ is the null vector. As δu solely impacts the y-coordinate, the x- and z-components of $\mathbf{p}$ are always zero in a perfect ATF configuration. In a real Hill-frame, per contra, there will always be some movement in x- and z-direction. This is due to the linearisation error of the $\mathscr{H}$-frame definition (section 2.1.1). Figure 3.1 shows the relative trajectories of the satellites in a $5\,\mathrm{km}$ ATF configuration over one orbital period. The formation centre was chosen, in contrast to the definition above, to be in the middle of the two outermost satellites.

(I) In-plane motion (II) Out-of-plane motion
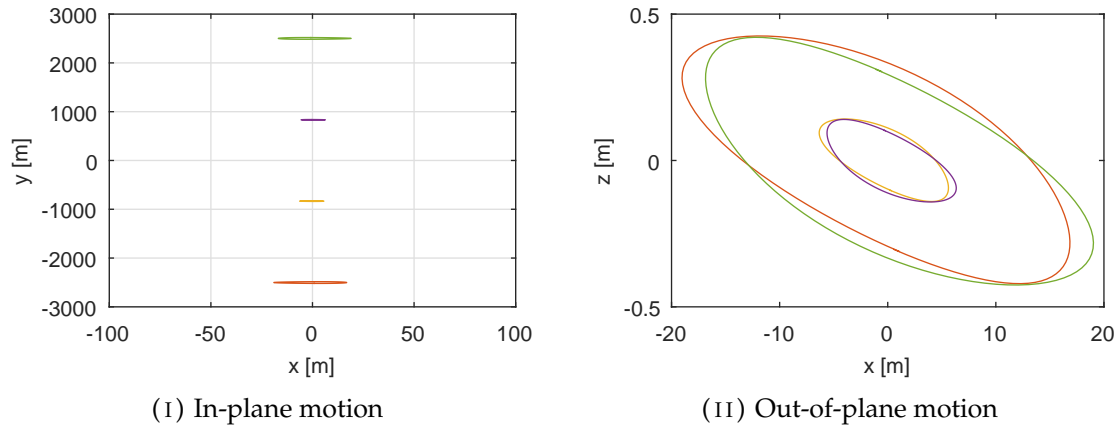
FIGURE 3.1: Relative satellite motion of a $5\,\text{km}$ ATF configuration.

This reduces the linearisation error by a factor of two. Image 3.1i shows the relative in-plane motion, where the $5\,\text{km}$ baseline can be seen in y-direction. The linearisation error caused by the curvature of the orbit occurs mainly radially, while a cross-track-movement is almost non-existent (figure 3.1ii). The corresponding state vector in ROE frame for the described formation is given in table 3.1. Since (ideally) there is no relative movement and a separation in only one direction, ATF is a 1D-formation.

TABLE 3.1: State vectors for a $5\,\text{km}$ ATF configuration. All values are given in $[m]$.

Satellite	1	2	3	4
δa	0	0	0	0
δe_x	0	0	0	0
δe_y	0	0	0	0
δi_x	0	0	0	0
δi_y	0	0	0	0
δu	-2500	-833	833	2500

3.3 Projected circular orbit

The projected circular orbit (PCO) formation describes a circular orbit of the follower satellites around the chief, as seen from the Earth. The follower orbits define an ellipse in $\mathscr{H}$-frame, which is a circle when projected into the yz-plane. This ellipse, which is shared by all followers, is tilted by δi. This results in a straight line in xz-plane, as can be seen in figure 3.2ii. Figure 3.2i shows the 2-by-1 in-plane ellipse with four equally spaced followers. The dotted lines depict the instantaneous position vectors of the satellites. The follower orbits are defined by the relative velocities in yz-plane, whose magnitudes are constant at every time instant. The two conditions to describe a PCO formation can be inferred from equation (2.38). Also deploying equation (2.37), it can be seen that the magnitude of the relative inclination vector has to be twice as high as the magnitude of the relative eccentricity vector for a PCO configuration ($\delta i = 2\delta e$). Second, the phase angles of the two vectors ϕ and θ must have a difference of $\pm 0.5\pi$. The angle offsets

(I) In-plane motion

(II) Out-of-plane motion
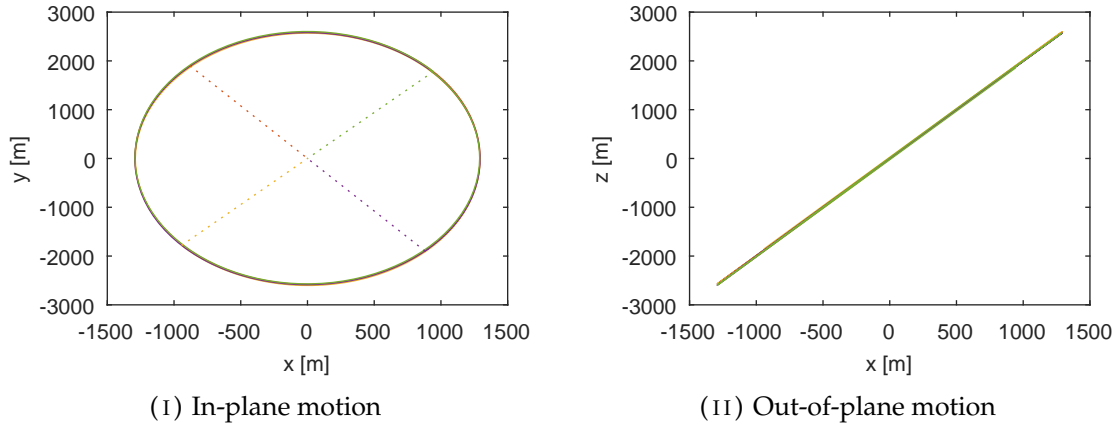
FIGURE 3.2: Relative satellite motion of a $5\,\text{km}$ PCO configuration.

between the four follower satellites on the common circumferential ellipse is $\Delta\phi = {}^1\!/2\pi$. The general ROE definition for the PCO formation is therefore

$$
a_0\delta\mathbf{o}_k = a
\begin{pmatrix}
\delta a_k \\
\delta\left(e_x\right)_k \\
\delta\left(e_y\right)_k \\
\delta\left(i_x\right)_k \\
\delta\left(i_y\right)_k \\
\delta u_k
\end{pmatrix}
=
\begin{pmatrix}
0 \\
a_0\tau\cos\left(\gamma_{k-1} + 0.5\pi\right) \\
a_0\tau\sin\left(\gamma_{k-1} + 0.5\pi\right) \\
2a_0\tau\cos\left(\gamma_{k-1} + \pi\right) \\
2a_0\tau\sin\left(\gamma_{k-1} + \pi\right) \\
-\dfrac{\delta\left(i_y\right)_k}{\tan i_0}
\end{pmatrix}
\tag{3.2}
$$

where index $k \in \{1, 2, 3\}$ denotes the follower satellites, τ is the free variable to define the size of the PCO formation and γ distributes the satellites equally, while γ_0 is the second arbitrary design parameter. The relative argument of latitude δu_k is defined according to equation (2.36b) to place the formation centre (virtual chief) in the very centre of the ellipse. The product $a_0\tau$ directly corresponds to the formation baseline. This PCO type promotes fuel balancing between the satellites and a homogeneous spacing. A PCO formation can also be established with three satellites on the ellipse and a chief in the focus. The state vector of this PCO variant is of the same nature as equation (3.2). Only the spacing angle has to be adapted to $\Delta\phi = {}^2\!/3\pi$ and the chief is located at $r = (0\ \ 0\ \ 0)^T$. In a PCO configuration, all satellites share a common plane of movement, making PCO a two-dimensional formation. The very state vector for the formation depicted in figure 3.2 is stated in table 3.2.

TABLE 3.2: State vectors for a $5\,\text{km}$ PCO configuration. All values are given in $[m]$.

Satellite	1	2	3	4
δa	0	0	0	0
δe_x	1291	0	-1291	0
δe_y	0	1291	0	-1291
δi_x	0	-2582	0	2582
δi_y	2582	0	-2582	0
δu	349	0	-349	0
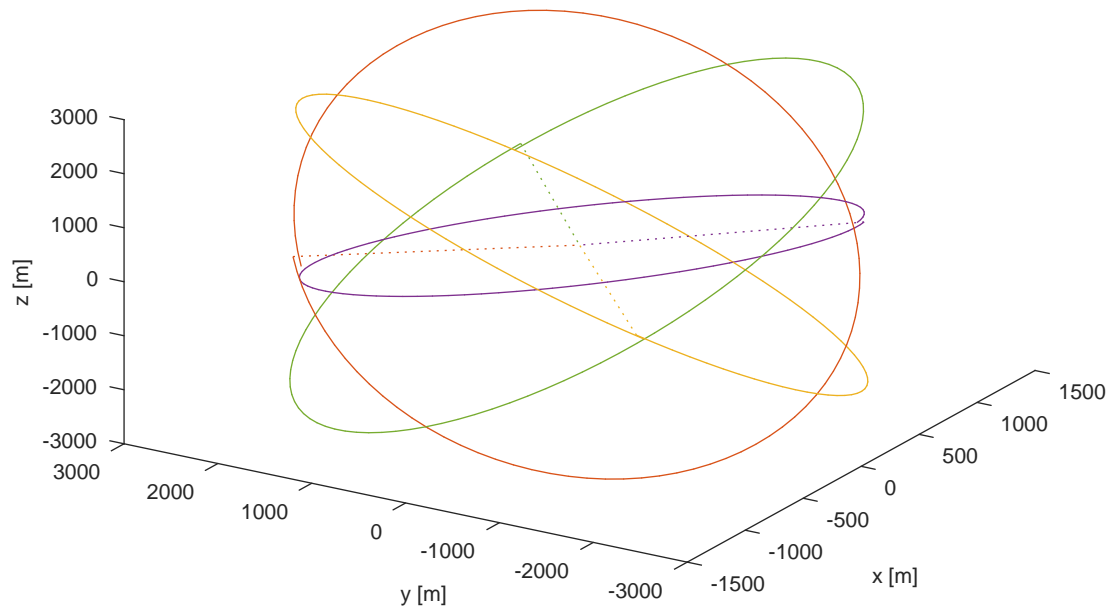
FIGURE 3.3: Relative satellite motion of a $5\,\mathrm{km}$ CWF configuration in 3D-space.

3.4 Cartwheel formation

The Cartwheel formation (CWF) describes a 3D-formation, where the follower satellites orbit around a (virtual) chief on differently inclined ellipses (see figure 3.3). The instantaneous positions of the deputies define a plane, which is always parallel to the plane defined by the along-track and the normal directions. By this, the 3D-formation degenerates to a constantly moving 2D-structure, when only the deputies are regarded. To achieve this behaviour, all deputies share the very same absolute inclination, resulting in the constraint $u - \theta = const$. The arguments of perigee and the true anomalies are equally spaced throughout the orbit. The along-track and cross-track baselines are coupled and remain in an envelope, thus $\theta = 1/4\pi$. This implies the constraint $\delta e = \delta i$ for CWF formations (Peterson, Zee, and Fotopoulos, 2008). The general CWF description in ROEs is:

$$
a_0 \delta \mathbf{o}_k = a
\begin{pmatrix}
\delta a_k \\
\delta (e_x)_k \\
\delta (e_y)_k \\
\delta (i_x)_k \\
\delta (i_y)_k \\
\delta u_k
\end{pmatrix}
=
\begin{pmatrix}
0 \\
a_0 \tau \cos(\gamma_{k-1} + 0.5\pi) \\
a_0 \tau \sin(\gamma_{k-1} + 0.5\pi) \\
a_0 \tau \sqrt{2}^{-1} \\
a_0 \tau \sqrt{2}^{-1} \\
-\dfrac{\delta (i_y)_k}{\tan i_0}
\end{pmatrix}
\tag{3.3}
$$

where again the product $a_0\tau$ defines the baseline, γ_0 is an arbitrary design parameter and δu was chosen to ensure centred motion. Equation (3.3) matches the PCO definition (3.2) in the relative eccentricity vector. The CWF configuration can be understood as a PCO formation with among themselves tilted ellipses. CWF's in-plane motion (figure

(I) In-plane motion   (II) Out-of-plane motion
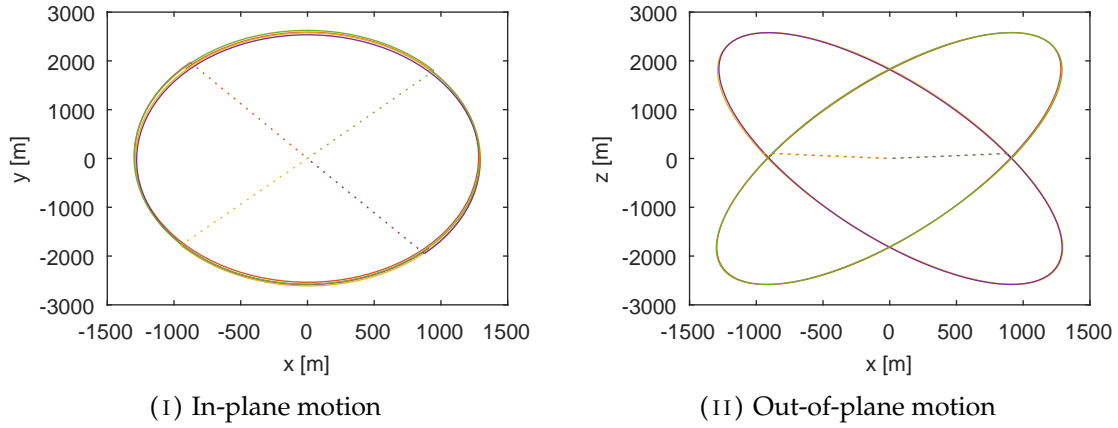
FIGURE 3.4: Relative satellite motion of a $5\,\mathrm{km}$ CWF configuration

3.4i) is exactly the same as in a PCO configuration. This is a direct consequence from the common eccentricity vector. Beyond this, the out-of-plane motion (figure 3.4ii) is also elliptical for CWF. With four follower satellites, the out-of-plane ellipses are equal by twos. This arises from a $180°$-shift per two satellites. The aforementioned plane defined by the instantaneous positions equals the dotted position lines in figure 3.4ii. The perfect alignment of this plane with the out-of-track plane can also be seen in figure 3.3. The explicit state vector for this configuration is given in table 3.3. As with the latter formation, CWF can also be built with three circling satellites and a chief in the centre.

TABLE 3.3: State vectors for a $5\,\mathrm{km}$ CWF configuration. All values are given in $[m]$.

Satellite	1	2	3	4
δa	0	0	0	0
δe_x	1291	0	-1291	0
δe_y	0	1291	0	-1291
δi_x	1826	1826	1826	1826
δi_y	1826	1826	1826	1826
δu	247	247	247	247

3.5   J2 perturbation mitigation

The ROE state vectors for the formation descriptions were designed under regard of the constraints from equation (2.36). When perturbations are not neglected, these constraints have to be adapted. In this analysis, only the J_2-induced effect will be regarded, as the remaining perturbation forces hardly influence formation behaviour (section 2.2.2). Satellites in a formation will drift apart, if any of their three angle rates do not match. The angle rates are the angular velocities in in-track, cross-track and radial direction. A handy description of the angle rates is inherent in the Delaunay elements, i.e. in the Hamiltonian orbit description (equations 2.56 and 2.59). In this representation, the motion is divided into unperturbed and perturbed parts, as equation (2.62) denotes (where the perturbation coefficient is now $\epsilon = -J_2$). The unperturbed part $\mathfrak{H}_0$ is explicitly given by equation (2.63) and the perturbed part $\mathfrak{H}_1$ is given by the perturbation

function from Brouwer's mean-to-osculating transformation (Brouwer, 1959):

$$\mathfrak{H}_1 = \frac{\mu^4 R_E^2}{4L^6} \left(\frac{a}{r}\right)^3 \left[\left(3\frac{H^2}{G^2} - 1\right) + 3\left(1 - \frac{H^2}{G^2}\right)\cos\theta\right] \tag{3.4}$$

Following the deviation in Alfriend et al. (2010), the Hamiltonian $\mathfrak{H}$ is now transformed to a normalised representation. For that purpose, distance is normalised by Earth's radius and time is normalised by the orbital period. Thus, R_E and μ are no longer part of $\mathfrak{H}$ and further conversions simplify. The normalised Hamiltonian $\bar{\mathfrak{H}}$ is then inserted into equation (2.61) to find the angular rates $\dot{l}$, $\dot{g}$ and $\dot{h}$. A back-transformation of the explicit formulation of the angular rates to orbital elements gives:

$$\dot{l} = \frac{1}{a^{3/2}} + \epsilon\left(\frac{3}{4a^{7/2}\eta^3}\right)\left(1 - 3\cos^2 i\right) \tag{3.5a}$$

$$\dot{g} = \epsilon\left(\frac{3}{4a^{7/2}\eta^4}\right)\left(1 - 5\cos^2 i\right) \tag{3.5b}$$

$$\dot{h} = \epsilon\left(\frac{3}{2a^{7/2}\eta^4}\right)\cos i \tag{3.5c}$$

Two satellites will drift apart if and only if their rates are different:

$$\delta\tau = \tau_1 - \tau_0 \neq 0, \quad \tau = \left\{\dot{l}, \dot{g}, \dot{h}\right\} \tag{3.6}$$

When a stable formation is desired, the satellites may not drift apart, i.e. equation (3.6) has to evaluate to zero for all three angular rates. In the following, the consequences of this constraint on formation design are examined. The differential angular rates are obtained by expanding equation (3.5) in a Taylor series around the chief satellite. From this expansion it can be seen that the differential rates only depend on conjugate momenta, but not on the initial position or angle differences. The initial differential conjugate momenta are a function of δa, $\delta\eta$ and δi. This gives three equations with three unknowns, explicitly:

$$\delta a = \frac{1}{2}J_2 a_0 \left(\frac{R_E}{a_0}\right)^2 \frac{3\eta_0 + 4}{\eta_0^5}\left(\left(1 - 3\cos^2 i_0\right)\delta\eta - \eta_0\sin\left(2i_0\right)\delta i\right) \tag{3.7a}$$

$$\delta\eta = \frac{5\eta_0\sin\left(2i_0\right)}{4\left(1 - 5\cos^2 i_0\right)}\delta i \tag{3.7b}$$

$$\delta\eta = -\frac{\eta_0\tan i_0}{4}\delta i \tag{3.7c}$$

Only when all three sub-equations are fulfilled, the formation will not suffer from any drift due to the J_2-factor of the Earth. This well-determined system imposes three constraints on initial formation design, restricting the shape of the formation. Or, in other words, restricting the available ROE state vectors derived earlier in this chapter. The first one constrains δa as a function of $\delta\eta$ and δi, the other two are coupled and both constrain $\delta\eta$ and δi. A mismatch in δa causes a drift in the first Delaunay angle

$\dot{l}$ as can be inferred from equation (2.59a), since the mean rotation rate is a function of the semi-major axis (equation 2.25). Considering all formations are constrained to a zero-offset in semi-major axis when perturbations are neglected, this constraint can easily be integrated in formation state vectors. This does not restrict available types or sizes of formations. Only the first element of the desired ROE vector has to be replaced with the result from equation (3.7a).

The other two constraints are coupled in $\delta\eta$ and δi and only their trivial solution, e.g.

$$\delta\eta = \delta i = 0 \tag{3.8}$$

satisfies equation (3.6). Fulfilling equation (3.8) would only allow String-Of-Pearls formations, since the relative eccentricity and inclination vectors would have to be zero. Even regarding a single constraint of the two coupled ones greatly limits available formation shapes, since it determines the eccentricity vector after an inclination vector is chosen (and vice versa). Consequently, these constraints will not be regarded in formation state vector design. Counteracting these differential rates will be part of the control effort and increase total delta-v consumption during formation hold phases. This effort, anyhow, is very small compared to the total J_2-mitigation effort consisting of all three constraints (equation 3.7). This can be seen in the detailed analysis in section 6.1.

With the above choice of respected constraints, all formation shapes derived in the beginning of this chapter are feasible.

Chapter 4

Software framework

To simulate the satellite orbits as well as to evaluate propagator and controller performance, a comprehensive software framework has been developed. It features (perturbed) orbit propagation, formation state vector design, formation-level trajectory planning, propagator and controller evaluation, performance benchmarking and an extensible debug interface. The framework, which is written in Java, features a fully configurable satellite model and extends a well-known third-party framework (OREKIT) for propagating the dynamic states of the satellites. The first section in this chapter will introduce the main workflow of the software, whereas the following sections go into further detail about the satellite model and the orbit propagator.

4.1   Overview

The software uses configuration files in CSV-format (comma-separated values). From these configuration files, dynamic databases are created at programme start-up, one for the satellite model and one for the orbital dynamics simulation. The satellite model database stores initial information about all active subsystems and is also used to exchange up-to-date data between the subsystems during orbit propagation. When a whole formation is propagated, each satellite has its own database. This means, every spacecraft is treated individually and inter-satellite communication and data exchange may be modelled at different levels of complexity, independently of the current satellite configuration. After initialisation, the orbits of all satellites are instantiated simultaneously with the orbital dynamics framework OREKIT (OREKIT, 2016). Figure 4.1 depicts the whole execution process of the developed software. During the propagation process, the different satellite subsystems execute their procedures at their respective frequencies. This part is illuminated in detail in section 4.3 Every piece of information in the satellite databases and the current relative and absolute orbits may be viewed in live-updated MATLAB plots. The data exchange with MATLAB is realised over a network connection (UDP), giving the possibility to plot the results on a remote machine. The software includes multiple on-board propagators and controllers of different levels of complexity, which was the main focus of this work. Beyond this, it provides implementations and conversion procedures for all frames mentioned in section 2.1, perturbation models and a formation-level trajectory planner for all kinds of manoeuvres. It provides convenient
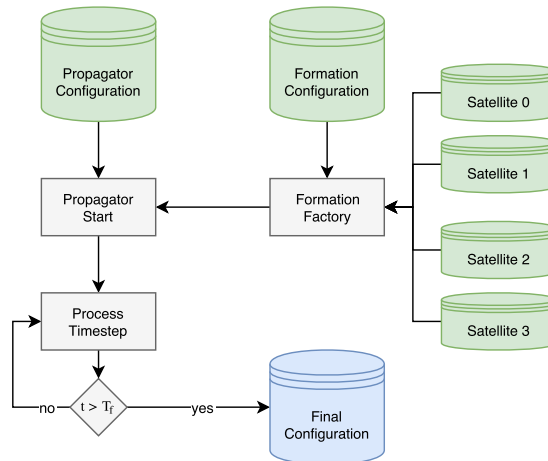
FIGURE 4.1: Data flow and execution process of the software framework. Input data (form the configuration databases) is depicted in green, output in blue.

formation design not only in ROEs (as in chapter 3), but also in any possible absolute and relative frame.

4.2 Satellite model

The satellite model was developed with a focus on reconfigurability, while, at the same time, the computation speed of the subsystem procedures was not neglected to achieve a reasonable orbit propagation time. Furthermore, it was developed to provide the *NetSat* team with a model which can be used at all phases of mission design, independently of the foci of this work.

4.2.1 Subsystem structure

The satellite model consists of the bare satellite structure and the subsystems. The sole purpose of the bare structure is to update the database with the current spacecraft state (like on-board time, orbit, mass, **pv**-vector) after each propagation step and to call the procedures (so called handle-step methods) of all active and waiting subsystems. A subsystem is meant to be waiting when its last procedure call is longer ago than its execution interval (measured in on-board time). A subsystem in the sense of this software model does not have to be a classical satellite subsystem, but may also be a very simple procedure which has to be executed at certain time intervals (e.g. as simple as printing debug information to the console when the satellite enters eclipse). Subsystems are created via the CSV-configuration by adding a defining structure to the table. This definition features a name, which will also be the Java class name of the subsystem generated from the configuration file. The definition also includes an active flag (to easily switch off some functionality if needed), the execution interval, a verbose flag (indicating if the subsystem is allowed to print to the console) and a unique execution

position. Therefore, if multiple subsystems are in waiting mode at the same time instant, the order of execution may be controlled. For example, the attitude sensing system has to be executed before the relative orbit controller, since it relies on up-to-date orbit information. Since all this information is part of the database, it may be altered during execution, e.g. activating a battery loading procedure only during non-eclipse phases or enabling housekeeping data storage only during times without ground station contact. A broad overview of the most important subsystems stated in their order of execution is given in the following. If multiple alternatives for a specific function are stated, this may be configured through the database.

1. AODS (Attitude and Orbit Determination System)
   retrieves ("senses") the current orbit and attitude from the propagator. This may be the exact values from the propagator (OREKIT) or an extended version with an error model. The error model can be applied on absolute or relative state vectors. This can be used to evaluate on-board propagator sensitivity to input state deviations. In a later implementation, the direct OREKIT input can be substituted with attitude and position sensor models.

2. MH (Mission Handler)
   works as the major planning instance and updates the control target at configured times to different types of formations. Thereby, the whole *NetSat* mission plan may be simulated with a single propagation run. The mission handler can react to database events like the termination of a formation change manoeuvre. Once triggered, it can update the new control target, change the active controller implementation or send a status update to the other satellites of the formation.

3. On-board propagator
   propagates the relative state with reference to the (virtual) chief of the formation. The implementation features various on-board propagators with increasing level of accuracy. More details are given in chapter 5.

4. Controller
   generates control commands for the thrust system to reach a certain relative orbit. The implementation features multiple control methods for different use cases like formation maintenance or formation change manoeuvres. More details are given in chapter 6.

5. Thrust system
   takes the control input and applies it to the thrusters, which results in a contribution to the physics of the dynamic model of the propagator. Obeys thruster capabilities, power consumption and mass loss. It can be set to test mode to allow and forward any input to the physical propagation model. In normal mode the input is capped at the maximum rate of the thrusters. Also the maximum turning rate of the satellite is obeyed, since all thrusters are directed in the same direction. This prevents an instantaneous change of the thrusting vector. The thrust model includes accurate mass-loss and power consumption calculations based on the applied acceleration.

6. Inter-Satellite Link
   communicates with the other satellites in the formation and updates the relative
   state. Depending on the configuration, this can be a perfect real-time link (meaning
   the satellites know at all times the true relative positions and velocities of each
   other) or a link which updates information from time to time. In the future, it
   can be extended to incorporate a complex communication model like an OMNET-
   based simulation. The default state-exchange frequency is set to one time per
   orbit. Continuous communication is highly unlikely for the *NetSat* mission with
   the current design – the use of directed antennas and position control with directed
   thrusters may not be performed at the same time.

7. PCDU (Power Control and Distribution Unit)
   loads the battery in sunshine phases, obeys the estimated power consumption
   of the on-board computer and the power consumption of the active subsystems.
   Has to be the last subsystem to be executed to account for all current changes in
   consumption. Can also raise warnings on low battery levels and deactivate greedy
   (but not critical over a short time period) consumers like the thrust system.

Further important subsystems like housekeeping or ground station communication are
not part of this work, because focus was set to autonomous orbit propagation and
control. This is only marginally impacted by the two systems stated above. If needed,
they may be easily integrated in the future due to the expandable nature of the whole
model.

4.2.2   Data handling

Internal satellite data is handled and processed by a dynamic database, generated from
specially formatted CSV files. This database is structured into tables (one for each
subsystem) and contains all parameters which need to have a configurable value at
start-up or which impact multiple subsystems. Thereby this database is the only way for
subsystems to exchange or forward data between each other. This renders a subsystem's
implementation totally independent of other parts of the satellite, resulting in a modular
model. All parameters are stamped with their last update time and may be locked
to prevent further value changes. A single parameter can be a simple atomic value
like a floating point number, an array of atomic values or a complex datatype like an
orbit definition. A list of all available types is provided in appendix E. If needed,
further datatypes may be added by defining parse- and copy-methods for the type.
The implementation also features event-driven interaction, i.e. the database calls an
event handler in a subsystem if a certain parameter changed. The database is directly
connected to the debug interface to visualise real-time data dumps (see section 4.4).
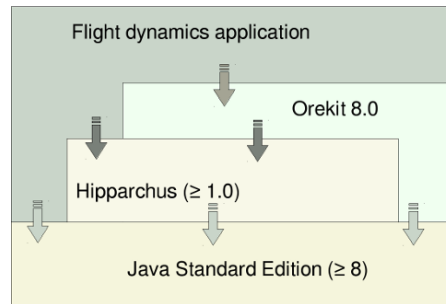
FIGURE 4.2: Propagator (Flight dynamics application) and OREKIT interaction. Source: http://www.orekit.org

4.3 Orbit propagation

The iterative orbit propagator handles all satellites equally (e.g. does not distinguish between chief and deputy s/c) and propagates their absolute orbits simultaneously for each time step. It is based on the open-source orbital dynamics framework OREKIT, which is a pure Java library and only depends on the Hipparchus mathematics library (Hipparchus, 2016).

4.3.1 OREKIT interface

OREKIT provides packages for date & time handling, frame transformations, ODE integration, attitude handling and perturbation force models. However, it does not support multiple satellites or relative state descriptions. The developed orbit propagator is the basis of the flight dynamics application which sets up on OREKIT, but also has access to the underlying mathematics library. The schematics of this connection is depicted in figure 4.2. Developed extensions include multi-satellite-support, configuration via CSV files, thrust force models and the interface to the previously mentioned satellite model. The instantaneous state of each spacecraft is defined by its osculating **pv**-vector and its mass. The dynamics of the state are represented by ordinary differential equations (ODEs) obeying gravitation, perturbation forces and inertial satellite forces like thrust. To propagate the state, these equations (with their initial values comprised by the spacecraft states) are converted to match the format of Hipparchus. Figure 4.3 depicts the propagation process in detail. The bold grey arrows are comprised of the current environmental settings and all satellite state vectors and follow the main execution loop. After each time step, the mapper brings this cumulated state vector into an ODE-friendly format. Within Hipparchus, the states are integrated using a numerical integrator and then back-transformed to spaceflight dynamics to give insight into the spacecraft states at the next timestep. After the simulation time has been increased, environment events (e.g. eclipse entering) and satellite-internal events are handled. Then, all waiting subsystems are executed in their respective order. Before the next propagation step begins, relevant data is sent to the debug interface.
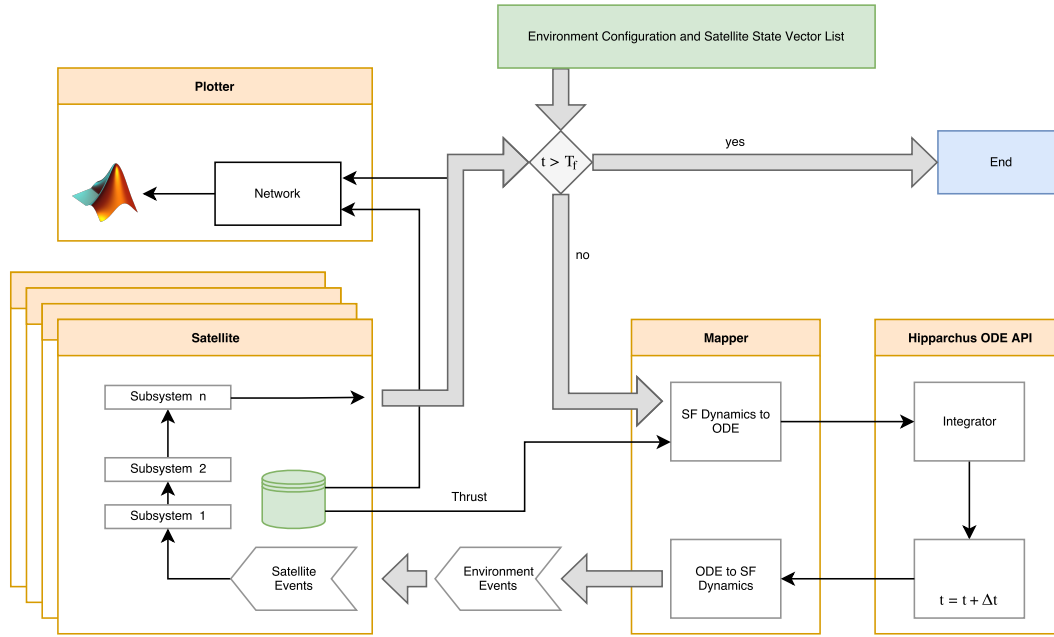
FIGURE 4.3: Propagation process in detail. The start is depicted in green, the end in blue.

4.3.2 Frame and date handling

The satellite states are integrated (e.g. propagated) in absolute osculating pv-coordinates. The utilised state vector is therefore equal to equation (2.2). For the ECI frame, the J2000 (or EME2000) reference was chosen since this is prevalent in orbital dynamics and already implemented in OREKIT (see section 2.1.1). The J2000 frame is defined in reference to Terrestrial Time (TT). Since other timescales are also important for various data input sources or desired output formats, conversion functions from TT to International Atomic Time (TAI) and Universal Time Coordinated (UTC) are exposed to the framework user. TAI is very important since it is the most accurate and regular timescale available and also used as a reference for the GPS time with a constant offset to GPS reference time of $19s$. TT is also defined via a constant offset to TAI:

$$\text{TT} = \text{TAI} + 32.184\,\text{s} \tag{4.1}$$

UTC has 86400 SI-seconds per day and is synchronised with TAI. To accommodate the slowing of the Earth's rotation, leap seconds are introduced at irregular intervals to keep the difference to TAI below $0.9\,\text{s}$ (Montenbruck and Gill, 2012). Whenever a state vector is utilised in the framework, the reference frame and the timescale has to be provided, and both are checked against their counterparts when combining different state vectors. This ensures compatibility and exchangeability of state vectors over all parts of the software. Additionally to the absolute OREKIT-inherent frame J2000 (see above), the software includes conversion methods between absolute and relative pv-vectors (equations 2.15 and 2.19), Keplerian to equinoctial and non-singular orbital elements (equations 2.30 and 2.28), any set of absolute orbital elements to differential orbital elements (equation 2.31) and relative orbital elements (equation 2.32). Whenever
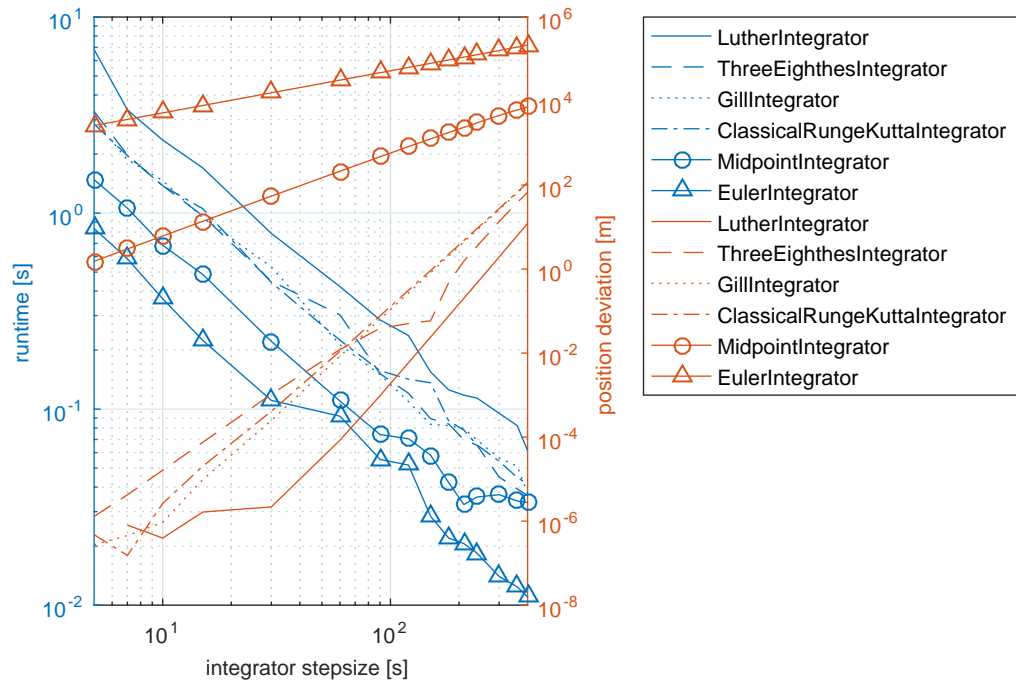
FIGURE 4.4: Propagator benchmark for different integrators and integration step sizes. Setup: one satellite propagated for four orbital periods on an Intel i5 machine. Computation time (runtime) on the primary ordinate, absolute accuracy (deviation of the final position obtained by most accurate integrator with smallest possible step size) on the secondary ordinate.

absolute orbital elements are used, they are internally represented as equinoctial orbital elements (EOE) to overcome singularities at small eccentricities (see section 2.1.2). Furthermore, relative Cartesian and orbital frames may be converted with equation (2.32). All orbital frames (both absolute and relative) may be provided in osculating or mean elements, depending on the current application or required input/output formats. The conversion is done with equations (2.55) and (2.64), respectively for absolute and relative conversions. Explicit formulations in terms of mean orbital elements can be found in appendix A and appendix B.

4.3.3 Integrator evaluation

Hipparchus offers a vast variety of different ODE integrators, from a simple Euler integrator to a complex sixth-order Runge-Kutta integrator. The integrators differ in runtime and accuracy. To evaluate the best-suited integrator, multiple implementations with different integration step sizes were tested. Figure 4.4 shows the results in terms of accuracy and runtime on a log-log-scale for all tested integrators. For the accuracy (position deviation after four orbits), the result of the most accurate integrator with the smallest step size is used as a reference position (or truth model). The test set-up was one satellite in a LEO orbit, propagated for four Keplerian periods on an Intel i5 machine. During propagation, Earth oblateness and atmospheric drag was taken into
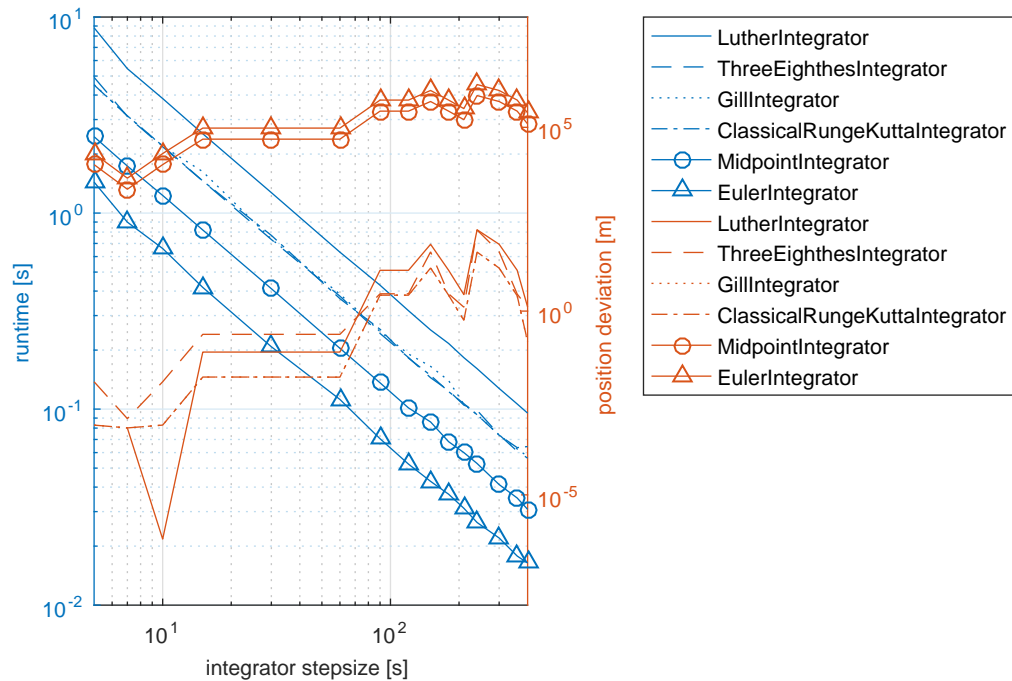
FIGURE 4.5: Propagator benchmark for different integrators and integration step sizes. Setup: four satellites propagated for four orbital periods on an Intel i5 machine. Computation time (runtime) on the primary ordinate, relative accuracy (accumulated deviation of the final position of the formation centre obtained by most accurate integrator with smallest possible step size) on the secondary ordinate.

account, while the satellite exerted no thrust. One can observe a positive exponential relationship between step size and accuracy as well as a negative exponential relationship between step size and runtime. Furthermore, to achieve an accuracy below one meter (which is the order of the sought position accuracy of the relative orbit determination system, see table 1.1), Euler and Midpoint integrator disqualify even for the lowest step sizes. To analyse the suitability, however, the relative accuracy between satellites is of much higher interest as the absolute accuracy. Therefore, the exact same benchmark was conducted again with a formation of four satellites in a $5\,\mathrm{km}$ PCO orbit, this time with relative position deviation (with respect to the formation centre) on the secondary axis of ordinates (figure 4.5). Each data-point was obtained by five individual runs to achieve higher accuracy in terms of runtime. Error bars for the runtime are neglected in the plot in favour of higher readability, since the orbit accuracy (which is deterministic and therefore the same for each run of a certain configuration) is of much higher interest. However, the dependency between integrator step size and runtime shows up more clearly compared to figure 4.4. As before, the two best integrators in terms of runtime do not have sufficient accuracy. Up to a step size of $60\,\mathrm{s}$, all other integrators result in a deviation below one meter. A further decrease in step size (down to $13\,\mathrm{s}$) does not lead to higher accuracy, while at the same time computation time rises. The sixth-order RK integrator (Luther integrator) has a 50% higher runtime compared to the three remaining integrators, which are almost identical in runtime (Three-Eights integrator, Gill integrator, Classical fourth-order Runge-Kutta integrator). Out of these, the Classical

Runge-Kutta integrator slightly outperforms the other two in terms of deviations. This lead to the decision to use the fourth-order RK integrator with a step size of $60\,s$ during orbit propagation in the software framework. The step size is also the shortest possible interval of consecutive executions of a subsystem's step handler method. If shorter periods are required for a certain subsystem, the integrator step size may be adapted at the cost of a higher runtime. This said, the stated $60\,s$ define only the upper bound of the usable step size value.

4.3.4 Included forces

The ODEs to propagate a satellite's state are composed of a superposition of all forces exerted at the satellite:

$$\mathbf{f_{total}} = \sum \left(\mathbf{f_K} + \mathbf{f_p} + \mathbf{f_s} \right) \tag{4.2}$$

where $\mathbf{f_K}$ is the Keplerian attraction force (equation 2.39), $\mathbf{f_s}$ is the sum of all satellite-internal forces and $\mathbf{f_p}$ are perturbing forces. In the current implementation, $\mathbf{f_s}$ only consists of the instantaneous output force of the thrusters. This could be extended to also incorporate rotation wheel forces, if they are not aligned with the main inertia axes of the satellite. According to section 2.2.2, of all perturbing forces only the non-spherical character of the Earth has a major influence on relative formation dynamics. This is modelled with the Holmes-Featherstone attraction model using the modified forward row method, whose implementation is part of the OREKIT framework (Holmes and Featherstone, 2002). The spherical harmonics of the Earth are modelled up to degree and order of ten, which is a good compromise between accuracy and runtime. Higher degrees are not useful for the used integrator configuration, since the added correction terms are below the integrator accuracy. To get a higher fidelity, also the very low impact of atmospheric drag was included. Even though section 2.2.2 showed the possibility to neglect this perturbation force, atmospheric drag gains influence in lower altitudes. Therefore, the propagator can also be used to simulate the final phase of the *NetSat* mission, where a low-altitude graveyard orbit or a possible re-entry is sought. The OREKIT inherent implementation of the modified Harris-Priester atmosphere model was chosen, since it combines high computation speed with relative accuracy. It uses solar activity dependent altitude-versus-density tables (Montenbruck and Gill, 2012).

The influence of the non-spherical shape of the Earth on the relative position of two satellites is shown in figure 4.6. The two images depict the relative position of a satellite over the time of half a day. The satellite is in a $5\,km$ PCO orbit around a virtual centre. The absolute orbit is the nominal *NetSat* orbit ($T = 97.5 min$). This leads to slightly more than seven revolutions in twelve hours. Image (I) shows this period in all three components of the Hill-frame position vector. In image (II), the satellites were propagated in the same manner, except that the J-terms of the Earth were taken into account. The period of the position components stays unchanged, but one can clearly see a vertical shift of the y-component over time. After half a day, the difference in comparison to the unperturbed propagation is as high as $350\,m$, or 7% of the baseline. This makes it
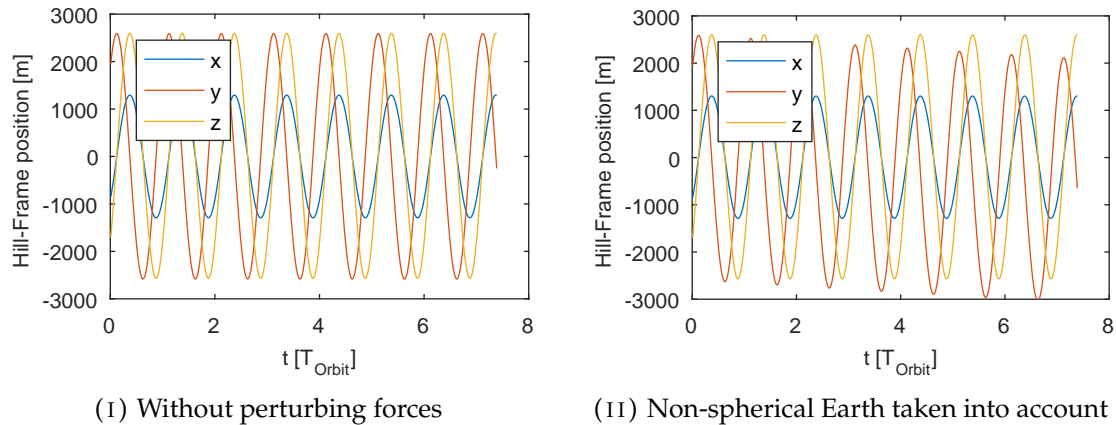
(I) Without perturbing forces

(II) Non-spherical Earth taken into account

FIGURE 4.6: Relative position in Hill-frame of a $5\,\mathrm{km}$ PCO formation (one satellite around virtual centre) for twelve hours.

obvious that this effect may not be neglected for the on-board propagator. Figure 4.7 shows a 3D-representation of the perturbed trajectory over time. The J-terms-influence continuously perturbs the orbit and shifts it in the negative y-direction, while the other two components stay nearly uninfluenced. This result is in accordance with the theoretical background of section 2.2.2. When the differential atmospheric drag is also included in the propagation process, the final state vector hardly differs from the result above. The difference after half a day is below $10\,\mathrm{m}$, around 0.2% of the baseline. The velocity part of the state vector is altered by less than $5 \times 10^{-4}\,\mathrm{m\,s^{-1}}$ over twelve hours. Although this force will not be part of the on-board propagator, this small influence will be included in the absolute OREKIT propagation process to gain the highest possible accuracy.

4.4 Debug interface

The debug interface is realised as a UDP client, which writes real-time data dumps to the network interface, packed into an extensible protocol. The data dumps are solely represented by floating point arrays for all datatypes (e.g. a one-field array for an atomic double value and a six-field array for an orbit definition, consisting of the six Keplerian parameters). The count and meaning of the debug output for each datatype of the database can be found in appendix E in the *Output* column. Any combination of parameters from the satellite databases may be marked as debug output by setting a flag in the database. The tri-state-flag may be any of *no debug output*, *debug output grouped by parameter*, or *grouped by satellites*. When the propagator is initialised, it sends a network message with the names of all parameters to be debugged during the propagation process. Then, after each time step, all parameters are sent as an array of floating point numbers in the order of their priorly sent names.

Furthermore, any information may be sent over the debug interface when a message type is defined for the desired data (as has been done for the database dump). This also allows to watch simulation metrics which are not part of the satellite model. Since
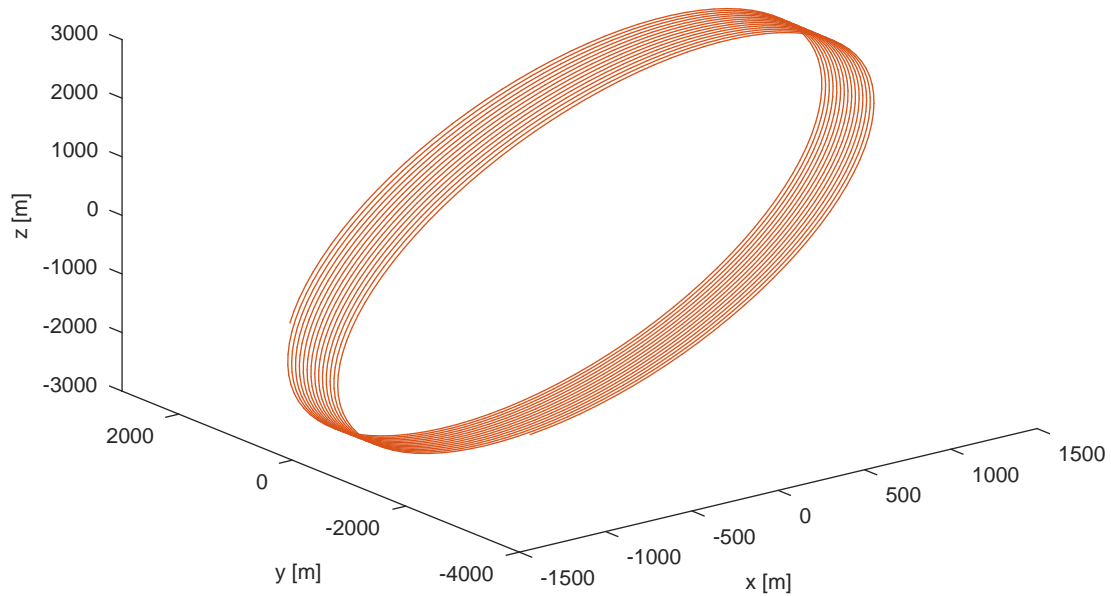
FIGURE 4.7: 5 km PCO orbit propagated for one day.

single messages may be larger than the maximum size of a UDP package, a message abstraction layer has been included. Data is sent packed into a message protocol, as defined by table 4.1. Each message is split automatically by the client into multiple network packages, when it is larger than the maximum UDP package size.

TABLE 4.1: Network message protocol (all parameters except *payload* are integers).

Parameter	Size [byte]	Description
ID	4	unique identifier (auto-incrementing)
TYPE	4	message type
TSIZE	4	total payload size of message
NPKG	2	number of packages in this message
PID	2	identifier of the current package
DSIZE	4	data (payload) size in this package
OFFSET	4	offset of this package's data in message
PAYLOAD	DSIZE	(part of) actual message data

The debug server waits until he receives all packages of a certain message, only then it is processed. The server forwards received messages to a message processor, which displays the content of the messages. At the moment, two different processors are implemented. The first one is a simple text-based processor, which displays all received values to the console and can also save the data to CSV-formatted text files on request.

The second one is a graphical processor, which displays all data in MATLAB graphs. When it receives data from the satellite databases, data streams from all satellites are combined and visualised, ordered by parameter or satellite (depending on the flag). Figure 4.8 denotes the relationship between ordering style and output, which results in
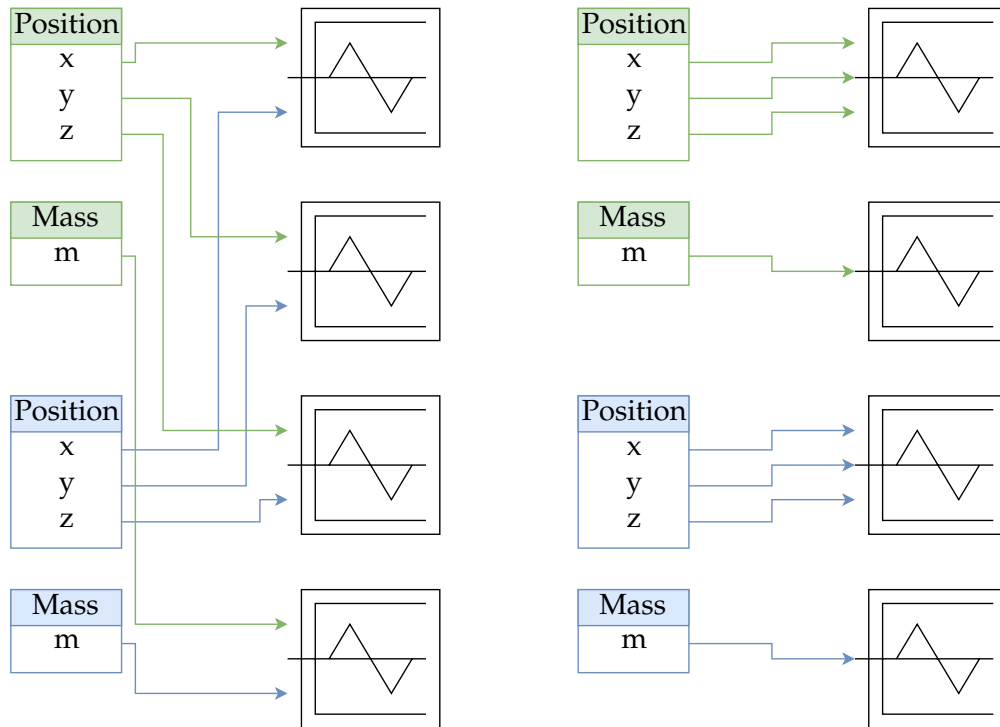
FIGURE 4.8: Two different methods to group atomic debug values –
the left-hand side illustrates grouping by satellites, the right-hand-side
grouping by parameter. Each colour represents the database of one satel-
lite.

different grouping of the atomic values. Depending on the situation or simulation task,
any combination of these two may render useful. Plotting routines for other message
types have to be added separately. At the moment, there are also routines to visualise
absolute and relative orbits in 3D space and thrust profiles.

Chapter 5

Relative propagation

One focus of this thesis is the on-board relative orbit propagator. It uses the theoretical background developed in section 2.3. The on-board propagator predicts the relative state vectors of the satellite in reference to all other satellites of the formation or in reference to the formation centre, depending on the configuration.

5.1   Overview

To control a satellite formation, each satellite has to have knowledge about the positions and velocities of the other satellites. Following the definition of section 2.1, these state vectors are represented in a common local frame, either based on orbital elements or Cartesian coordinates. An absolute orbit propagator is not part of the satellite model, since absolute orbit control does not lie in the scope of this work. The propagator is realised as a single configurable subsystem and integrates into the whole satellite model as explained in section 4.2.1. It is part of the main control loop and executes its step-handler as depicted in figure 4.3. The implementation follows a two-tier structure. The first part integrates with the satellite and controls database access. The second part only contains the bare mathematics for propagating the relative orbit. By this, the active STM may be changed easily.

All on-board components are limited in computational resources and memory. The propagator was developed in an iterative process, starting with a very simple dynamic model. This model was consecutively extended to incorporate higher-fidelity dynamics. This increases computation time and accuracy. The development process terminated in the final implementation once the desired accuracy for the *NetSat* mission was achieved.

The input for the propagator is the true (measured) relative state at some time instant t_0 in the past. The objective is to estimate the relative state at the current time instant t_1. As stated in section 4.2.1, most probably there will be no permanent inter-satellite communication. In a communication period, the satellites exchange knowledge about their orbits, letting them measure the instantaneous relative state. This measure can be obtained from multiple absolute orbit measurements or from direct relative distance measurements. The measurement is provided to the satellite model by the OREKIT propagator as absolute **pv**-vectors. A noise model in series adds a configurable level

of uncertainty to the state to simulate real inputs. The instant of the last relative state update will be t_0. The output of the propagator is the current relative state and is distributed to the other satellite subsystems via the global satellite database described in section 4.2.2. Depending on the request, the propagator provides relative **pv**-vectors, mean or osculating relative orbital elements, and mean or osculating differential orbital elements.

If not stated otherwise, the propagator suitability and accuracy will be examined at a $5\,\mathrm{km}$ PCO orbit (see section 3.3). Without loss of generality, this relative configuration with only one satellite orbiting the virtual centre is used for assessment. For more precise analyses, larger or other formations will be used when applicable. Following the general description of equation (3.2), the ROE state vector of one satellite in a $5\,\mathrm{km}$ PCO orbit is

$$a_0\boldsymbol{\delta o}_{\mathbf{PCO5}} = \begin{pmatrix} 0 & 1291 & 0 & 0 & 2582 & 348.6 \end{pmatrix}^T \; [m] \qquad (5.1)$$

Its $\mathscr{H}$-frame vector over twelve hours (without and with perturbing forces included) is shown in figure 4.6. The corresponding 3D-trajectory for one full day is depicted in figure 4.7. To fulfil mission constraints and to perform the sought formation baselines introduced in section 1.2, a relative accuracy below 1% of the formation baseline is intended. Communication to exchange state vectors should take place at least once per orbit. But even if communication fails for a few periods, the satellites should still be aware of their relative positions. This induces the demand on the error stability to remain at the stated level for multiple orbital periods. To make even small formation baselines possible, it is desired to maintain the error level below 0.1% of the baseline for at least one Keplerian period.

5.2   Circular motion model

The simplest propagator is based on the Hill-Clohessy-Wiltshire equation (2.73). Its solution presented in equation (2.75) is a fully qualified state transition matrix (STM) to propagate the orbit for arbitrary time intervals. It is based on a circular orbit model and neglegts all eccentricity-induced terms in the propagation process. Furthermore, it does not include any perturbation terms. As derived in section 2.3.1, it should provide a decent level of accuracy for low eccentricity orbits. Figure 5.1i shows the absolute deviation over two orbits for a circular reference orbit, when perturbations are neglected. The maximum error per axis is $2\,\mathrm{m}$, which is a negligible relative error of 0.04%. When the absolute reference orbit only has a very small eccentricity (like the nominal *NetSat* orbit), the error rises rapidly (see figure 5.1ii, note the different scaling of the ordinates). For a reference eccentricity of $e_0 = 0.007$, the relative error rises to 4.7%. Further analysis showed a strictly linear relationship between reference orbit eccentricity and maximum

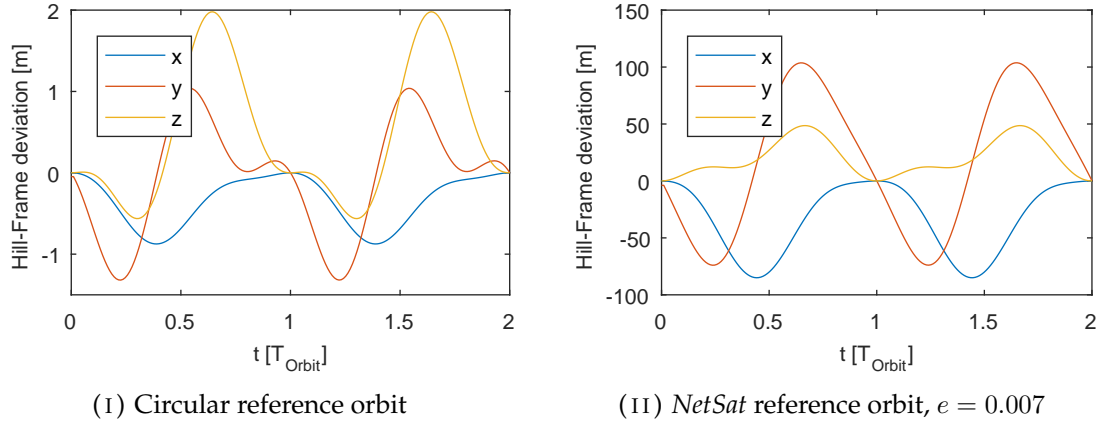(I) Circular reference orbit (II) *NetSat* reference orbit, $e = 0.007$

FIGURE 5.1: Absolute position error in Hill-frame when propagating with the HCW solution for different reference orbits.

relative error of the HCW-propagator. The relation is described with the (almost) origin-crossing linear fitting function

$$\max \left\{ a_0 \frac{\|\boldsymbol{\delta o_{\mathbf{real}}}\| - \|\boldsymbol{\delta o_{\mathbf{hcw}}}\|}{\|\boldsymbol{\delta o_{\mathbf{real}}}\|} \right\}_{e_0} = 6.53 \, e_0 + 2.72 \times 10^{-4} \tag{5.2}$$

where $\|\boldsymbol{\delta o_{\mathbf{real}}}\|$ is the magnitude of the real ROE state vector and $\|\boldsymbol{\delta o_{\mathbf{hcw}}}\|$ the propagated one. This shows that even a small eccentricity as low as $e = 2 \times 10^{-3}$ leads to a deviation larger than 1% per orbit. The relation between relative error and formation baseline b is in the region of interest also linear with the fitting function

$$\max \left\{ a_0 \frac{\|\boldsymbol{\delta o_{\mathbf{real}}}\| - \|\boldsymbol{\delta o_{\mathbf{hcw}}}\|}{\|\boldsymbol{\delta o_{\mathbf{real}}}\|} \right\}_{b[km]} = 1.35 \times 10^{-4} \, b + 4.59 \times 10^{-2} \tag{5.3}$$

This function was obtained for the nominal eccentricity. The error is around 4.7% for the smallest possible formation. In the largest desired PCO configuration with a baseline of $100 \, \mathrm{km}$, the position error reaches almost 6% per orbit. Comparing functions (5.2) and (5.3) unveils the considerably higher influence of the eccentricity on the error. The baseline error is a result of the frame linearisation around the chief, which is the same for the eccentric models of the next section.

The two results above show that the HCW-propagator does not fulfill the error requirements for any of the desired formation configurations. Even a possible eccentricity lowering of the reference orbit would not lead to error constraint satisfaction. This demands a more sophisticated propagator, which is derived in the next section.

5.3 Eccentric motion model

State transition matrices for eccentric chief orbits were derived in section 2.3.2. The approaches either use the true anomaly as independet variable (TH-equations) or use
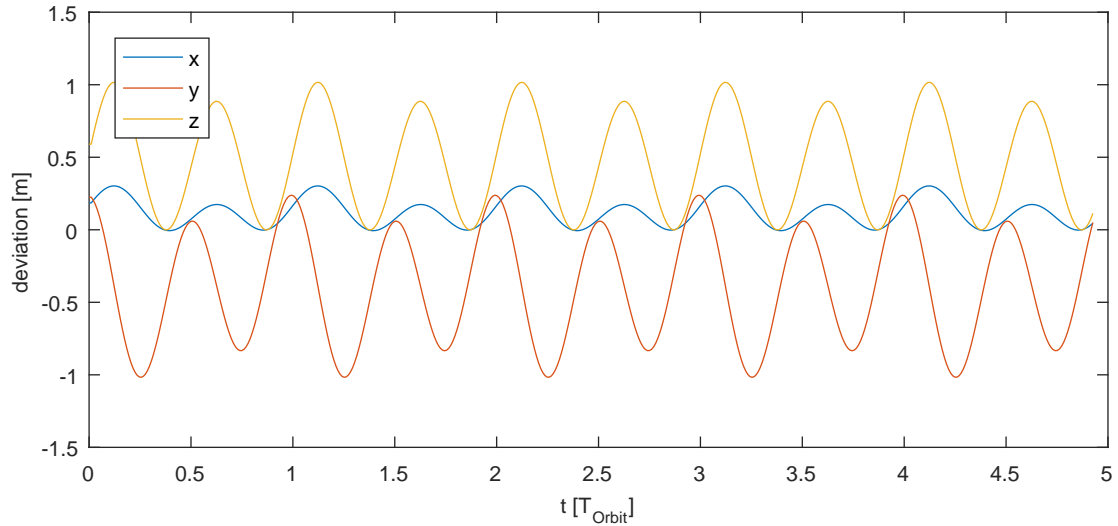
F I G U R E 5 . 2 : Absolute error for a $5\,\text{km}$ PCO orbit propagated with the simplified GA STM in nominal *NetSat* orbit (perturbation-free environment).

complex derivations like orbital element Jacobians. On top of this, the GA STM presented in section 2.3.3, which uses a geometrical orbit interpretation, can be simplified to correspond to standard TH-dynamics. Gim and Alfriend (2005) state in their derivation that the perturbation-free implementation of the GA STM leads to results as accurate as those obtained by the Carter STM (equation 2.83). For this reason, a simplified version of the GM STM (2.92) is used to analyse perturbation-neglecting eccentricity-obeying relative propagation.

Without considering perturbations, the matrix (2.89) to transform between differential orbital elements (DOE) and $\mathscr{H}$-frame coordinates simplifies to

$$\boldsymbol{\Sigma}\left(t\right) = \mathbf{A}\left(t\right) \tag{5.4}$$

since the perturbation parameter α evaluates to zero. Furthermore, there is no difference between a mean or osculating interpretation of the orbital elements. This distinction renders meaningless from the perturbation-free perspective as all DOE elements stay constant, hence

$$\mathbf{D}\left(t\right) = \mathbf{I} \tag{5.5}$$

The final implemented STM for the eccentric chief orbit is obtained by inserting equations (5.4) and (5.5) into (2.92):

$$\boldsymbol{\Phi}_{\mathbf{GA,Simple}}\left(t, t_0\right) = \mathbf{A}\left(t\right)\bar{\boldsymbol{\phi}}\left(t, t_0\right)\mathbf{A}\left(t_0\right) \tag{5.6}$$

The elements of $\mathbf{A}$ are part of $\boldsymbol{\Sigma}$ given in appendix C and the elements of $\bar{\phi}$ are given in appendix D. In the DOE-to-$\mathscr{H}$-matrix $\boldsymbol{\Sigma}$, the perturbation coefficient α has to be set to zero for this implementation. The superiority of this STM compared to the HCW-solution can be seen in figure 5.2. It shows the absolute error when propagating the $5\,\text{km}$ PCO configuration with the nominal *NetSat* orbit. The error stays well below 0.1% in
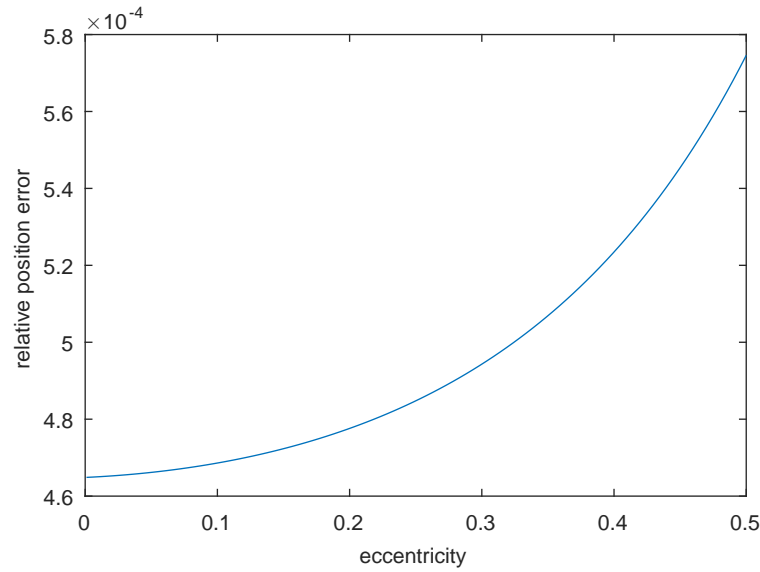
FIGURE 5.3: Relative error for a $5\,\mathrm{km}$ PCO orbit propagated with the simplified GA STM for different reference orbit eccentricities (perturbation-free environment).

every direction. The error again adapts linearly with the baseline and has a magnitude of about 1% per orbit for the largest desired PCO configuration with $100\,\mathrm{km}$ baseline.

The *NetSat* orbit has a very low eccentricity, which cannot be assumed to be constant. As absolute orbit control may not be guaranteed, the absolute orbit may change over time. To assure the applicability of the simplified GA STM independently of the absolute orbit, it was tested in an eccentricity range from 0 to 0.5. Figure 5.3 shows the result with the relative error on the ordinate. The simplified GA STM yields a non-linear relation between reference orbit eccentricity and propagation error. Even for the largest tested eccentricity value, the error stays well below acceptable levels. This robustness makes the selected STM predestinated for further investigation.

For the STM analysis in a realistic environment incorporating perturbing forces, the same setup like the one from figure 5.2 was chosen. Only the simulation environment was configured to represent the realistic environment. This means, the simulation environment was set up with perturbing forces as stated in section 4.3.4. Figure 5.4 shows the Cartesian position deviation in the realistic environment for six orbital periods. After this time, the error already reached 10% of the state vector magnitude. It is continuously rising without limits. The largest amount of the error is in along-track direction (y-axis). The nature of the error becomes more clear when the deviations in the propagated relative orbital elements are investigated (figure 5.5). All relative elements except δu stay within reasonable bounds below 0.4% for the first three orbits. According to the ROE definition in equation (2.32), the growing error is located in the relative argument of perigee or the anomaly. This perturbation effect has to be included in the motion model to prevent unbounded error growth beyond the predetermined level.
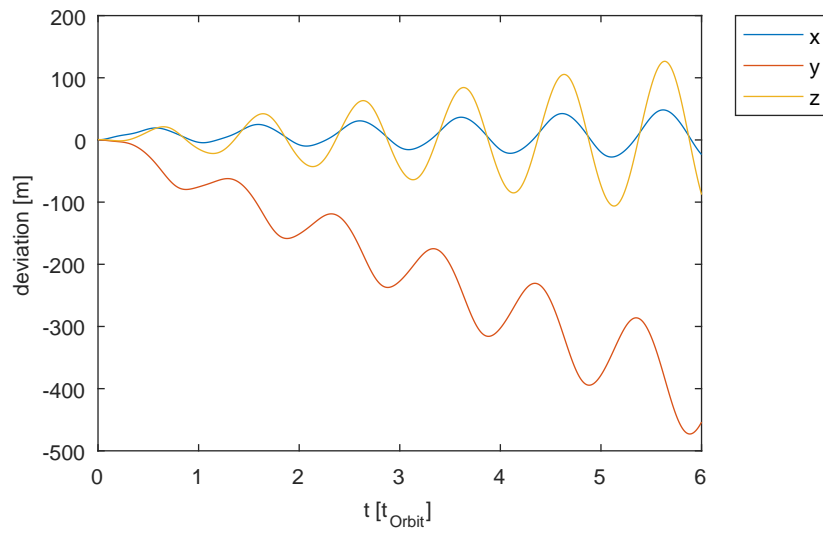
FIGURE 5.4: Absolute Hill-frame error for a $5\,km$ PCO orbit propagated with the simplified GA STM in nominal *NetSat* orbit (perturbed environment).
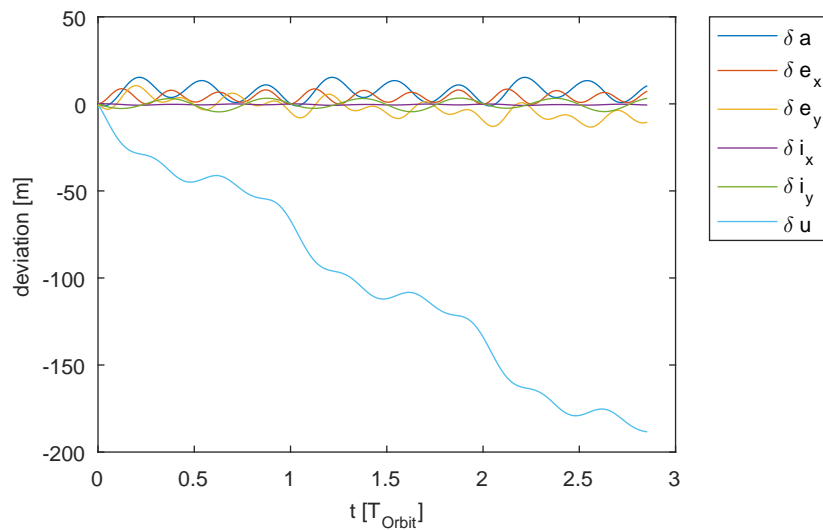

FIGURE 5.5: Absolute ROE-frame error for a $5\,km$ PCO orbit propagated with the simplified GA STM in nominal *NetSat* orbit (perturbed environment).

(I) ROE – all elements in $[m]$

(II) COE – all elements in $[rad]$. Except a $[m]$ and e (dimensionless)
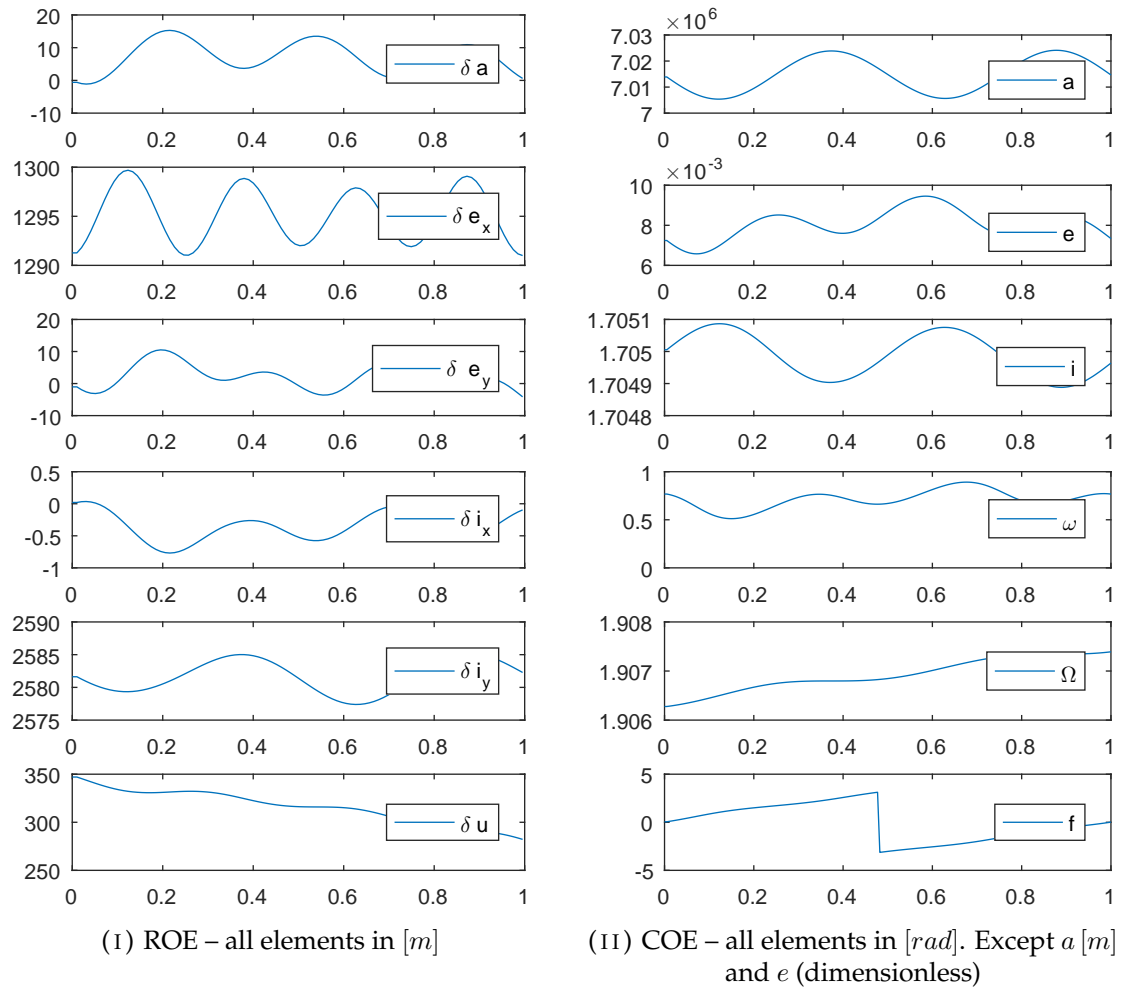
FIGURE 5.6: Perturbed relative and absolute orbital elements for one Keplerian period.

5.4 Perturbed motion model

Figure 5.6 shows the relative and absolute orbital elements over one Keplerian period of the deputy satellite in the realistic simulation environment. The alterations in figure 5.6i are in fact a snippet of the ROE deviations in figure 5.5. Since the motion model used to produce this trajectory does not incorporate any perturbations, the ROE state vector stays constant for all times. Also in figure 5.6 all absolute values except δu feature periodic motion. To analyse the error source, the absolute classical orbital elements are also shown for one Keplerian period (figure 5.6ii). The relative argument of latitude δu is dependent on the mean anomalies and thereby a function of the semi-major axis a. As depicted in the topmost plot of 5.6ii, the absolute value of the semi-major axis changes by around $20\,\mathrm{km}$ during one orbit. Deploying equation (2.25), this changes the mean motion by:

$$\Delta n = \left| \sqrt{\frac{\mu}{a_{max}^3}} - \sqrt{\frac{\mu}{a_{min}^3}} \right| = 4.44 \times 10^{-6} \tag{5.7}$$

FIGURE 5.7: Absolute Hill-frame error for a $5\,\mathrm{km}$ PCO orbit propagated
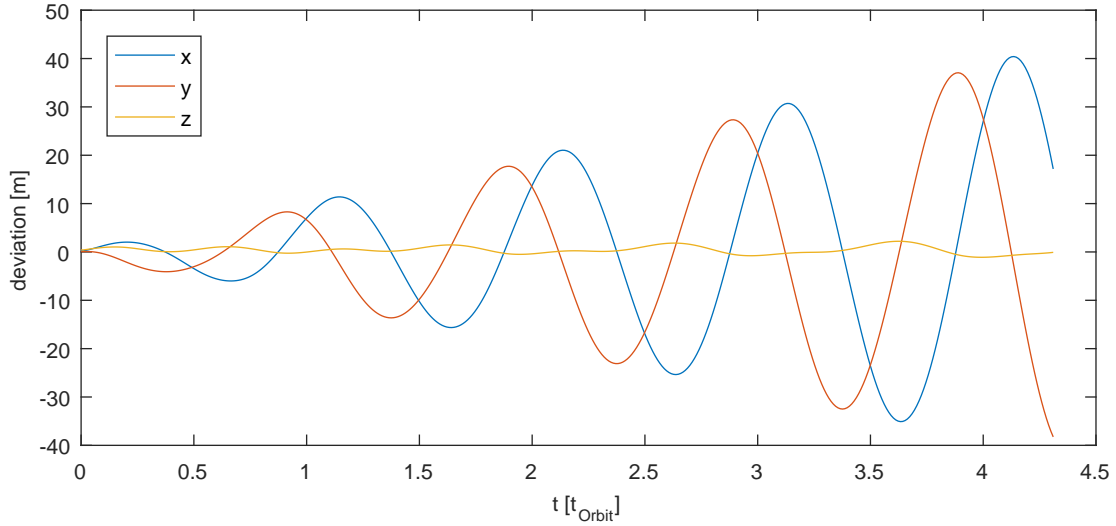with the GA STM in nominal *NetSat* orbit.

The error in mean motion results in an along-track offset after one orbit of

$$\Delta y = v\Delta T \approx 2\pi\sqrt{\frac{\mu}{a}}\frac{\Delta n}{n^2} = 190\,\mathrm{km} \tag{5.8}$$

This offset is by far larger than the error of the perturbation-free STM. Since the two
absolute orbits underlie similar instantaneous perturbation forces, their semi-major
axes vary with the same frequency in almost the same manner. The alteration in the
differential semi-major axis is around $20\,\mathrm{m}$. This value corresponds to the magnitude of
the curve in the topmost plot of figure 5.6i, as relative and differential semi-major axis
are equal by definition (see section 2.1.2). Inserting this difference in equation (5.8) gives
the maximum error estimate in along-track deviation after one orbit in local Cartesian
frame:

$$\Delta y_{max}^{\mathscr{H}} = 190\,\mathrm{m} \tag{5.9}$$

This value is higher than depicted in figures 5.4 and 5.5 and is only a worst case estimate,
since it depends on the instantaneous error in semi-major axis. This so-called "error"
is in fact the difference between the osculating and mean value of a. Mitigation of this
error source is addressed in the full version of the Gim-Alfriend STM (equation 2.92).
By regarding the state at t_0 in mean elements, the J_2-effect is filtered out. The initial
$\mathscr{H}$-frame state is transformed to differential mean elements and then propagated until
t_1 with the DOE-STM $\phi(t_0, t_1)$ from equation (2.87). The utilisation of the GA STM is
shown in figure 5.7. Compared to the simplified GA STM, especially the cross-track
error has greatly reduced. The error magnitude after one orbit is around 0.2% and thus
qualifies as a suitable STM in realistic settings. In a setting compared to the analysis
in Gim and Alfriend (2003) with an almost circular reference orbit, a baseline of $500\,\mathrm{m}$
and perturbing forces only comprised of Earth's J_2-J_5 terms (and without differential
atmospheric drag), the error after one orbit is at a comparable level. In contrast to the
above result, Gim and Alfriend could hold the error magnitude within the bounds posed
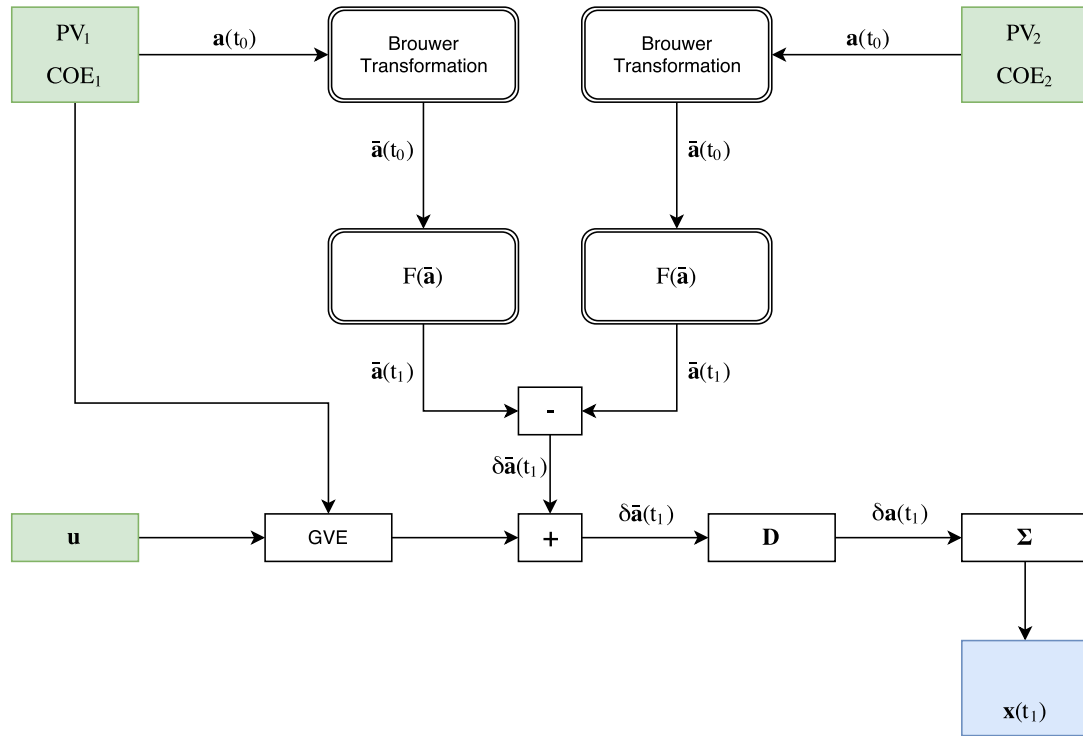
FIGURE 5.8: Procedure of the final on-board orbit propagator. Inputs
are green, the output is blue. Non-linear operations are in radiused boxes.

by the first orbit for over one day. The drawback of this very implementation is supposed
to come from the use of a simplified mean-to-osculation DOE transformation and minor
errors in the calculation of the differential anomaly. Since the initial state from OREKIT
is obtained in absolute non-singular orbital elements, many transformations take place
before the actual call of the STM. Further inspection revealed that the relative propagator
is very sensitive to numerical inaccuracies in the osculating differential anomaly.

Although the error level after one orbit is small enough to fulfil the requirements, it
grows too fast afterwards. This is a risk for periods without (or failed) inter-satellite-
communication and can raise state recovery costs in terms of delta-v. The two pos-
sibilities are to find an initial state computation with higher accuracy or to avoid the
anomaly-sensitive part of the STM. The latter option was chosen, since it lowers compu-
tational load through matching the new input requirements to already available data.

5.5 Modified GA propagator

The final implementation makes use of already available data as input sources. It fol-
lows the idea of the GA STM, but modifies different parts to accommodate accuracy
requirements and available input data at the same time. The satellites' absolute state
measurements will be obtained by GPS. This means, absolute **pv**-vectors are available.
By a simple transformation, the absolute Keplerian orbits of the satellites can be obtained
and are used as input. Following the idea of the GA STM and the absolute necessity
of this step as derived in the former section, the osculating orbits are transformed to

their mean counterparts using the non-linear Brouwer transformation (equation 2.55, explicitly given in appendix A). The mean orbits of both the reference satellite (or virtual chief) and the actual satellite performing the propagation are then extrapolated from t_0 to t_1. Assuming only J_2-perturbations, semi-major axis, eccentricity and inclination stay constant in mean element space. The other three elements are propagated with equations (2.65a), (2.65b) and (2.65c). Combining these with the mean motion n gives the mean element propagation function $\mathbf{F}$ to find the mean state at t_1:

$$\bar{\mathbf{a}}\left(t_1\right)=\begin{pmatrix}\bar{a}\\\bar{e}\\\bar{i}\\\bar{\omega}\\\bar{\Omega}\\\bar{M}\end{pmatrix}_{t_1}=\mathbf{F}\left(\bar{\mathbf{a}},t_0,t_1\right)\left(t_1-t_0\right)+\bar{\mathbf{a}}\left(t_0\right) \tag{5.10}$$

where

$$\mathbf{F}\left(\bar{\mathbf{a}},t_0,t_1\right)=\begin{pmatrix}0\\0\\0\\\dfrac{3}{4}J_2\left(\dfrac{R_E}{\bar{p}}\right)^2\bar{n}\left(5\cos^2\bar{i}-1\right)\\-\dfrac{3}{2}J_2\left(\dfrac{R_E}{\bar{p}}\right)^2\bar{n}\cos\bar{i}\\\bar{n}+\dfrac{3}{4}J_2\left(\dfrac{R_E}{\bar{p}}\right)^2\bar{n}\sqrt{1-\bar{e}^2}\left(3\cos^2\bar{i}-1\right)\end{pmatrix} \tag{5.11}$$

From the mean states at t_1, the differential orbital element set is obtained by subtracting the two absolute mean states. This differential state is then transformed to the osculating mean state using the differential mean-to-osculating transformation matrix $\mathbf{D}$ defined in equation (2.67). Its simplified explicit version is given in appendix B. This osculating state is finally transformed into the $\mathscr{H}$-frame with the full version of the $\mathbf{\Sigma}$-matrix stated in equation (2.89). With this usage, the perturbation factor α of $\mathbf{\Sigma}$ is set to $3J_2R_E^2$, its elements are given in appendix C. The final output is the Cartesian state vector in the local LVLH frame of the (virtual) chief. The whole workflow is depicted in diagram 5.8. This state transition procedure can be used for arbitrary time intervals without loss of accuracy. This means, there is no difference between multiple short orbit propagations or one long propagation step until the final date. When there is thrusting action, however, the instantaneous thrust vector has to be taken into account. Thrust is applied in the spacecraft's LVLH frame and can be transformed to an alteration in orbital elements with Gauss' Variational Equation stated in (2.97). This can be regarded as a further contribution to the differential elements set. By this fact, the thrust contribution is added to the differential orbital state vector at t_1. When the thrust plan for other spacecraft is known, their thrust vectors can also be added in this step to account for their active movement. The GVE is a function of the orbit at t_0, which differs vaguely from the one at t_1. The thrust is also assumed to be constant over one propagation period, inducing a lower limit on propagation frequency. The approach is in fact a zero-order hold
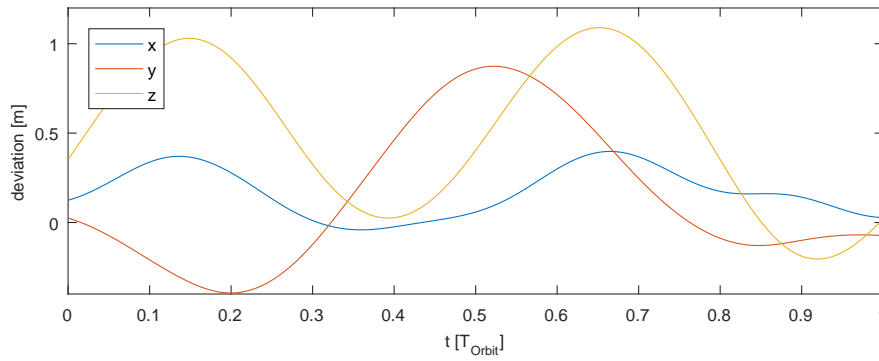
FIGURE 5.9: Absolute Hill-frame error for a $5\,\mathrm{km}$ PCO orbit propagated with the modified GA propagator in nominal *NetSat* orbit for one Keplerian period.
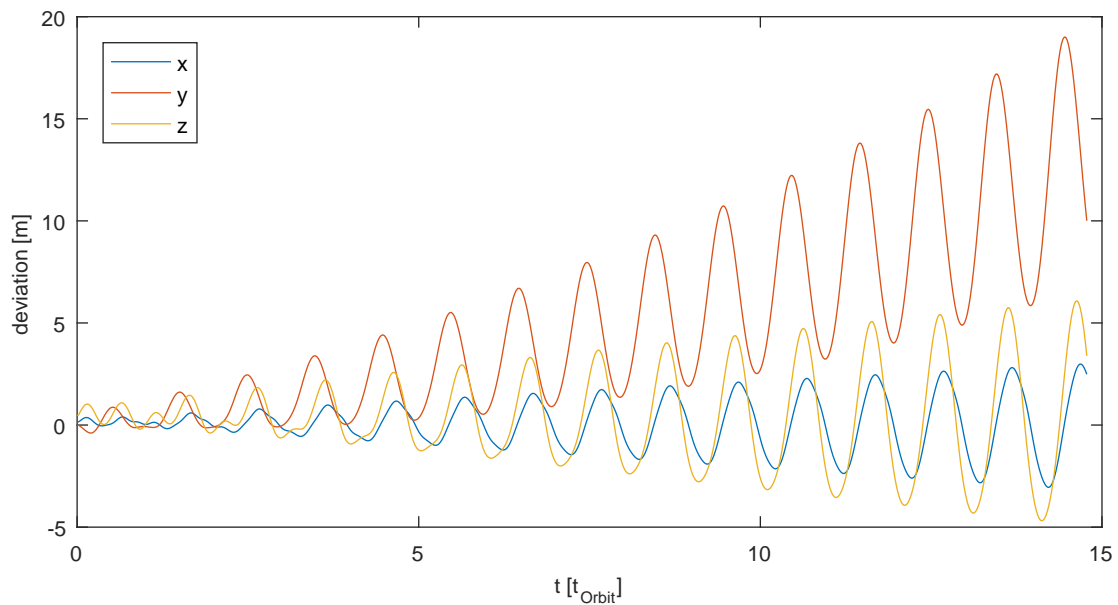
FIGURE 5.10: Absolute Hill-frame error for a $5\,\mathrm{km}$ PCO orbit propagated with the modified GA propagator in nominal *NetSat* orbit for one day.

assumption on the thrust input over the whole propagation period. For the concern of ultra low-thrust in the order of magnitude $1 \times 10^{-5}\,\mathrm{N}$ (like the *NetSat* satellites are supposed to have, confer equation 1.1), no mentionable impact on controller accuracy was observed. Even for multiple revolutions, the propagator deviation did not suffer from arbitrary thrust profiles.

The short-time performance of the developed propagator is shown in figure 5.9. It shows the Hill-frame deviation over one Keplerian period. In this time frame, the error does not exceed a magnitude of $1.5\,\mathrm{m}$, which corresponds to a relative error of 0.03%. This meets the requirements by far and may allow even close formation configurations.

The error stability is shown in figure 5.10. Although again the error magnitude is not constant (compared to the GA STM), it rises quite slow compared to the implementation
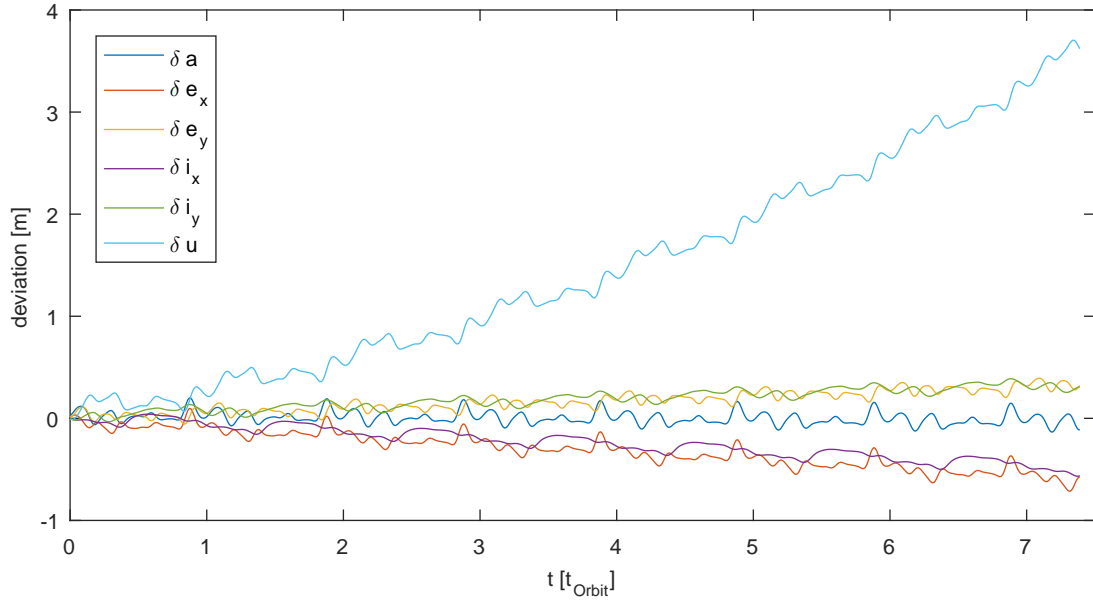
F I G U R E 5.11: ROE error for a $5\,\text{km}$ PCO orbit propagated with the modified GA propagator in nominal *NetSat* orbit for twelve hours.

of section 5.4. Within one full day without state vector updates, the error rises to 0.4% of the baseline, which is still below the desired maximum. The more restrictive error constraint of 0.1% for close formations is reached after five full orbits. This corresponds to roughly eight hours without inter-satellite-communication.

Figure 5.11 shows the error in relative orbital elements over half a day. Again, δu is by far the dominating factor. All other ROE elements stay within $1\,\text{m}$ of their real counterparts. If this single error in relative argument of latitude could by mitigated through finer osculating-to-mean transformations or higher numerical accuracy, the propagator may achieve even lower levels of error magnitude.

The error dependency on the formation baseline is depicted in figure 5.12. Above $7\,\text{km}$, the error grows quasi-linear. At the largest sought formation with $100\,\text{km}$ baseline, it is still below 1% per orbit. The more restrictive constraint of a 0.1%-level is not fulfilled above $12\,\text{km}$ baseline. This does not constraint possible formations, however, since the narrow error margin grows with formation compactness, i.e. small inter-satellite distances. At baselines above $12\,\text{km}$, the absolute distances between the satellites are large enough to not pose a hazard through navigation errors.

The error stability over different reference orbit eccentricities is shown in figure 5.13. Starting almost linear for very small eccentricities, the error rises slowly to the 0.1%-level for $e = 0.12$. This e-value is by far higher than the nominal *NetSat* orbit and assumed not to be reached. The error rises faster with growing eccentricity values and reaches 10% at $e = 0.45$. The modified GA propagator performs much worse for high eccentricities compared to the TH-solution or the GA STM. This is a consequence of propagating the averaged mean anomaly and drawing inferences from it about the differential osculating true anomaly.
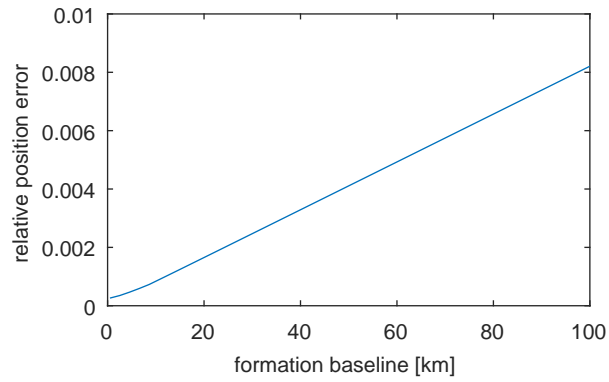
FIGURE 5.12: Relative error for various PCO orbits propagated with the modified GA propagator for different formation baselines.
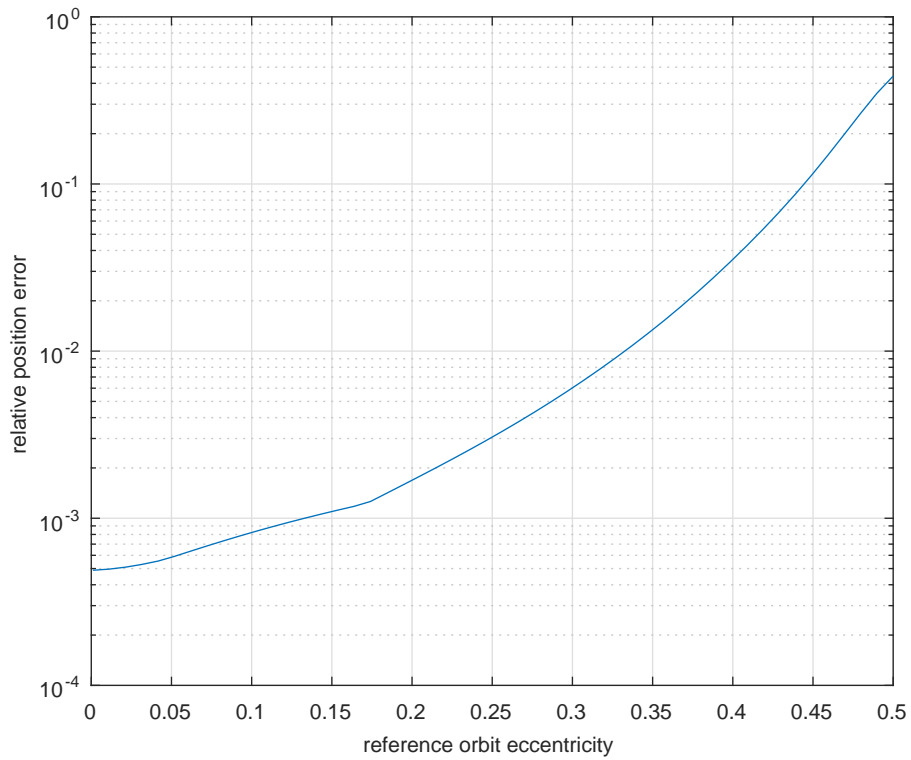

FIGURE 5.13: Per-orbit relative error for various PCO orbits propagated with the modified GA propagator for different reference orbit eccentricities.

(I) ATF

(II) CWF
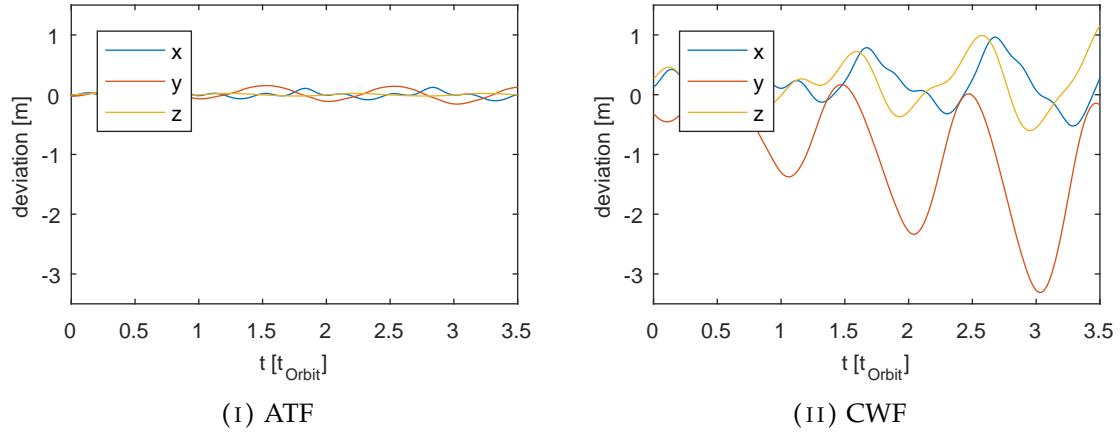
FIGURE 5.14: Absolute Hill-frame error for a different $5\,\mathrm{km}$-baseline formations propagated with the modified GA propagator in nominal *Net-Sat* orbit.

To prove the propagator versatility, its performance was analysed in other formation types. Figure 5.14i shows the Hill-frame deviation for a $5\,\mathrm{km}$ along track formation. The error is quasi non-existent and only arises from linearisation-errors in the direction of movement, since all satellites share the same absolute orbit. This one-dimensional formation will also be the initial configuration after deployment with an estimated baseline of $360\,\mathrm{km}$. Even for this large distance, the relative error stays below 0.6%. The three-dimensional cartwheel formation (CWF) is the most complex examined configuration. The absolute errors of the propagator in a CWF orbit are depicted in figure 5.14ii. The error magnitude is still below 0.1% for the first Keplerian period, but reaches this level within two full orbits. Compared to PCO, the error is around four times as high, but still at an acceptable level.

In this chapter, the relative error was given with respect to the formation baseline, i.e. the overall size of the configuration. The actual shortest distance between two satellites is a little bit lower. When this distance is selected as reference for GNC accuracy requirements, ATF and PCO are still possible at all intended distances. Only the CWF configuration may not be flyable with very small baselines. For the following chapter, the inter-satellite position update interval is assumed to be equal to the Keplerian period. This resets the error of the relative orbit propagator to zero every 97.5 minutes.

Chapter 6

Relative control

A number of relative orbit controllers were implemented in the software framework using the theory developed in section 2.4. This chapter begins with an investigation of the combined perturbation forces' order of magnitude the controllers have to counteract in maintenance mode. Based on the found characteristics, four different control strategies are analysed in terms of applicability, delta-v and accuracy. Furthermore, inter-formation trajectories for reconfiguration manoeuvres are examined. The chapter closes with a control plan proposal for all phases of the *NetSat* mission. If not stated otherwise, all sections use the nominal *NetSat* orbit as the absolute formation centre reference. Examined formations include PCO and CWF configurations with baselines up to $10\,\text{km}$ and ATF configurations without baseline limitations.

6.1 Optimal state vector design

For formation maintenance it is essential to reduce undesired relative motion to a minimum. The highest influence on undesired motion have unmatched semi-major axes. Per definition from chapter 3, all formation state vector sets have no difference in semi-major axes. When the state vectors are set up in the instantaneous osculating orbit of the (virtual) chief, they too are osculating and change over time (in contrast to a perturbation-free world, where ROE vectors stay constant). The difference in $a\delta a$ compared to the mean value can be as high as $20\,\text{m}$ (see section 5.4), leading to a drift in y-direction (in-track). Figure 6.1 shows the in-plane motion for one day for a four-satellite $5\,\text{km}$ PCO configuration, when set up in osculating ROEs. The along-track drift accumulates to around $1.5\,\text{km}$ for two of the satellites. It is important to note that this drift acts in opposing directions due to the shift of $180°$ in the respective eccentricity vectors. Most of this drift can be mitigated when the initial ROE vectors are set up with a mean reference orbit (see section 2.2.4). Figures 6.2i and 6.2ii show the 3D-trajectories for a $5\,\text{km}$ CWF configuration over one day (around 15 orbits) with initial osculating and mean reference. With the mean reference, the deviation compared to the initial ellipses is greatly reduced, which manifests in narrower trajectory bands. When the semi-major axes match, only perturbing forces drive the spacecraft apart. The only influence worth noting is the differential J_2-effect (see sections 2.2.2 and 4.3.4). Following section 3.5, the major part of this differential force can be oppressed with a small correction term

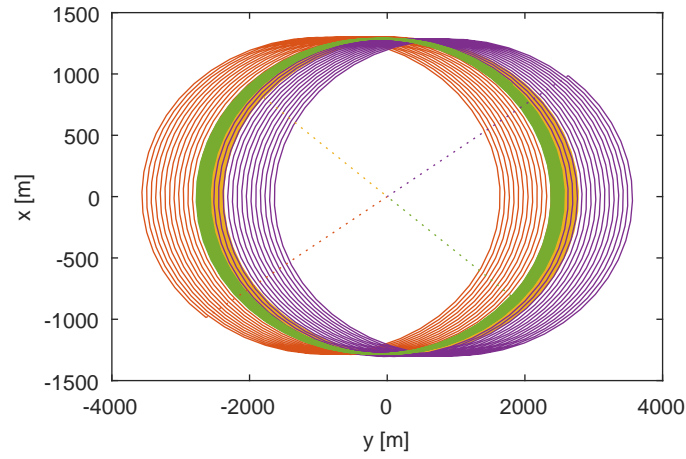FIGURE 6.1: In-plane motion for one day with osculating initial ROEs
(5 km PCO)

(I) Osculating ROE   (II) Mean ROE   (III) Mean ROE with δa-correction
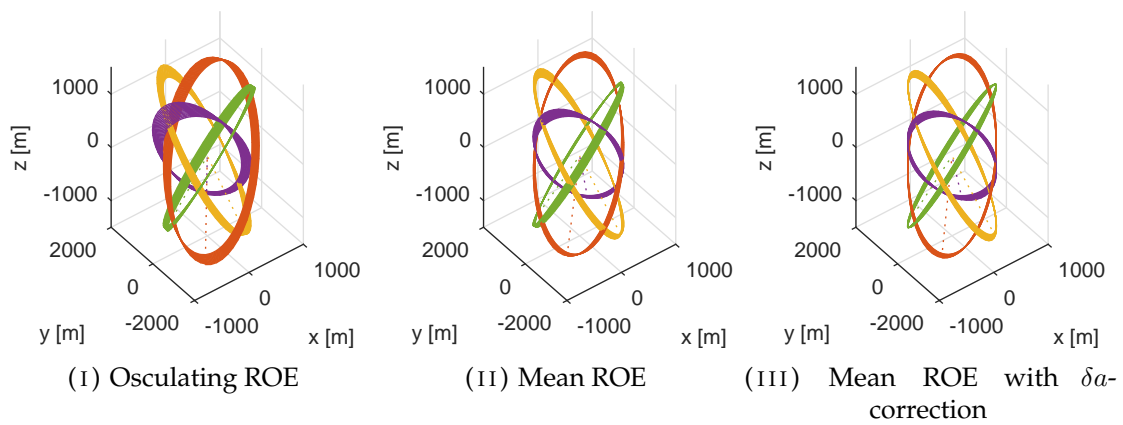
FIGURE 6.2: Relative motion for one day (5 km CWF) depending on
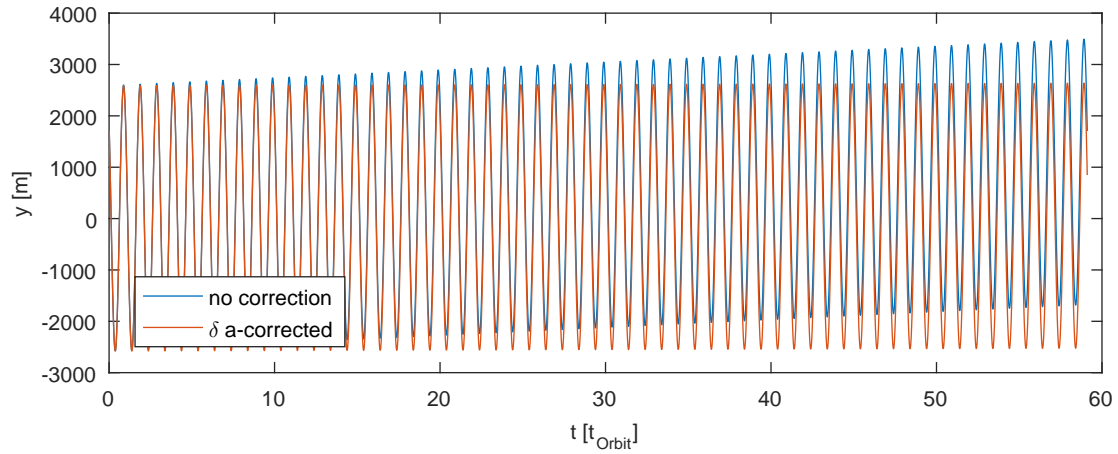initial state vector setup.

FIGURE 6.3: In-track motion for four days with(out) δa-correction (5 km PCO).

for δa obtained by equation (3.7a). This correction evaluates to a value between 0 and 2 meters for the examined formations and reduces undesired relative motion, which can be seen in figure 6.2iii. Compared to the uncorrected mean state vector, the trajectory variations over time are more balanced throughout the position in orbit. This can be seen best in the green trajectory, which has two equally thick bands in the δa-corrected case. Figure 6.3 highlights the importance of the δa-correction at the in-track relative motion between two satellites in PCO configuration. For PCO formations, the correction is usually higher than for CWF, resulting in a larger control effort reduction. The figure shows the relative along-track motion for four full days (almost 60 orbits). While the uncorrected spacecraft underlies a cumulated drift of 1 km, the drift is barely noticeable in the corrected case.

Having the above results in mind, the control input vectors must always be designed in mean element space. Furthermore, the δa-correction should always be implemented in the control target to further reduce maintenance delta-v consumption. The remaining part of this chapter always supposes the two preceding statements to be fulfilled without mentioning them. Another conclusion from the contrary influence of the main perturbation force can be drawn for the formation structure classification. Since the geometric centre of the formation stays nearly constant, i.e. the satellites suffer opposing drifts of the same magnitude, there is no big advantage in handling the formation as a single plant (MIMO) or as a cyclic structure. For now, all controllers will be developed in a chief-deputy configuration, whereby the virtual chief is always at the centre of the Hill-frame and the four satellites are orbiting around it (except ATF).

6.2 CLF-based control

Two different CLF-based controllers were implemented. The first one only controls the differential semi-major axis, while the second one is a full-state controller. The

(I) In-track control input

(II) Total delta-v
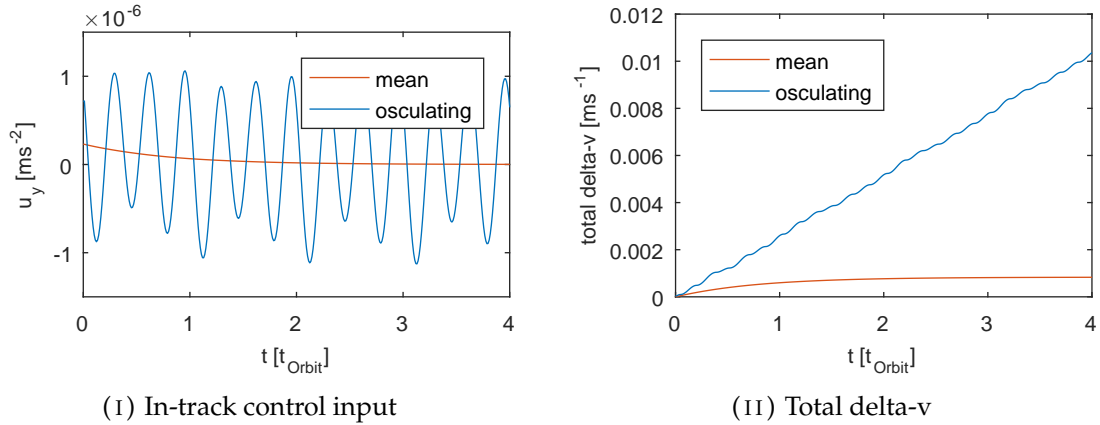
FIGURE 6.4: CLF-based δa-correction manoeuvre of $1\,\text{m}$ for osculating and mean control input.

controllers use the derivation of section 2.4.6. Since a control Lyapunov function only proves stability, the difficulty lies in finding the delta-v optimal CLF.

In the case of a sole δa-controller, a good CLF can be obtained from Gauss' variational equations (2.97) (Schaub et al., 2000). The first row of the GVE reveals that a control effort in y-direction has a hundred times higher influence on δa as its x-direction counterpart for the given reference orbit. Neglecting the latter one, a linear control law for correcting an offset in δa can be made up as

$$\frac{2a^2 p}{hr} u_y = -k\Delta a \tag{6.1}$$

where Δa is the difference between current and reference value for δa, i.e. $\Delta a = \delta a - \delta a_r$, and $k \in \mathbb{R}^+$ is an arbitrary scaling factor. The fraction is simply the control influence of u_y on δa. The stability of this law can be proven with the Lyapunov candidate function (2.118) in scalar form:

$$V(\Delta a) = 0.5\Delta a^2 \tag{6.2}$$

 Its derivative evaluates with the control law 6.1 to

$$
\begin{aligned}
\dot{V}\left(\Delta a\left(t\right), u_y\left(t\right)\right) &= \Delta a \Delta \dot{a} \\[2mm]
&\approx \Delta a \frac{2a^2 p}{hr} u_y \\[2mm]
&= \Delta a \frac{2a^2 p}{hr}\left(-k\right)\frac{hr}{2a^2 p}\Delta a \\[2mm]
&= -k\Delta a^2
\end{aligned}
\tag{6.3}
$$

which is clearly negative. Applying the maximum thrust level constraint (1.2) to the control law renders it non-linear, but keeps the CLF valid. Adding the constraint to the stability proof just yields a variable scaling factor k for the CLF, if the controller operates in saturated mode. Using this control law is the fastest way to counteract along-track
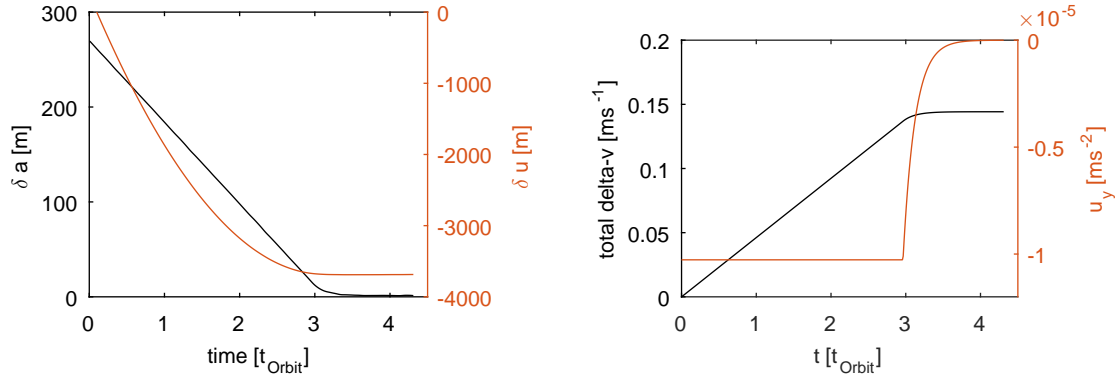
(I) Relative semi-major axis and argument of latitude.

(II) In-track control input and total delta-v consumption.

FIGURE 6.5: CLF-based initial drift compensation manoeuvre.

drift between any two satellites, since the spacecraft constantly fires until the semi-major axis is adjusted to the desired level (the reference value). The importance of using mean elements not only for setting up the initial state vectors, but also for the control law, is shown in figure 6.4. It depicts a δa correction manoeuvre of $1\,\mathrm{m}$ in a time frame of four orbits with control law (6.1) and scaling factor $k = 0.25n$. While the mean controller corrects Δa within two orbital periods and smoothly reaches an effortless state, the osculating controller constantly tries to correct the variations in semi-major axis. The variations are larger than the offset to be controlled, which leads to a continuously oscillating control acceleration. The mean controller performs well and puts all its effort in mitigating along-track drift when used for semi-major axis assimilation, making it a perfect choice for initial drift compensation after deployment of the spacecraft.

Simulations showed that the assumed maximal deviation in δa after an initially uncontrolled phase is roughly $270\,\mathrm{m}$ (see also section 3.1). This offset can be mitigated with the CLF-δa-controller within four orbital periods, as can be seen in figure 6.5. Shifting the reference position (Hill-frame origin) to the y-position of the spacecraft at manoeuvre start, δu increases for another $3.8\,\mathrm{km}$ during the δa-correction (figure 6.5i). The total amount of delta-v used to mitigate the complete offset is below $0.15\,\mathrm{m\,s^{-1}}$.

The CLF-based full-state controller directly uses the control law (2.117) with differential orbital elements as state vector. In this implementation, $\mathbf{B}$ equal the GVE (2.97) and $\mathbf{A}$ is the state transition matrix of the mean orbital elements (5.11). A suitable gain matrix $\mathbf{P}$ was determined heuristically and is given by

$$\mathbf{P} = \mathrm{diag}\left(\begin{array}{cccccc} 0.03 & 1 & 0.001 & 0.01 & 0.1 & 0.007 \end{array}\right) \tag{6.4}$$

The stated values proved to be more useful than a single-coefficient matrix of the form $\mathbf{P} = k\mathbf{I}$, since they exploit some characteristics of the GVE, namely the control throughput. The amplification of the error in a and M (first and last element) is very low to prevent δa-oscillations, which would cause along-track drift. This is necessary, because
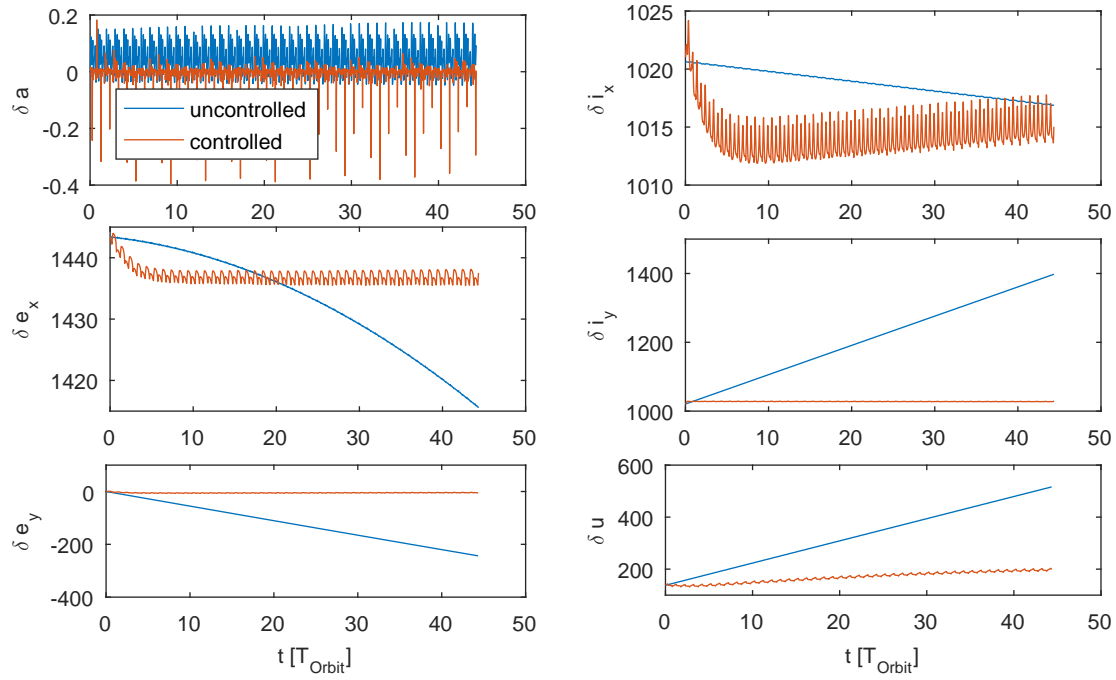
FIGURE 6.6: ROE state vector for three days with CLF-based full orbit
control (5 km CWF).

the controller is limited to maximum thrust levels and may therefore fail to correct a cou-
pled error in a and M at the same time. With the limiting factor, step four in the stability
proof (2.119) is not true anymore. For that reason, the implemented controller can only
be used for formation maintenance. Under very small deviations to the reference state
the controller operates in unsaturated mode and the stability proof still holds. Figure
6.6 shows the relative orbital elements of a 5 km CWF for three days with the CLF-based
full-state controller in comparison to the uncontrolled simulation. It has a steady-state
error in δe_x, leading to a fast change in δi_y in the beginning. All other elements are well
controlled and exhibit only small variations. Only δu rises very slowly with time owed
to the higher focus to δa in **P**. Figure 6.7 shows the corresponding thrust profile for the
first five orbits. It can be seen that the controller operates in saturated mode even in a
formation maintenance phase. This makes the control law error-prone, because stability
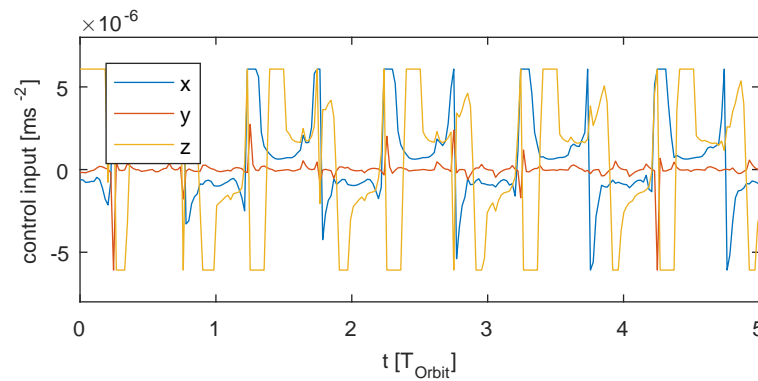
FIGURE 6.7: Control profile for five orbits for CLF-based full orbit con-
trol.

cannot be guaranteed. Furthermore, the spacecraft undergoes a constant control effort, which results in a non-optimal delta-v consumption, namely $0.0259\,\mathrm{m\,s}^{-1}$ per orbit for the given formation.

Further simulations revealed that the implemented full-state control law may only be used for very small-baseline formations with negligible differential perturbations to operate in unsaturated mode. Even then the variations in the ROE vector are still too large to provide high fidelity positioning. That is a direct result of the low-value gain matrix **P** to bring control input levels below the constraint value. The CLF-based control could be altered with a more complex control law. However, this process is non-trivial and a stable CLF-based law must not result in a delta-v optimal solution. Considering the simulation results, another control method has to be implemented.

6.3   LQR

A linear quadratic regulator (LQR) was implemented based on section 2.4.5. The design parameters of the LQR controller (2.98) are the two matrices **Q** and **R** of the cost function (2.100), which weight the state deviation **x** and the control input **u**. The controller uses Hill dynamics and is described in the LVLH-frame. The state error gain matrix was chosen as

$$\mathbf{Q} = \mathrm{diag}\begin{pmatrix} 1 & 50 & 1 & 0 & 0 & 0 \end{pmatrix} \tag{6.5}$$

This selection of **Q** only enforces the position constraint (upper left 3×3-submatrix), while neglecting any velocity deviations (lower right 3×3-submatrix). This is a valid approach, since the chosen cost function is an infinite horizon optimiser, where state derivatives may be bypassed. A higher error gain for the along-track direction (y-axis) proved to be useful to ensure orbital period commensurability. This property matches the observations from the CLF-based controller and was again applied in the also heuristically determined input acceleration gain matrix

$$\mathbf{R} = \tau\,\mathrm{diag}\begin{pmatrix} 1 & 30 & 0.1 \end{pmatrix} \quad \tau \in \mathbb{R}^{+} \tag{6.6}$$

The control input in z-direction was chosen to have the lowest penalty for the cost function, since it is decoupled from the other two coordinate axes. For the coupled x- and y-axes, the higher weight on y results in correction manoeuvres using thrust in x-direction when possible, leading to a more precise mean motion matching. The dimensionless factor τ globally weights the state error against the control input. A factor of $\tau = 5 \times 10^{-6}$ proved to be suited best, since it adjusts the influence of **x** and **u** to the same order of magnitude. The control gain matrix **K** is found by solving the continuous-time algebraic Riccati equation (2.114), what can be done with MATLAB's `care`-function. For the chosen input matrices, it evaluates to
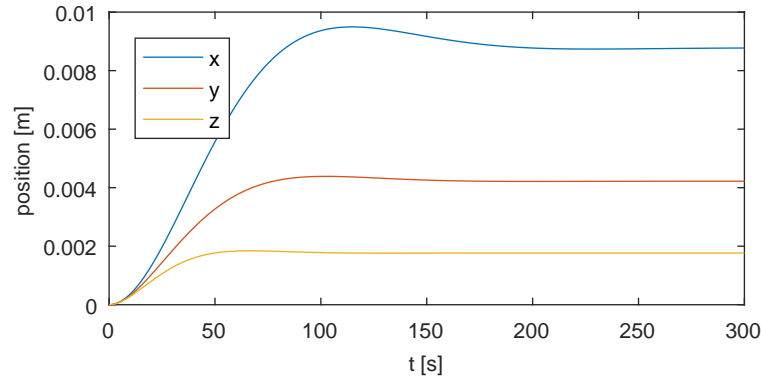
FIGURE 6.8: Step-response of the LQR controller for maximum-thrust-adjusted Heaviside input.
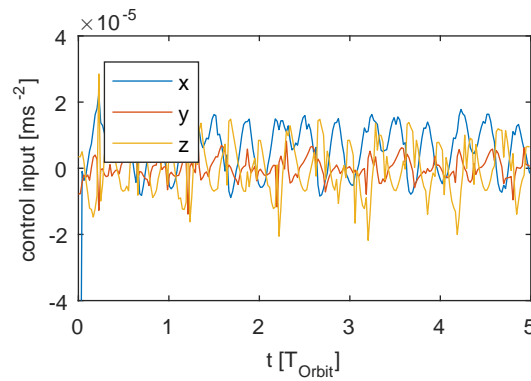
FIGURE 6.9: Generated thrust profile of the LQR controller.

$$\mathbf{K} = 1 \times 10^{-2} \begin{bmatrix} 0.0443 & -0.0581 & 0 & 3.152 & -3.398 & 0 \\ 0.0015 & 0.0568 & 0 & -0.1133 & 3.304 & 0 \\ 0 & 0 & 0.1413 & 0 & 0 & 5.316 \end{bmatrix} \qquad (6.7)$$

where the left half represents the gain for the position error and the right half the gain for the velocity error, which is also non-zero. It proves the hypothesis of a possible neglect of the state error derivatives in an infinite-horizon LQR law's gain matrix $\mathbf{Q}$. Though the velocity error throughput in $\mathbf{Q}$ is zero, it is considered in the final gain matrix. The control gain matrix $\mathbf{K}$ also shows the coupling of the x- and the y-axis, which is an inference from equation (2.70). Both, position and velocity errors, have a non-zero value in the axes-corresponding minor diagonals. All eigenvalues of $\mathbf{K}$ are negative with a non-zero imaginary part, leading to an asymptotically stable control law. The corresponding step response (figure 6.8) depicts the stability property with a very low steady-state error. It also reveals a rather fast (in the time frame of an orbital period) settling time below three minutes.

The results above were obtained with an unconstrained thrust input level. If the control input is restricted, the extended state transition definition (2.107) of the LQR does not hold anymore. Although it was attempted to lower the control input as far as possible with a very high τ-factor, it was not possible to keep the controller in its unsaturated
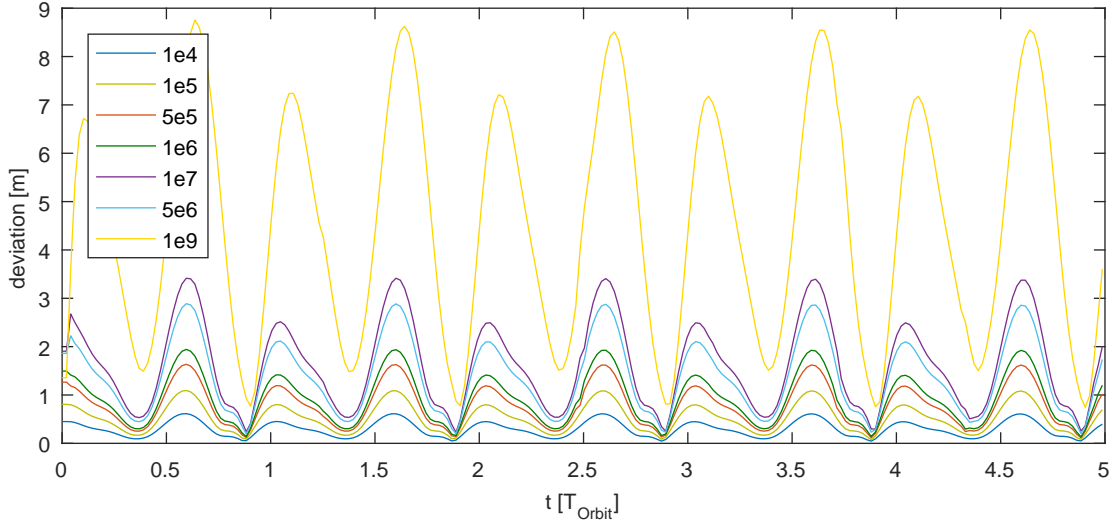
FIGURE 6.10: Deviation to reference governor for different **R**-matrix factors τ.
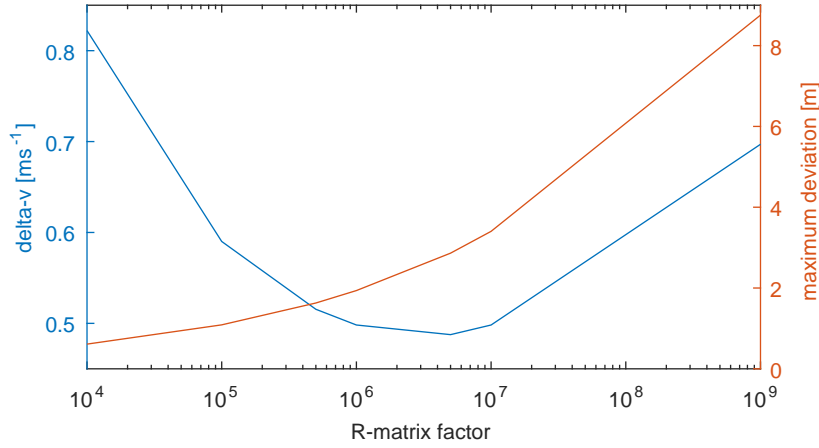
FIGURE 6.11: Maximum deviation and total delta-v (five orbits) for different **R**-matrix factors τ.

domain, when using a control input constraint (maximum level as defined in equation 1.2). As soon as the constrained LQR reached the saturated domain, the system became unstable and position errors increased exponentially. The lowest achieved thrust levels were around two times as high as the maximum level, as can be seen in the thrust profile 6.9 of a $5\,\mathrm{km}$ CWF for five orbits controlled with the unconstrained LQR. The higher input accelerations lead to an increased total delta-v consumption compared to the CLF-based controller. In case of the example configuration, the LQR consumed $0.098\,\mathrm{m\,s^{-1}}$ per orbit, which is almost four times higher than the CLF approach.

Despite not fulfilling the constraint, the control law gives valuable insight into long-term state deviations and upper bound delta-v estimates. Furthermore, the thrust levels are in the order of magnitude of the allowed maximum, giving the potential to find a modified LQR, which suits the constraints. The influence of the input weighting matrix factor τ on controller performance is shown in figure 6.10. It depicts the error-norm in
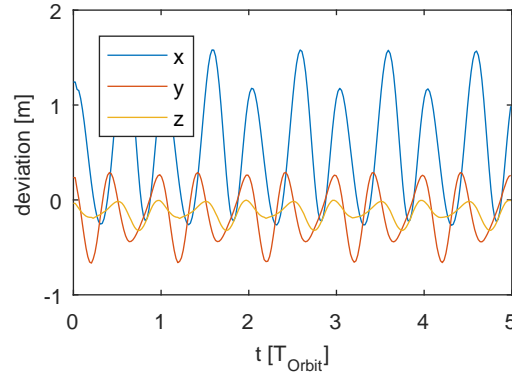
FIGURE 6.12: Hill-frame deviation from reference governor for five
orbits (5 km CWF) with LQR control.
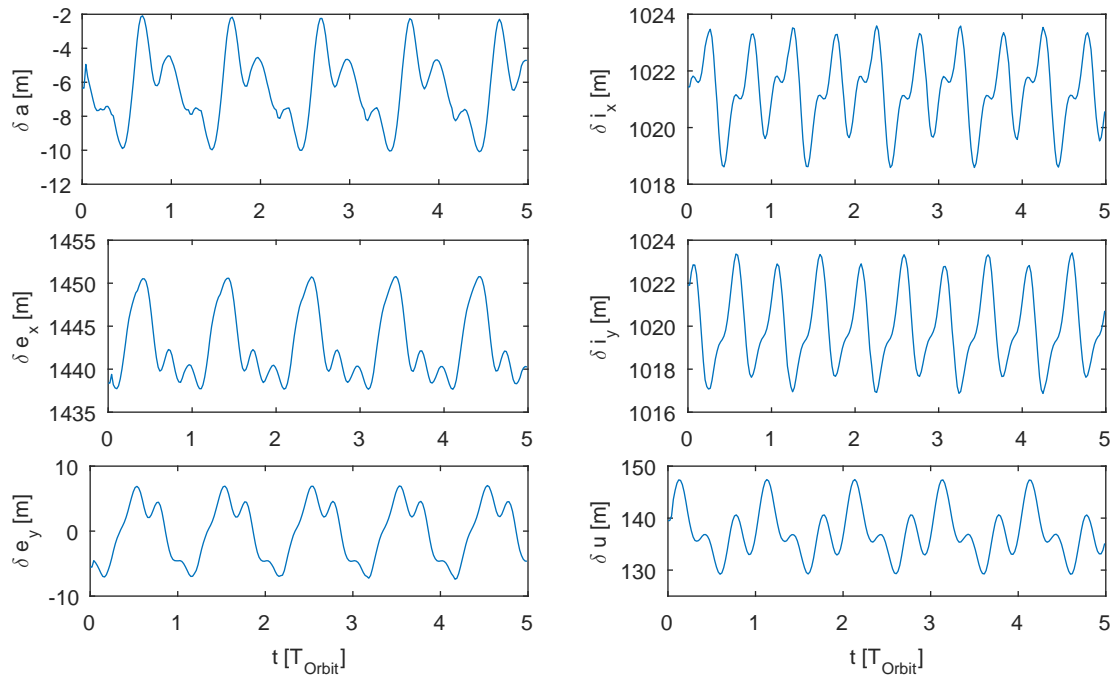
FIGURE 6.13: ROE state vector for five orbits LQR control.

Hill-frame from the reference governor for τ between 1×10^4 and 1×10^9. The lower the weight on the control input, the more thrust is applied to counteract even small position deviations, leading to faster deviation mitigation. The error analysis yields more meaningful when the cumulative delta-v is taken into account too. Figure 6.11 plots the maximum deviation levels of figure 6.10 as well as total delta-v over five orbits in dependence on the factor τ. Both figures prove the lower error levels for lower control input weightings. The delta-v consumption shows a valley-like profile and increases for low and high values of τ. Its minimum corresponds with the previously stated factor, which brings state error and control input to similar values ($\tau_0 = 5 \times 10^6$). Lower values for τ result in too high state error gains. On the other side, higher values admit much larger state errors as a result of slow error counteracting, leading to an increased delta-v consumption to counteract the larger error.

Another insight from the LQR controller is the coherence between regulated Hill-frame error and ROE state vector error. For the unconstrained τ_0-LQR, the Hill-frame error is shown for five orbits in the example formation in figure 6.12. The norm of the three lines corresponds to the respective light blue curve in figure 6.10. Although the error in any Hill-frame axis is constantly below $2\,\mathrm{m}$, the variations in the ROE state vector reach levels of up to $20\,\mathrm{m}$ for a single element (see figure 6.13). In Hill-frame, also the position derivative, which is not shown in the figure, is part of the state vector. Even small variations in velocity lead to an altered instantaneous relative orbit geometry when viewed in ROEs. This is emphasised at the example of the relative semi-major axis (upper left plot of figure 6.13), which is directly related to the x-axis in the Hill-frame. Even though they represent the same length in different frames, the relative semi-major axis varies six times as high as the x-coordinate in the Hill-frame (blue curve in figure 6.12). For that reason, error analysis for the final controller has to be done in a local Cartesian as well as a local orbital frame.

In conclusion, the developed LQR cannot be used for the current constraint set. Nevertheless, its analysis provides a first guess for design parameters of the MPC controller. Beyond this, it revealed the importance of conducting error analysis in different reference frames for a complete insight. There are also constraint-including descriptions of non-linear quasi-LQR controllers, which could be implemented in the future.

6.4 MPC

The model predictive controller (MPC) is the best performing one among the implemented controllers. This section starts with a detailed view on the final implementation. This is followed by two parts which investigate the controller performance in formation maintenance mode and during reconfiguration manoeuvres.

6.4.1 Implementation

The developed MPC based on section 2.4.7 is all in all the scalar cost function (2.136) subject to imperative constraints. The internal state vector of the controller is the mean DOE element set

$$\delta\bar{\mathbf{a}} = \begin{pmatrix} \delta a & \delta e & \delta i & \delta\omega & \delta\Omega & \delta M \end{pmatrix} \tag{6.8}$$

This set is used to match the output of the GVE (2.97), which is used for the control inputs. The complete controller description is given by:

$$\min_{\hat{\mathbf{U}}_k} \mathbf{C}^T \hat{\mathbf{U}}_k \tag{6.9}$$

subject to

$$\mathbf{A}_{eq}\hat{\mathbf{U}}_k = \mathbf{b}_{eq} \tag{6.10a}$$

$$\mathbf{A}_{ieq}\hat{\mathbf{U}}_k \le \mathbf{b}_{ieq} \tag{6.10b}$$

where $\hat{\mathbf{U}}_k$ is the concatenated control input over the planning horizon (2.133). Opposing to the deviation in section 2.4.7, the final relative orbit is enforced with the equality constraint (6.10a), whose reasons are stated later on in this section. All other restrictions are encapsulated in the inequality constraint. In one execution step, the MPC not only computes the control input for the current time step, but for all subsequent steps until the end of the planning horizon t_f. This also includes controller-internal orbit propagation over quite a large time to compute the matrix elements of the equality constraint. When using Hill dynamics in this time domain, the deviations grow too large for an effective control plan. Hence, in contrast to the preceding controllers, the MPC will use more exact dynamics in the equations of motion. The right hand side of the equality constraint (6.10a) is the final state error the controller has to overcome. The computation of $\mathbf{b}_{eq}$ is independent of the control input (i.e. the uncontrolled dynamics) and can be done beforehand the MPC. For $\mathbf{b}_{eq}$, even the eccentric dynamics derived in section 2.3.2 are too inaccurate. The ultimate solution is to use an own instance of the modified GA propagator (see section 5.5). With this propagator, the spacecraft position is propagated until the end of the planning horizon. The result is then converted to mean DOEs and subtracted from the desired mean DOE vector at t_f:

$$\mathbf{b}_{eq} = \delta\bar{\mathbf{a}}_{r,f} - \mathbf{\Phi}_{MGA}\left(\delta\bar{\mathbf{a}}_0, t_f\right) \tag{6.11}$$

where $\mathbf{\Phi}_{MGA}\left(\mathbf{x}, t\right)$ gives the state vector $\mathbf{x}$ at t with the method described in section 5.5. The left hand side of the equality constraint, $\mathbf{A}_{eq}$, equals equation (2.126a), which is repeated here for clarification:

$$\mathbf{A}_{eq} = \left[\begin{array}{ccccc} \mathbf{\Phi}^{(k-1,k)}\mathbf{G}_0 & \mathbf{\Phi}^{(k-2,k)}\mathbf{G}_1 & \cdots & \mathbf{\Phi}^{(0,k)}\mathbf{G}_{k-1} & \mathbf{0} \end{array} \right] \tag{6.12}$$

It consists of the concatenated control input matrices convoluted with the discrete state transitions for the respectively appropriate time frames. The control impact $\mathbf{G}_k$ (2.122b) is propagated for one time step T_s with the differential orbit STM

$$\mathbf{A}_k = \mathbf{\Phi}_{DOE}\left(0, dt\right) = \begin{bmatrix} 1 & 0 & 0 & 0 & 0 & 0 \\ 0 & 1 & 0 & 0 & 0 & 0 \\ 0 & 0 & 1 & 0 & 0 & 0 \\ 0 & 0 & 0 & 1 & 0 & 0 \\ 0 & 0 & 0 & 0 & 1 & 0 \\ -\frac{3ndt}{2a} & 0 & 0 & 0 & 0 & 1 \end{bmatrix} \tag{6.13}$$

If the differential semi-major axis vanishes, the DOE STM degrades to an identity matrix. If not, δa has an influence on the relative argument of latitude (lower left matrix element). This STM neglects all perturbing forces on the state vector. It turned out to be sufficient to use these basic dynamics for $\mathbf{A}_{eq}$. For the investigated control input levels in the order of magnitude of $1 \times 10^{-5}\,\mathrm{m\,s^{-2}}$, the influence on the absolute state is so small that the state transition matrix (6.13) is accurate enough. For the matrix $\mathbf{G}_k$, the very same

$\mathbf{A}_k$-matrix was used, giving

$$\mathbf{G}_k = \int_0^{dt} e^{\mathbf{A}_k \tau} d\tau \mathbf{B}(k) \approx \begin{bmatrix} T_s & 0 & 0 & 0 & 0 & 0 \\ 0 & T_s & 0 & 0 & 0 & 0 \\ 0 & 0 & T_s & 0 & 0 & 0 \\ 0 & 0 & 0 & T_s & 0 & 0 \\ 0 & 0 & 0 & 0 & T_s & 0 \\ -\frac{3nT_s}{4a} dt & 0 & 0 & 0 & 0 & T_s \end{bmatrix} \mathbf{B}(k) \tag{6.14}$$

with a zero-order hold assumption on $\mathbf{A}_k$, a total propagation time $dt = t_f - t$ and the GVEs (2.97) for the control influence $\mathbf{B}$. The GVEs are dependent on the instantaneous osculating orbit. The orbit is obtained with the mean orbital elements propagation function $\mathbf{F}$ (5.11), followed by a Brouwer-transformation (2.55) to an osculating element set. The whole process is depicted in diagram 6.14. The control loop starts at the green input variables and terminates in the blue thrust profile if a solution is found by the MPC_f-block, which solves the constrained minimisation problem (6.9). If not, the input is adjusted over and over until the process terminates. The diagram contains two special steps for reconfiguration manoeuvres, which are explained later. The actual model predictive logic is contained in the yellow block MPC_f. This is in fact the process of finding a solution to equation (6.9) under the given constraints and is conducted with MATLAB's linear programming function `linprog`. The yet not mentioned inequality constraint (6.10b) consists in the final implementation of the maximum thrust constraint (2.138) and the rate limit (2.132). The matrix form over the planning horizon for the rate limits is

$$\begin{bmatrix} \mathbf{V} \\ -\mathbf{V} \end{bmatrix} \mathbf{U}_k \leq \begin{pmatrix} \mathbf{R}_k^{\max} \\ \mathbf{R}_k^{\min} \end{pmatrix} \tag{6.15}$$

with

$$\mathbf{V} = \begin{bmatrix} -1 & 0 & 0 & 1 & 0 & \cdots & 0 \\ 0 & -1 & 0 & 0 & 1 & & \vdots \\ \vdots & & \ddots & & & \ddots & \\ 0 & \cdots & & 1 & 0 & 0 & -1 \end{bmatrix} \tag{6.16}$$

$\mathbf{R}_k$ is defined analogue to $\mathbf{U}_k$ in equation (2.131). The both constraints combined to the single inequality

$$\mathbf{L}\mathbf{U} \leq \mathbf{d} \tag{6.17}$$

give

$$\mathbf{L} = \begin{bmatrix} \mathbf{I} \\ -\mathbf{I} \\ \mathbf{V} \\ -\mathbf{V} \end{bmatrix} \tag{6.18}$$
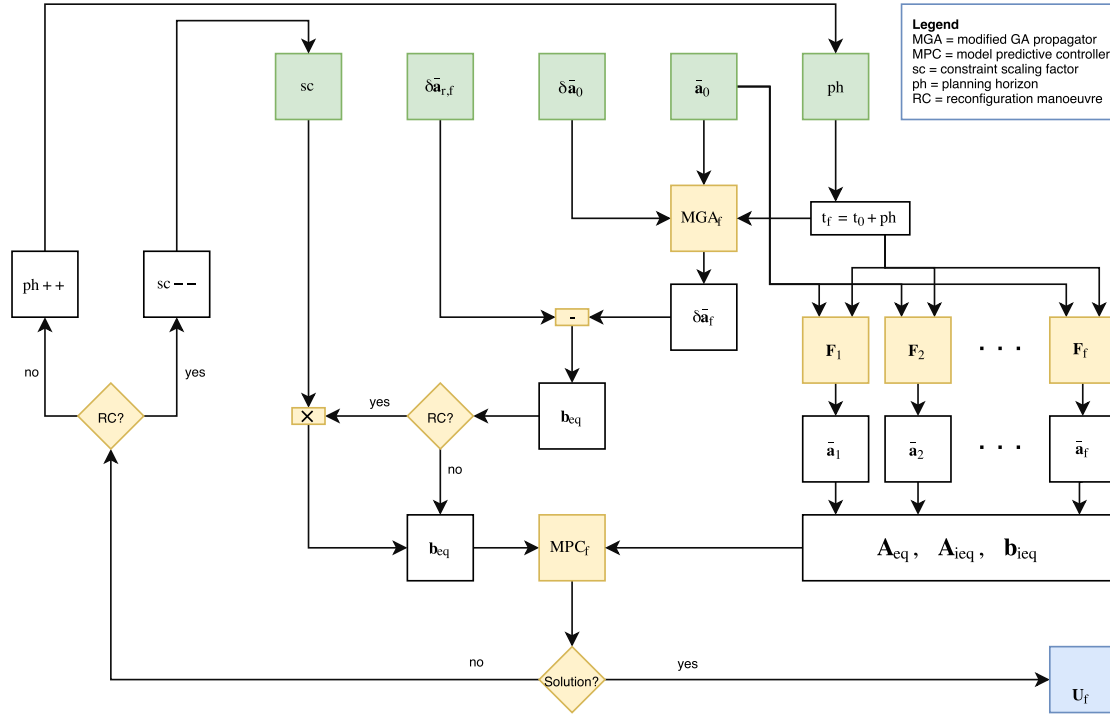
FIGURE 6.14: Diagram of the complete final MPC logic. Input is depicted in green, output in blue.

and

$$\mathbf{d} = \begin{pmatrix} \mathbf{U}_k^{max} \\ \mathbf{U}_k^{min} \\ \mathbf{R}_k^{max} \\ \mathbf{R}_k^{min} \end{pmatrix} \tag{6.19}$$

The MPC inequality (6.10b) uses the extended input vector (2.133) to account for positive and negative input while still posing a minimisation problem. This format is achieved by extending the previously stated matrices appropriately:

$$\mathbf{A}_{ieq} = \begin{bmatrix} \mathbf{L} & -\mathbf{L} \\ -\mathbf{I} & \mathbf{0} \\ \mathbf{0} & \mathbf{I} \end{bmatrix} \tag{6.20a}$$

$$\mathbf{b}_{ieq} = \begin{pmatrix} \mathbf{d} \\ \mathbf{0} \\ \mathbf{0} \end{pmatrix} \tag{6.20b}$$

With this, the minimisation problem formulation (6.9) is complete and can be solved by linear programming techniques.

Since there are no error tolerances or a boundary box included for the final state, the problem is not always feasible. In contrast to the deviation in section 2.4.7 and the relative orbit MPC analysis in Tillerson, Inalhan, and How (2002), this design step was

done on purpose to reduce the total delta-v consumption. When the terminal orbit constraint is not feasible and an adjustable error margin is used, the thrusters will operate at their maximum rates over a large time, which is not desirable. The influence of the control acceleration rises and falls with the sines and cosines of the true anomaly and the argument of latitude (see equation 2.97). In the times in between with low control throughput, delta-v is wasted. Au contraire to the cited source, the developed controller varies the input parameters when it hits an unsolvable minimisation problem. In formation maintenance mode, the planning horizon is increased, giving the spacecraft more time to counteract any state errors. This should only occur after uncontrolled phases in a given configuration (like in a period foreseen for inter-satellite communication). If the problem would not be feasible after a controlled phase (i.e. almost no state error in the beginning), it means that relative perturbation forces are larger than the maximal control output. In this case, also an extended planning horizon dos not lead to feasible solutions, since the perturbation acceleration increases analogous. For formation reconfiguration manoeuvres, a scaling factor for the terminal orbit constraint is used. In one planning period, it is only compensated for a fraction of the difference between desired orbit and current orbit. This is necessary for almost any manoeuvre conducted with CLT, since it takes a very long time for noticeable orbit changes. When no valid thrust profile is found by the MPC, this scaling factor is lowered, reducing the orbit difference to overcome during one planning interval.

For ATF baseline reconfiguration manoeuvres (see section 6.4.3), there may not be any constraint on the differential argument of latitude. To not force a certain value on δu, the terminal orbit equality (6.10a) is extended to:

$$\mathbf{H}\mathbf{A}_{eq}\hat{\mathbf{U}}_k = \mathbf{H}\mathbf{b}_{eq} \tag{6.21}$$

where

$$\mathbf{H} = \begin{bmatrix} 1 & 0 & 0 & 0 & 0 & 0 \\ 0 & 1 & 0 & 0 & 0 & 0 \\ 0 & 0 & 1 & 0 & 0 & 0 \\ 0 & 0 & 0 & 1 & 0 & 0 \\ 0 & 0 & 0 & 0 & 1 & 0 \end{bmatrix} \tag{6.22}$$

This removes the last entry in the terminal orbit constraint, allowing a freely changing differential argument of latitude.

6.4.2 Formation maintenance

The performance of the developed controller is first of all examined at the $5\,\mathrm{km}$ CWF configuration for comparison with the other controllers. Figure 6.15 shows the three-dimensional trajectory of a MPC-controlled satellite over one day. While the uncontrolled trajectory reveals a band (equalling the green trajectory in figure 6.2iii), the controlled one is a sharp line. For this example, the controller was set up with a planning horizon of 60 minutes and a sampling interval of 20 seconds. Figure 6.16i shows the

(I) Uncontrolled
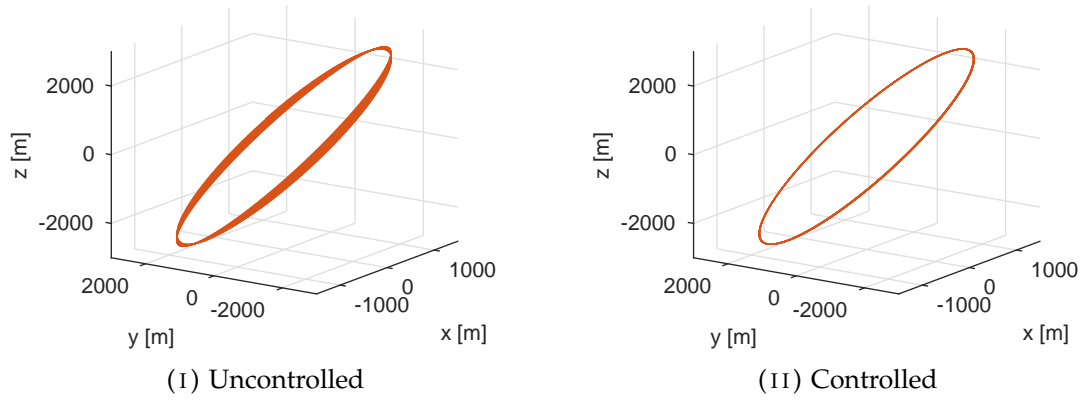
(II) Controlled

FIGURE 6.15: 3D trajectory for one day with MPC ($5\,\mathrm{km}$ CWF).

(I) $5\,\mathrm{km}$ CWF

(II) $2.5\,\mathrm{km}$ CWF
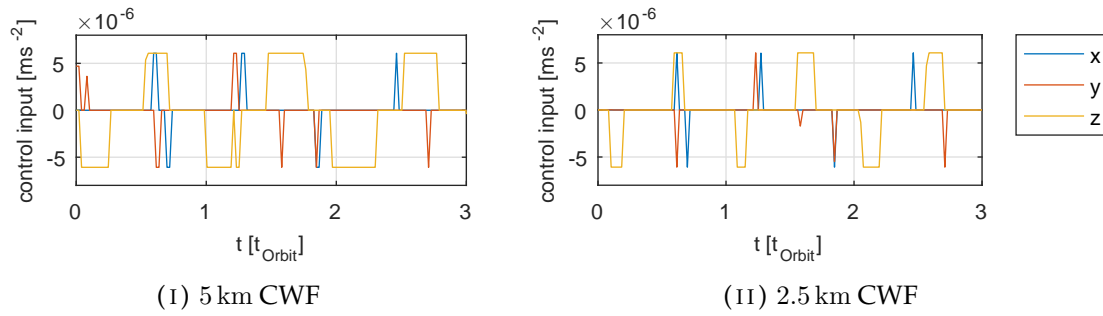
FIGURE 6.16: Thrust profiles with MPC.

generated thrust profile for the first three orbits. This controller, which generates globally optimal solutions over the planning horizon, produces thrust-less time intervals, which can be used for inter-satellite communication. The delta-v consumption per orbit in this configuration is $0.0198\,\mathrm{m\,s^{-1}}$, or around 25% less than the CLF-based controller. Figure 6.16ii shows the applied control input with the same controller configuration for a $2.5\,\mathrm{km}$ CWF. The active thrusting phases are around half as long as for the CWF with a doubled baseline. This suggests that there is a linear relationship between thrusting time and total delta-v to formation baseline. The more attitude-constraining activities besides orbit control are planned, the smaller the formation baseline has to be. Furthermore, the left thrust profile implicates that the baseline may not grow much larger for CWF, since thrusting in z-direction is for a large fraction at its maximum level.

The MPC-controlled ROE state vector is shown in figure 6.17. In contrast to the LQR controller, the MPC controls only in certain intervals, leading to a more discrete shape. The absolute error values in the ROE vector are around as high as the ones of the LQR controller. This implicates that the developed MPC is superior in terms of delta-v consumption while at the same time maintaining the lowest position deviation (below $3\,\mathrm{m}$ in Hill-frame for the example configuration).

The two most important design parameters of the MPC algorithm are the planning horizon and the control interval. The planning horizon is the amount of time over which
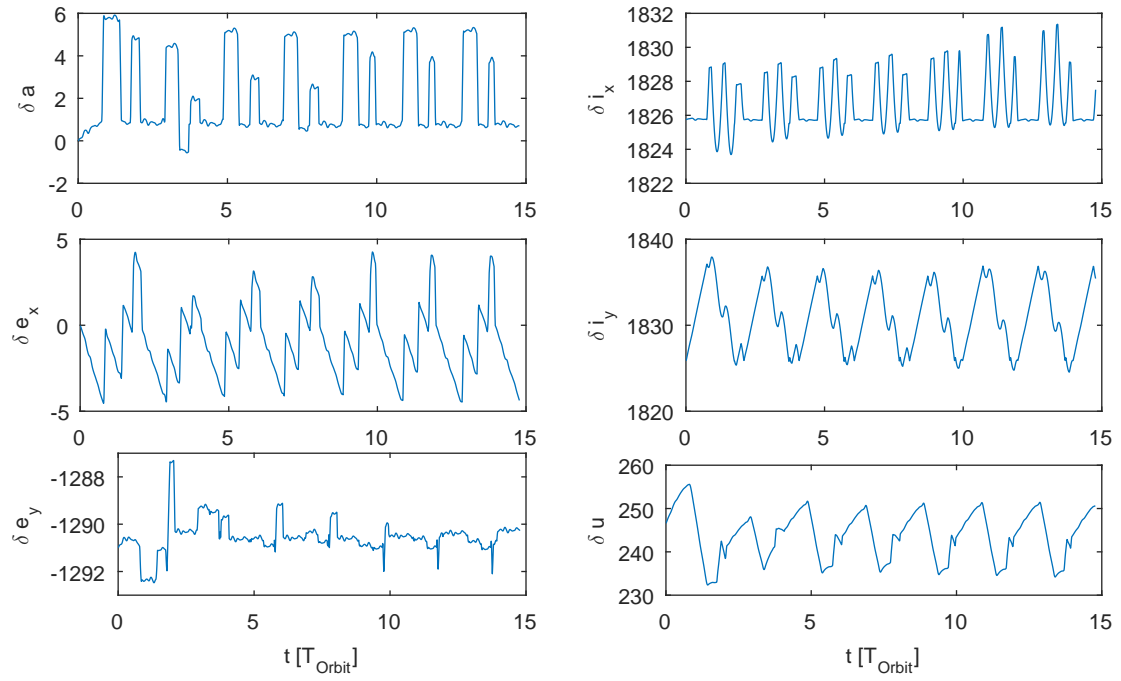
FIGURE 6.17: ROE for one day with MPC (5 km CWF).

FIGURE 6.18: Position deviation over planning horizon (5 km CWF).
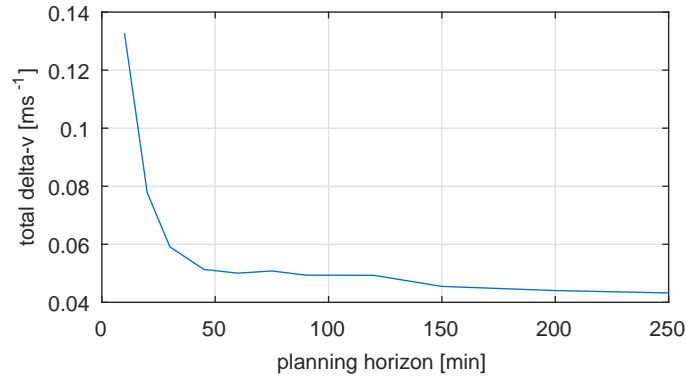
F I G U R E 6.19: Per-orbit delta-v over MPC planning horizon (5 km CWF).

MPC optimises the thrust profile. Since MPC generates globally optimal solutions over the horizon, an extended horizon should lower the long-term delta-v consumption. In the implementation described in section 6.4.1, the orbit is only enforced at the end of the planning horizon, leading to larger position errors in between when the horizon is extended as can be seen in figure 6.18. It shows the maximal position deviation 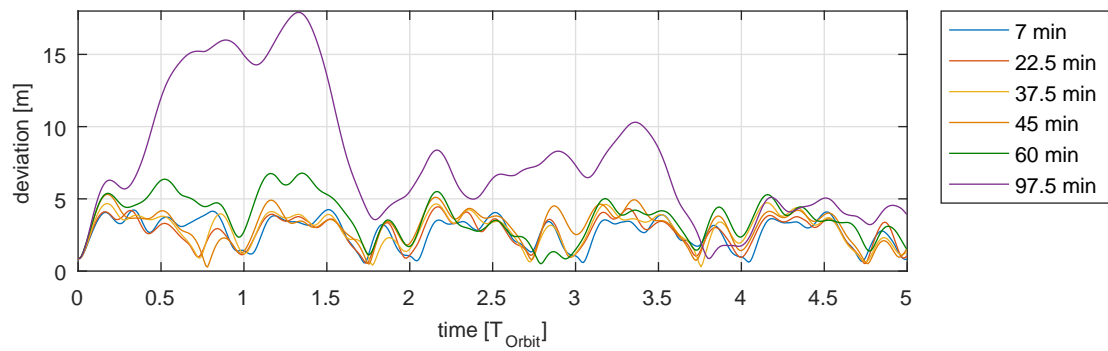from the reference governor for different planning horizons between 7 and 97.5 minutes, where the latter corresponds to one orbital period. Below 60 minutes, the deviation does not fall significantly for shorter intervals. The five-meter-level in between full orbital periods, which is shared by all intervals below 60 minutes, is a result from the deviation of the relative orbit propagator $\mathbf{\Phi}_{MGA}\left(\delta\bar{\mathbf{a}}_0, t_f\right)$, which receives a position update only once per orbit (see section 5.5). In other words, there is no need to lower the planning horizon below 60 minutes in terms of orbit deviation, since it does not lead to a gain in accuracy.

As stated before, the planning horizon also influences the total delta-v consumption, which is depicted in figure 6.19. The longer the horizon, the more optimal the solution becomes. Below half an orbital period (around 50 minutes), the per-orbit delta-v rate rises rapidly. The very small high-frequency position oscillations are counteracted, which consumes a lot of delta-v. For longer planning horizons, these oscillations are smoothed out and delta-v is saved. The figure also reveals that there is only a very small gain in optimality for much longer horizons. Combining the result of the two observations in terms of position deviation and delta-v consumption, a planning interval of around half the orbital period – 50 minutes – seems to be the best choice. This choice also allows a per-orbit long-term planning between maintenance and reconfiguration manoeuvres, since the end of one Keplerian period always coincides with the end of a planning horizon. Furthermore, the relative orbit propagator is updated once per orbit, giving an error reset right before every second MPC planning interval, which results in the highest possible accuracy.

The MPC performance also depends on the interval at which new thrust profiles are generated (see beginning of section 2.4.7). If this interval is shorter than the planning
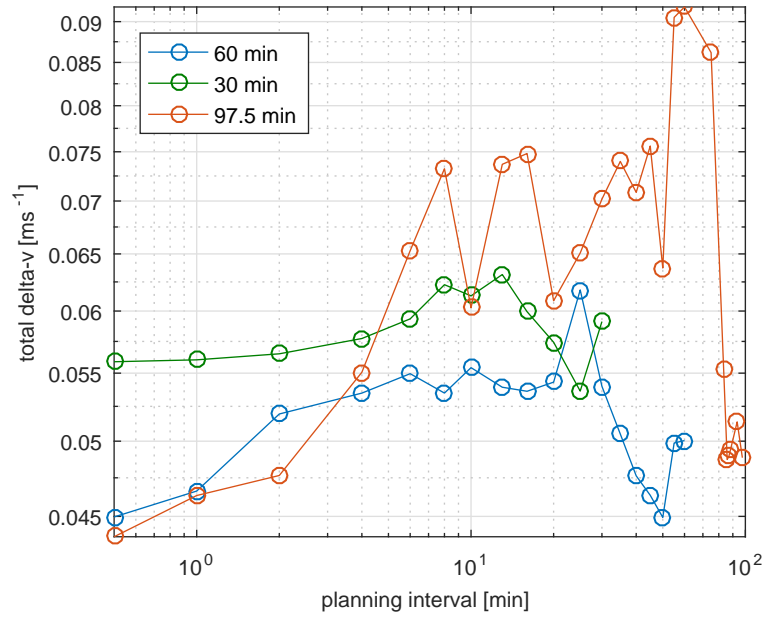
FIGURE 6.20: Per orbit delta-v over MPC control interval for different planning horizons (5 km CWF).
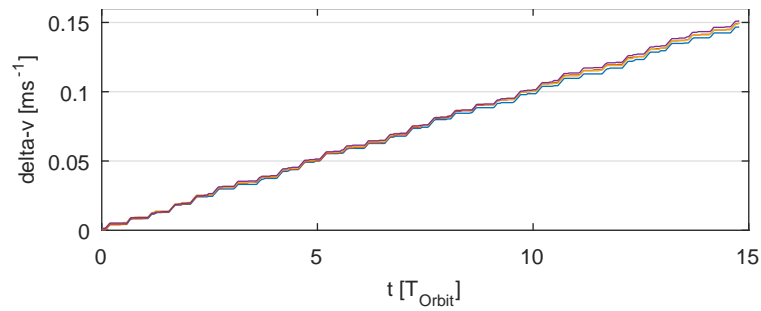
FIGURE 6.21: Delta-v consumption of four satellites in a 2.5 km CWF configuration (one line per satellite, almost equal profiles).

horizon, the last part of the generated thrust profile is dismissed and replaced with the beginning of the newly generated profile. The influence of the control interval on delta-v consumption is shown in figure 6.20 for the three planning horizons 30, 60 and 97.5 minutes. Each line ends at a planning interval which coincides with the planning horizon. If the control interval is larger, there would be uncontrolled times in between the end of the planning horizon and a new control interval. Although the data points seem to be arbitrarily distributed on first sight, one can draw a rough conclusion from the figure. All three curves have in common that they reveal the lowest delta-v consumption for a very short control interval (from seconds up to a few minutes) and for a control interval equal to the planning horizon. Since it seems unlikely that the on-board computer can solve the linear programme at a high frequency, the planning intervals below one minute are dismissed. This leads to the conclusion that the optimal choice for the control interval is the length of the planning horizon.

(I) $\gamma_0 = 0°$ (II) $\gamma_0 = 45°$
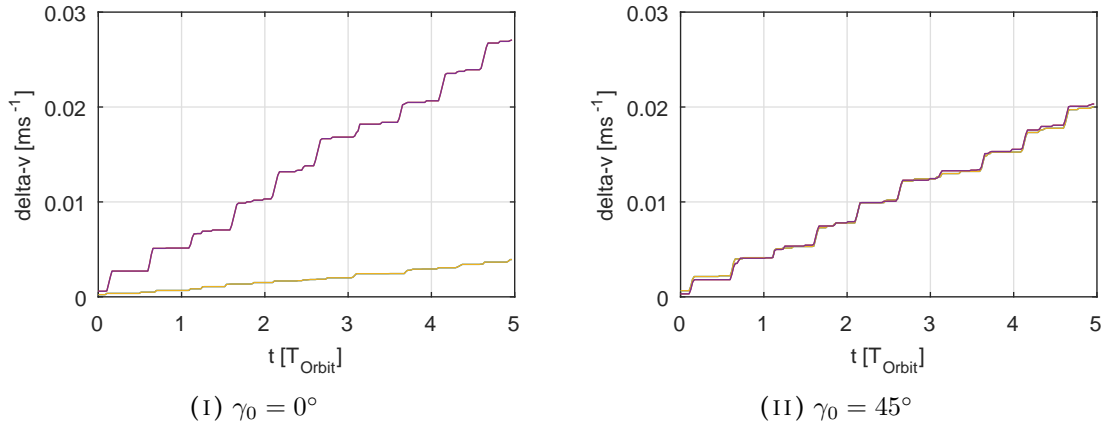
FIGURE 6.22: Delta-v consumption of four satellites in a $1\,\mathrm{km}$ PCO configuration (one line per satellite, some profiles are almost equal).
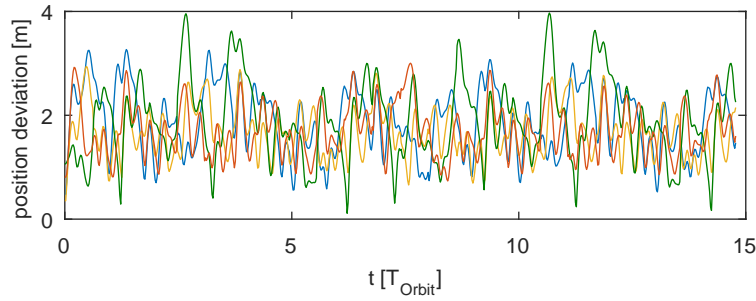
FIGURE 6.23: Position deviations of four satellites in a $2.5\,\mathrm{km}$ CWF configuration for one day with $t_f = T_O$.

An important aspect of formation control is the equal distribution of control effort over the whole fleet. Figure 6.21 shows the delta-v consumption of four satellites in CWF configuration over one day. The expenditure is almost equally distributed among all spacecraft, no matter how the angular design parameter γ_0 in the CWF definition (3.3) is chosen, since it does not influence the $\delta\mathbf{i}$-vector. For PCO configurations, however, the angular design parameter influences the control effort distribution, which is shown in figure 6.22. If γ_0 is set to zero in the PCO definition (3.2), two satellites do not have a δi_x component and two do not have a δi_y component in their ROE vectors. Following the ROE definition (2.32), δi_x depends on the relative inclination and δi_y on the relative right ascension of the ascending node. Since only $\delta\Omega$ of the two is subject to J_2-drift (see equation 2.65), δi_y costs a lot more delta-v to maintain. Shifting the design parameter γ_0 by $45°$ adjusts the magnitudes of all satellites' δi_x- and δi_y-values to the same level, leading to an equal control effort to maintain the projected circular orbit. To guarantee a homogeneous delta-v consumption on the long run (see figure 6.22ii), each PCO state vector set must be designed with the just mentioned restriction on the angular design parameter.

The long-term stability of the controller is shown in figures 6.23 and 6.24 for $2.5\,\mathrm{km}$ CWF and $500\,\mathrm{m}$ PCO, respectively. For both figures, the planning horizon was set up to the orbital period of the satellites. Even with this value double as high as the nominal horizon
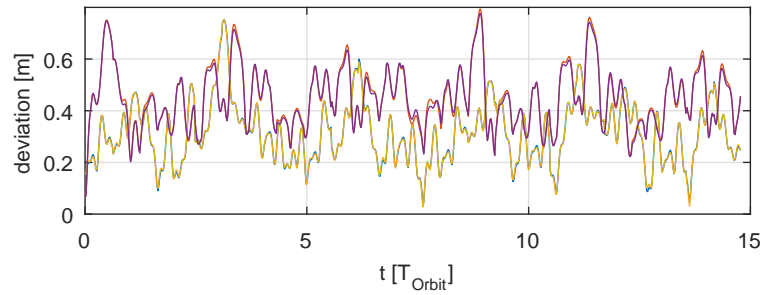
FIGURE 6.24: Position deviations of four satellites in a $500\,\mathrm{m}$ PCO configuration for one day with $t_f = T_O$.

(I) PCO   (II) CWF
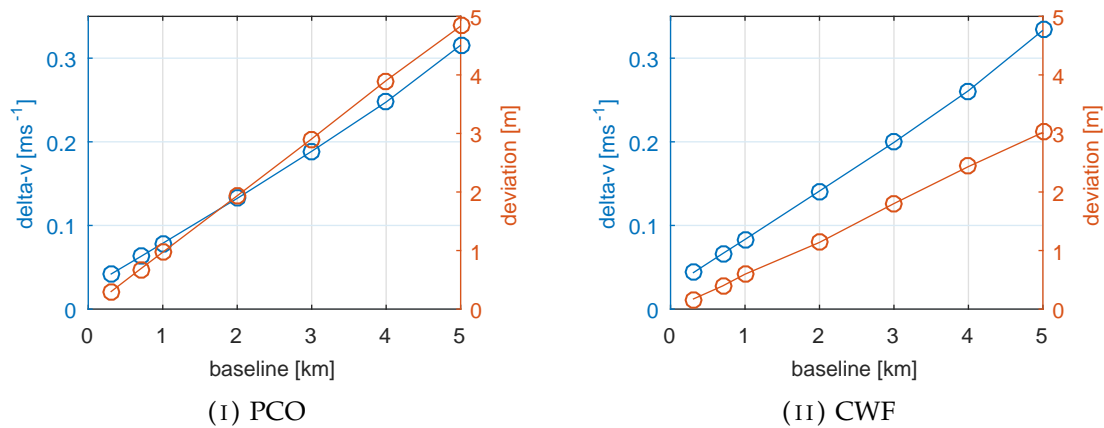
FIGURE 6.25: Daily delta-v consumption and maximum position deviation for different baselines of PCO and CWF configurations.

interval, the error roughly stays within the bounds of the first orbit, no matter if a CWF or PCO configuration is chosen. This lets assume that MPC provides satisfying stability, even if for some reason planning- or inter-satellte-update-intervals are extended above their nominal values.

Figure 6.25i shows the daily delta-v consumption and maximum position deviation in relation to the formation baseline for the nominal control interval and planning horizon. The same data for CWF configurations is depicted in figure 6.25ii. To a high degree, both reveal a linear relationship between baseline and delta-v consumption as well as position deviation for the examined baseline extents. The $5\,\mathrm{km}$ baseline is the upper limit for both configurations with the given maximum capabilities of the on-board thrusters. For baselines above $8\,\mathrm{km}$, the differential perturbation force is higher than the maximum control force. A margin of three kilometres was chosen to not operate at the maximum thrust level all the time. This would not allow any other activity than continuous orbit control. Furthermore, the power system will not allow permanent thrusting throughout a whole orbit. The margin is based on the so far available very rough definition of the power system and may be adjusted in the future when the power model is well defined. The high control accuracy for close formations gives rise to the possibility to fly baselines below $1000\,\mathrm{m}$, if intended. Figure 6.26 shows the position deviation and delta-v consumption for along track configurations on a log-log scale. Since ATF will be used
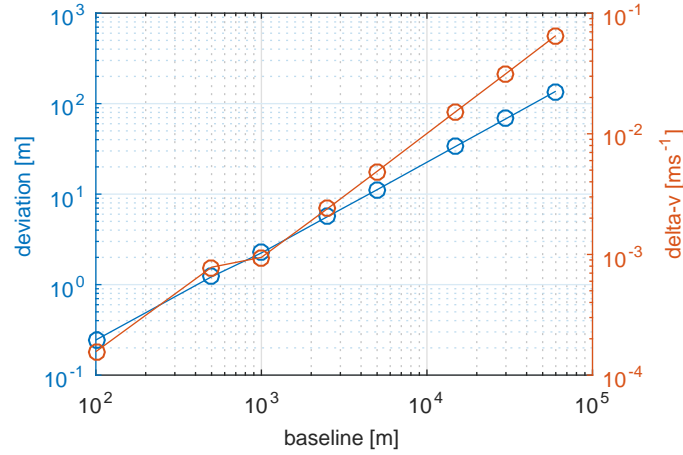
FIGURE 6.26: Hill-frame position deviation and total delta-v for five
orbits for different ATF baselines.
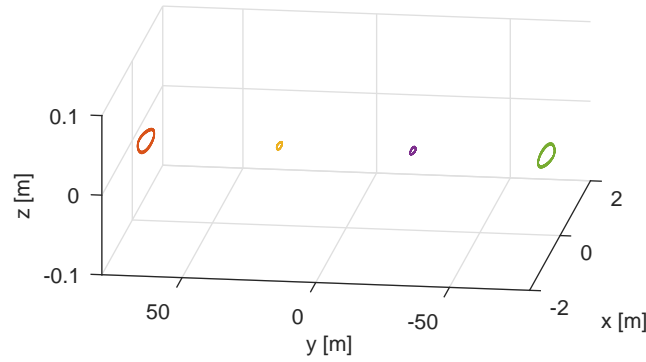
FIGURE 6.27: Trajectories over one day for a $150\,\mathrm{m}$ ATF configuration.

on a much larger scale, also formations up to $100\,\mathrm{km}$ baseline have to be examined. They
are only distinguished by the relative argument of latitude, while all $\delta\mathbf{e}$- and $\delta\mathbf{i}$-vectors
are zero. The larger the ATF configuration is, the larger the linearisation error of the
Hill-frame gets (see figure 3.1i). For that, the delta-v consumption also increases linearly
with the baseline. To counteract a high control effort for very large ATF configurations,
the formation centre (virtual chief) can be shifted individually towards each spacecraft.
The sub-meter accuracy of ATF control is shown in figure 6.27 for a $150\,\mathrm{m}$ baseline. The
nominal distance between any two neighbouring satellites is $50\,\mathrm{m}$. Throughout the day,
all inter-satellite distances stay in the interval $[49.6\,\mathrm{m}; 50.4\,\mathrm{m}]$. The observations for all
formation types in terms of delta-v are pooled in the following equation set, where $f_\oslash$
gives the daily control effort in $\mathrm{m\,s^{-1}}$ per satellite for maintaining a formation of type $\oslash$
with baseline $x[\mathrm{km}]$ (as defined in chapter 3).

$$f_{PCO}\left(x\right) = 0.058x + 0.021 \tag{6.23a}$$

$$f_{CWF}\left(x\right) = 0.061x + 0.022 \tag{6.23b}$$

$$f_{ATF}\left(x\right) = 0.0033x \tag{6.23c}$$

(I) Total delta-v consumption.

(II) Change in argument of latitude.
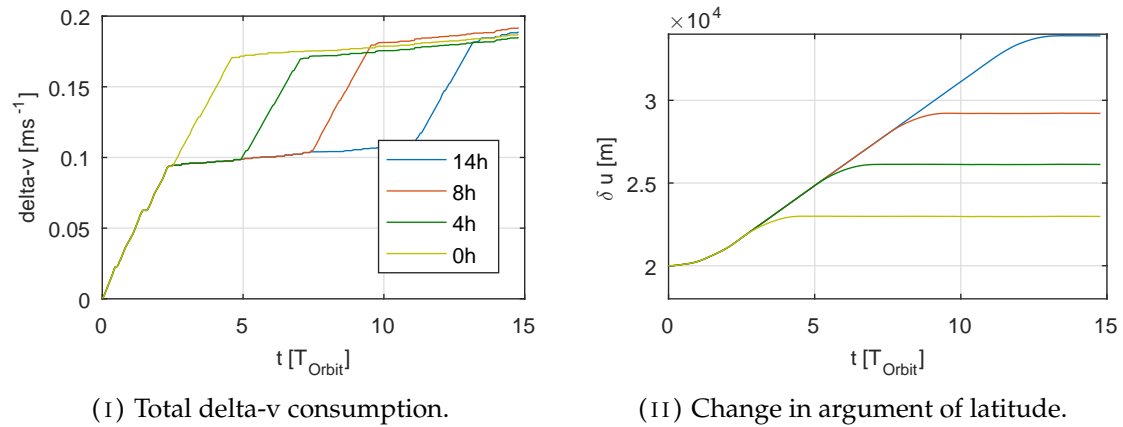
FIGURE 6.28: Impact of the cruising phase in ATF baseline reconfigurations for $\delta a = 135\,\mathrm{m}$.

6.4.3 Reconfiguration manoeuvres

The simplest reconfiguration manoeuvre is the variation of an ATF baseline. Since all satellites share the same orbit without relative inclination or eccentricity, the distance between the satellites can be altered by adding a relative semi-major axis. If a satellite is in a smaller orbit ($\delta a < 0$), it has a shorter Keplerian period and shortens the distance to another satellite flying ahead. This kind of reconfiguration is divided into three manoeuvres. In the first phase, the satellite creates a positive or negative relative semi-major axis by thrusting in y-direction. This is done with the CLF-based δa-controller described in section 6.2, since it is the most effective way to generate an offset in a. In the cruising phase, the satellite maintains the ROE state vector, including the relative semi-major axis. To allow a change in relative argument of latitude, while at the same time maintaining the other state vector elements, MPC with the extended terminal orbit constraint (6.21) is used. When the desired distance is reached, the satellite begins the last phase, in which the difference in semi-major axis is cancelled out with the CLF-based δa-controller. In this time, the satellite will further increase (or decrease) the relative argument of latitude until δa is zero. This has to be obeyed when designing a manoeuvre to reach a certain inter-satellite distance. The delta-v consumption for such a reconfiguration highly depends on the chosen offset in δa, while the baseline change depends on the cruising time. Figure 6.28 shows the delta-v consumption and the change in δu for four different cruising periods. In the case of the yellowish green curve, phase two was omitted in the manoeuvre. All four manoeuvres have a positive δa-offset of $135\,\mathrm{m}$, which increases δu over time. This choice of δa is a fair compromise between delta-v consumption for entering (and leaving) the drift orbit and alteration speed of δu. The two parameters have a linear relationship, allowing a simple adjustment of the time of the reconfiguration manoeuvre, if desired. Figure 6.28i reveals that there is almost no influence of the cruising period on total delta-v consumption – the MPC controller needs the same amount of control input to hold a certain ATF configuration, no matter of the current δa. With this in mind, arbitrary large changes in δu may be achieved with almost the same amount of delta-v consumption. For the given parameter set, a change in δu of

(I) $c = 0.1$ (II) $c = 0.03$
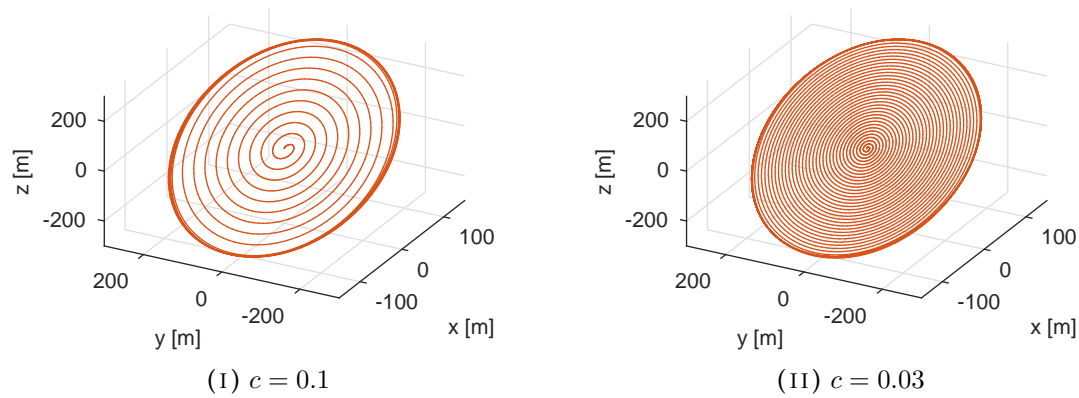
FIGURE 6.29: Transfer trajectory from Hill-frame origin to $500\,\mathrm{m}$ PCO
configuration.

(I) $c = 0.1$ (II) $c = 0.03$
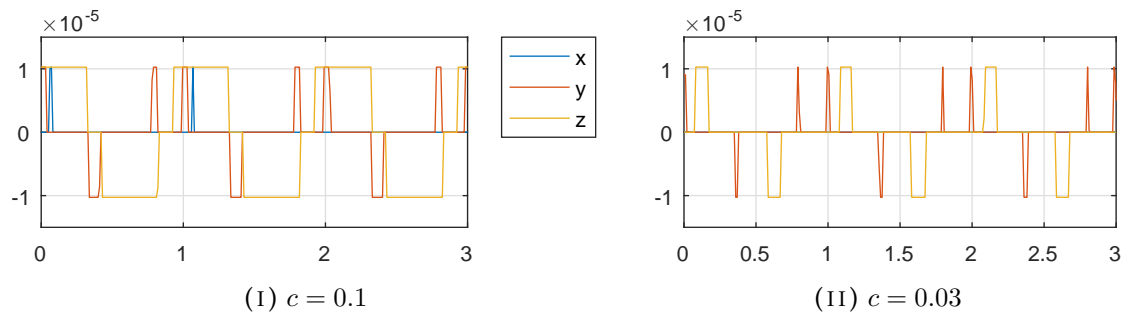
FIGURE 6.30: Thrust profile from Hill-frame origin to $500\,\mathrm{m}$ PCO con-
figuration.

$15\,\mathrm{km}$ is reached within one day, including the δa-correction phases. The delta-v amount needed for the ATF reconfiguration does not change for larger δu-offset manoeuvres or manoeuvres at larger baselines. Also, delta-v does not change with the direction of the alteration, i.e. an increase or a decrease of δu. Only the delta-v needed to keep the cruising orbit has to be added according to equation (6.23c), but this resembles the minor amount of the whole reconfiguration. In terms of the MPC logic diagram 6.14, the cruising phase is viewed as a formation maintenance period (not as reconfiguration phase, but with the extended terminal orbit constraint).

Reconfiguration manoeuvres for PCO and CWF formations demand more time, since the relative eccentricity- and inclination-vectors have to be changed. Figure 6.29 shows the transfer of one satellite from the origin of the Hill-frame to a $500\,\mathrm{m}$ PCO orbit for different reconfiguration scaling factors. The factor c is the fraction of the difference to the target orbit which is conquered in one orbital period. The manoeuvre in figure 6.29i with a factor of $c = 0.1$ is accomplished after ten orbits, expressing itself in ten torsions of the spiral until the target orbit is reached. When a factor of $c = 0.03$ is used, 33 orbits are needed to reach the final configuration.

(I) total delta-v   (II) total time
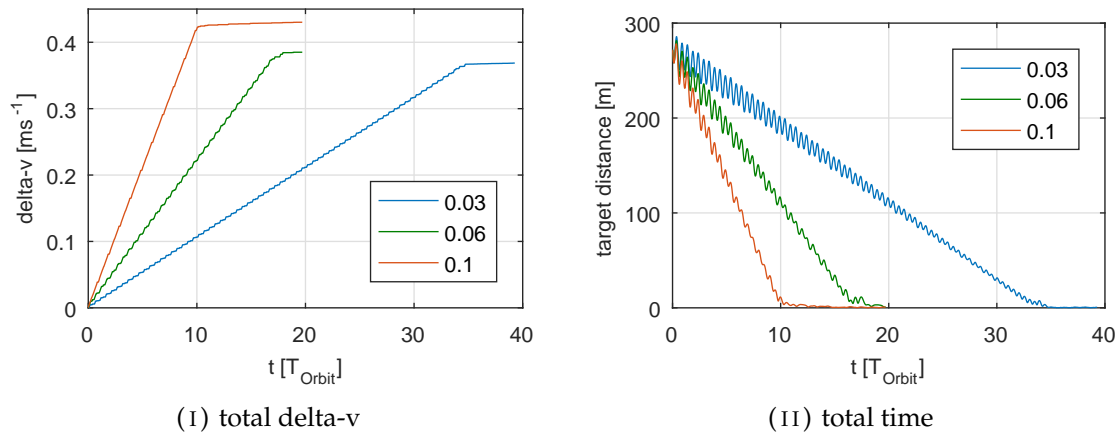
FIGURE 6.31: Influence of the *c*-factor on PCO reconfigurations.

The trajectory depicted in figure 6.29i is the fastest way for the given thrusting limits to achieve the target orbit. When c is further increased, the MPC does not find a solution to meet the terminal orbit constraint and the scaling factor is decreased before a new attempt is started (see algorithm overview in figure 6.14). For the first three orbits, the thrust profiles for the two manoeuvres of figure 6.29 are depicted in figure 6.30. The first profile for $c = 0.1$ shows continuous firing in z-direction, which is impossible with regard to the power system (see preceding section). A scaling factor of $c = 0.03$ gives well-defined intervals with and without thrust throughout the whole manoeuvre. The peaks in z-direction in figure 6.30ii coincide with the maxima of the sine of the true argument of latitude θ, which is the optimal time in orbit to alter the relative ascending node. As the peaks are pretty narrow, delta-v consumption will not get significantly lower for even smaller scaling factors. Figure 6.31i shows the total delta-v consumption for the $0 - 500\,\mathrm{m}$ PCO reconfiguration for the two scaling factors mentioned before and for an intermediate value $c = 0.06$. For the intermediate factor, the amount of delta-v is only slightly higher than for $c = 0.03$. The curve resembles the optimal choice between transfer time and delta-v consumption. For $c > 0.06$, the latter rises rapidly. The relation between c and the total time needed for the transfer is emphasised in figure 6.31ii. As expected, the time needed to reach the target orbit is $1/c\ T_O$.

Roughly the same numbers can be observed for CWF reconfigurations. Figure 6.32 shows the trajectory of a $1500 - 2500\,\mathrm{m}$ CWF manoeuvre for $c = 0.03$. For both, CWF and PCO reconfigurations, the transfer direction does not have an influence on delta-v. This means, the delta-v consumption of the stated manoeuvre is as high as a manoeuvre from $2500\,\mathrm{m}$ baseline down to $1500\,\mathrm{m}$. Furthermore, to the extent of the possible baselines up to $5\,\mathrm{km}$, delta-v is linearly related to baseline change. So the two manoeuvres are as costly as the initial CWF advance from the Hill-frame origin to $1000\,\mathrm{m}$ baseline. Combining all results, a scaling factor of $c = {}^{30\,\mathrm{m}}\!/\Delta b$ (where $\Delta b[m]$ is the difference in baseline) seems to be the optimal choice for all transfers. In other words, the satellite will change its PCO or CWF baseline by $30\,\mathrm{m}$ per Keplerian period during reconfiguration manoeuvres, giving a total time of almost 2.4 days per kilometre. For the two formation types, the following equations give the total amount of delta-v needed for the
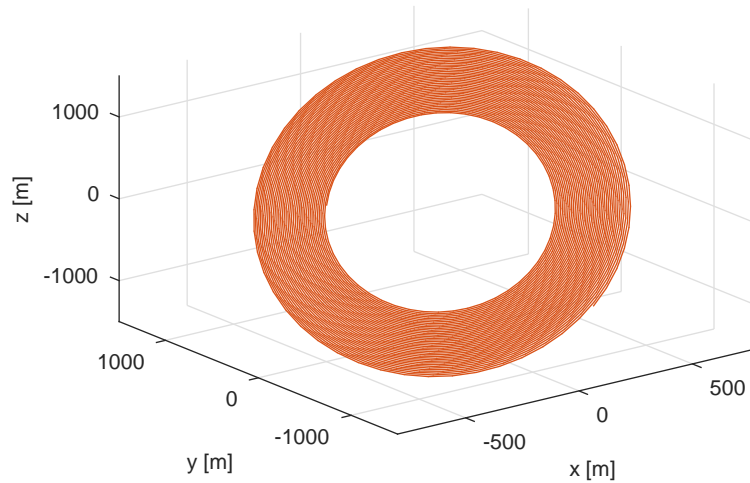
FIGURE 6.32: Transfer trajectory from $1500\,\mathrm{m}$ to $2500\,\mathrm{m}$ CWF configuration.

(I) View 1

(II) View 2

FIGURE 6.33: Trajectories of three satellites in initial CWF orbit and one satellite approaching the formation centre (depicted in red).

reconfiguration:

$$r_{PCO}\left(x\right) = 0.90x \tag{6.24a}$$

$$r_{CWF}\left(x\right) = 0.75x \tag{6.24b}$$

where x is the total baseline change in kilometres.

A baseline extension manoeuvre (like the one in figure 6.32) can be done simultaneously by all satellites of the formation without a loss of inter-satellite minimum distance. In contrast, the initial PCO manoeuvre depicted in figure 6.29 cannot be done by multiple satellites at the same time, since all would start at the same position (also true for initial CWF manoeuvre). This can be overcome by starting from an ATF configuration in both cases. To achieve the initial CWF formation, one satellite is brought to the centre of the Hill-frame and starts its initial spiral to target a $700\,\mathrm{m}$ CWF orbit. During this time, the other three satellites stay well beyond the target spiral at around $1500\,\mathrm{m}$ distance from
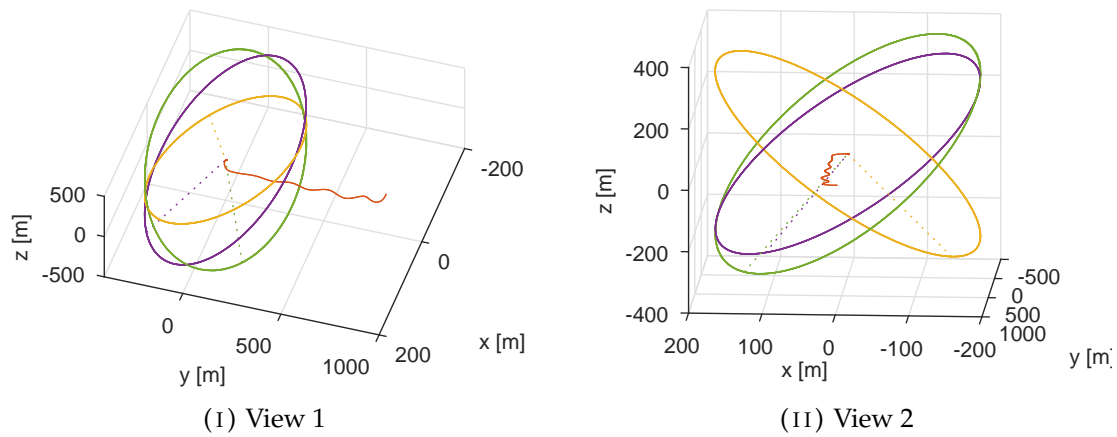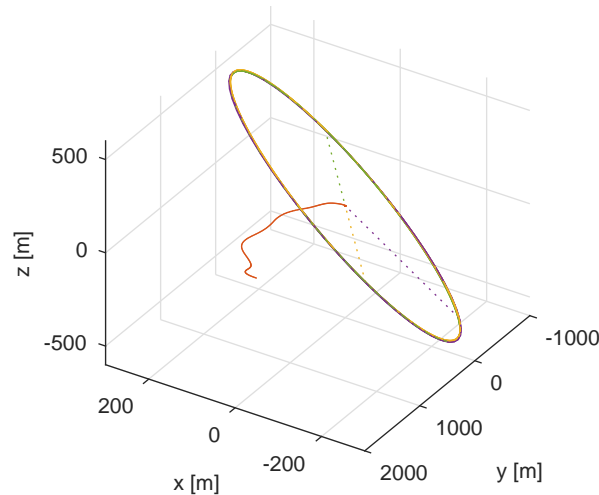
FIGURE 6.34: Trajectories of three satellites in initial PCO orbit and one
satellite approaching the formation centre (depicted in red).

the formation centre. Once the first satellite reached his target, the second spacecraft is brought to the Hill-frame origin, what is done with a slight change in δa. As can be seen in figure 3.4ii of the CWF formation's definition, no satellite which is already in an CWF orbit comes into the vicinity of the y-axis of the Hill-frame. Once at the origin, this satellite also approaches the initial CWF orbit with $700\,\mathrm{m}$ baseline. This procedure is repeated until all four satellites are equally spaced in the initial CWF ellipse. The centre-approach trajectory of the fourth satellite, when the other three are already in a CWF orbit, is shown in figure 6.33 for two different angles. The fourth satellite (red trajectory) started at an initial ATF position $813\,\mathrm{m}$ away from the formation centre and maintained a drift orbit with $\delta a = 20\,\mathrm{m}$ for six hours. The nominal closest distance between any two satellites for the $700\,\mathrm{m}$ CWF configuration is $380\,\mathrm{m}$, which never goes below $378.5\,\mathrm{m}$ with MPC control. During the centre-approach of the last satellite, the nominal distance goes down to $121\,\mathrm{m}$ for a short time, when the satellite passes the sphere made up by the ellipses. The true inter-satellite distance from the realistic simulation never went below $120.5\,\mathrm{m}$ during the manoeuvre. Even though the minimum nominal distance of the manoeuvre may sound restrictive, the simulation asserts its possibility. During the total time of seven hours, the centre-approaching satellite consumed $0.023\,\mathrm{m\,s^{-1}}$ delta-v mainly for δa-correction. The other three satellites consumed $0.019\,\mathrm{m\,s^{-1}}$ delta-v for formation maintenance control (see equation 6.23b). To go from a CWF formation back to an ATF configuration, the whole process is done in reverse order.

The process of initial formation approach for PCO configurations is different, since a PCO orbit directly cuts the y-axis (see figure 3.2). With the technique for initial CWF approach, the satellites would only have a minimum distance of $20\,\mathrm{m}$, resembling the δa-term in the drift orbit. The minimum distance can be increased by a larger δa-value for the centre-approach and a larger baseline of the initial PCO orbit. Since δu changes rapidly with increasing differential semi-major axis, no drift orbit is needed. As soon as the fourth satellite reaches its nominal δa-value, which is set to $\delta a = 90\,\mathrm{m}$, it is corrected

back to zero. The approach trajectory and the trajectories of the other satellites already in the initial PCO orbit with a baseline of $1000\,\mathrm{m}$ are depicted in 6.34. The fourth satellite (red trajectory) starts in an ATF orbit with $\delta u = 1596\,\mathrm{m}$ and reaches the origin of the Hill-frame after 2.5 orbits. The nominal minimal distance at the PCO-ellipse crossing is $122\,\mathrm{m}$ for the given manoeuvre parameters and did not fall below $121\,\mathrm{m}$ during the simulation. The approaching satellite consumes the high amount of $0.12\,\mathrm{m\,s^{-1}}$ delta-v as a consequence of the large δa-offset. During this short period of only 2.5 orbits, the other three satellites only consumed $0.008\,\mathrm{m\,s^{-1}}$ delta-v. The last three satellites (all except the first one) need to do this costly origin-approach manoeuvre. When going back to an ATF configuration, the order at which the satellites leave the formation should be reverted in order to promote fuel balancing.

Chapter 7

Conclusion

This chapter summarises the results obtained in this work. Special focus is directed to the outcomes' implications on the *NetSat* mission, with regard on satellite design parameters and flyable formations. A complete mission plan comprising a time frame of five months is presented, accommodating four phases with different types of formations. In the end, suggestions on further work are presented.

7.1   Results and mission plan proposal

A comprehensive software framework has been developed, which enables accurate orbit simulations for satellite formations (see section 4.3). It uses an extensible satellite model, where more subsystems can easily be added in the future and already implemented coarse subsystem definitions may be substituted with more exact high-level counterparts (see section 4.2). The framework, which is fully configurable through csv-based databases, features multiple relative orbit propagators and controllers with different levels of accuracy. The final on-board propagator has sub-meter accuracy for formation baselines below $1\,\mathrm{km}$ and in general deviations lower than 0.1% of the formation baseline. The relative propagation error rises very slowly with time. In nominal operation, a communication interval of one orbital period ensures exact relative navigation among the fleet. Even for close formations, multiple consecutive orbits without inter-satellite communication do not expose a risk to the formation – the propagator error does not rise above 5% of shortest inter-satellite distance over one day. Depending on to-be-defined design parameters of other subsystems, the communication period could even be extended to multiple orbital periods at the expense of slightly increasing the shortest possible baseline (see section 5.5). Multiple control techniques were implemented, where a combination of two was used in the end, namely CLF-based δa-control and MPC. The CLF-based δa-controller is used for along-track reconfiguration, i.e. shifting the along-track inter-satellite distance (see section 6.2). Three types of the MPC controller are used for different tasks. A MPC maintenance controller is used for formation hold control for all three analysed configurations (ATF, PCO, CWF). The maintenance controller enforces all six differential orbital elements on the satellite, resulting in full-state control (see section 6.4.2). When the desired state vector at the planning horizon cannot be reached due to uncontrolled phases before, the planning horizon is shifted

to the future until a solution is found. The MPC reconfiguration controller is used to generate trajectories between different baselines of PCO and CWF formations as well as the initial PCO- and CWF-establishing phases starting from an ATF configuration. The MPC reconfiguration controller, which also provides full-state control, divides the distance from the current to the final differential orbit into multiple sections, conquering one at a time in each planning interval (see section 6.4.3). If a section target cannot be reached, the differential orbit to overcome in one section is lowered. By this technique, both MPC controllers will eventually find a solution for every desired target formation as long as terminal orbit constraints are reasonable with regard to the thrust system. The third MPC type is used for the cruising phase of ATF baseline reconfigurations. It resembles the first MPC type except that it does not control the relative argument of latitude. This enables the satellite to drift towards (or away from) another satellite until the desired separation is reached. It was shown that the control error is below 0.5% of the baseline for all analysed formation types and distances. This result, in combination with the relative propagator accuracy, stands in contrast to the initially stated GNC scaling law (see table 1.1) and allows closer formations as expected. With the proposed nominal communication interval of one orbital period, $1000\,\text{m}$ PCO and $700\,\text{m}$ CWF formations may safely be flown. For these baselines, the nominal minimal inter-satellite distance is above $380\,\text{m}$, while the real positions deviate only by $1.5\,\text{m}$. For ATF configurations, even a baseline of $150\,\text{m}$ – with nominal distances of $50\,\text{m}$ between the satellites – seems possible. For this configuration, the satellites' positions deviate by only $0.5\,\text{m}$. All manoeuvre simulations were executed under the given constraints for the power- and thrust-system (see section 1.2). A direct consequence of the upper thrust limit is the maximum baseline for PCO and CWF formations which can be flown – $5\,\text{km}$. Above this value, the relative perturbation forces are too high to be mitigated with the thruster capability under the given maximum duty cycle. As soon as the power system is well defined, the upper bound for the two formations may be adjusted. All in all, the work on relative orbit propagation and control showed that one-, two- and three-dimensional configurations are possible within the given constraints.

Based on these results, a complete mission plan for *NetSat* is proposed. The detailed plan is given in table 7.1. The plan comprises five months and is divided into four phases. Every single action has been simulated with the developed software framework and the delta-v consumptions of all satellites are given. The first phase (around one month) is foreseen for initial configuration acquisition. After an uncontrolled LEOP phase of two weeks (following results from preceding UWE missions, see section 3.1), the satellites are brought to the initial $100\,\text{km}$ ATF configuration within one week. For this phase, the needed delta-v estimates are very coarse and an amply margin was added to the time as well as the delta-v budget calculation. Accurate numbers for this part of the missions are impossible to calculate, since the initial state vectors after deployment of the four satellites may only be estimated. The initial acquisition phase consists of a mitigation of the differential semi-major axis to prevent further drift. After this, the relative eccentricity and inclination between the satellites is abandoned. Once a nominal ATF orbit is reached, the baseline is reduced to $100\,\text{km}$. Each satellite is supposed to consume

roughly the same amount of delta-v, since a distinction renders useless with the given accuracy of the initial state vector.

The second phase comprises different ATF baselines between $100\,\text{km}$ and $5\,\text{km}$ (see section 3.2). It also takes roughly one month with generous time intervals at certain baselines. This gives the possibility to react to unforeseen events or conduct extensive on-orbit testing without altering the overall mission plan. Although the satellites have to overcome different distances to fit in the closer formations, all are again supposed to consume the same amount of fuel. The inter-satellite distance change is not linearly related to delta-v, but to the time frame of the cruising orbit (see figure 6.28). The highest delta-v amount of the simulation with four satellites was increased by an error margin of 10% and used for all satellites in delta-v budgeting. This accounts for linearisation errors and uncertainties related to the very large separation in the beginning of the phase.

In the beginning of the third phase, the two-dimensional PCO configuration is established (see section 3.3). From the start of this phase, which lasts two months, all delta-v expenditures are given accurately for each individual spacecraft. As investigated in section 6.4.3, the initial PCO acquisition has to be done one by one. Starting with the first satellite, the whole formation successively targets a $1000\,\text{m}$ PCO orbit. During this time, the satellites which already reached the PCO orbit consume more delta-v as the ones still waiting in close ATF configuration. During this phase, the minimal inter-satellite distance drops to $120\,\text{m}$ for a very short time during each of the last three transfers. In this time, position control is conducted with sub-meter accuracy to guarantee safe transfer trajectories. When all satellites reached the PCO configuration with $1000\,\text{m}$ baseline, the minimal distance rises to $680\,\text{m}$. A PCO configuration is maintained for three weeks at different baselines, rising up to $3000\,\text{m}$. This period gives the possibility to accurately analyse the impact of differential perturbation forces on the formation. In the end of the phase, the PCO-establishment process is again conducted in reverse order, bringing the satellites back to a one-dimensional ATF configuration.

The last part of the mission is foreseen to establish the three-dimensional cartwheel formation (see section 3.4). Similar to PCO, establishment of the initial CWF configuration demands an iterative process, one satellite at a time (see section 6.4.3). During the transfer manoeuvres, the inter-satellite distance also drops to $120\,\text{m}$ for a short time, while position is controlled at sub-meter accuracy. In the final $700\,\text{m}$ CWF configuration, the nominal distance is $380\,\text{m}$. This baseline is maintained for one week to get a deep insight on formation behaviour in three dimensions. The mission finishes with the consecutive transfer of all satellites to the one-dimensional ATF configuration. Once reached, the spacecraft are separated to a safe distance of $20\,\text{km}$ baseline.

The whole plan takes 150 days. For the consecutive transfer manoeuvres, the order of the satellites was chosen with respect to optimal fuel balancing in the fleet. At the end of
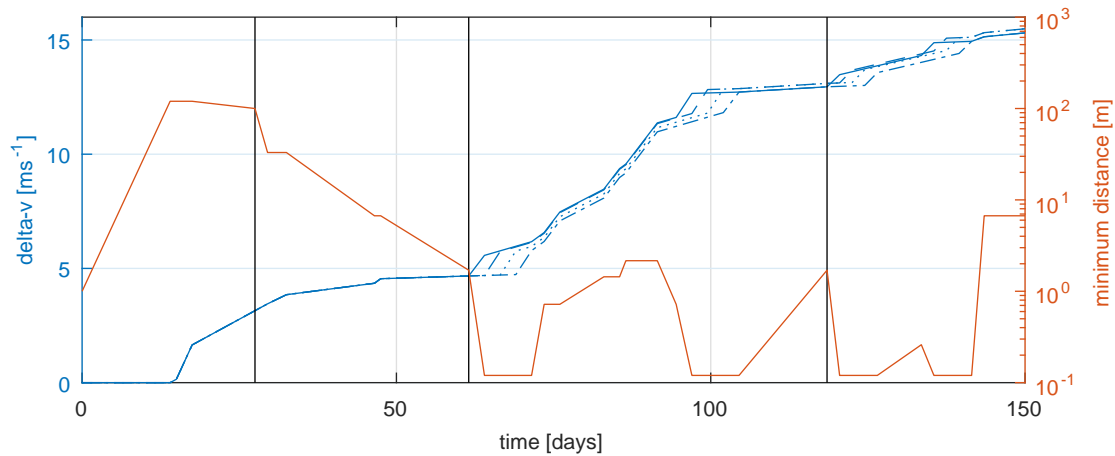
FIGURE 7.1: Delta-v of all four satellites and minimum inter-satellite distance over mission time for the proposed plan. The vertical black lines divide the mission time into the four phases as described in table 7.1.

the proposed mission, each satellite will have consumed around $15.5\,\mathrm{m\,s^{-1}}$ delta-v. The total available amount per satellite is expected to be almost twice as high, $30\,\mathrm{m\,s^{-1}}$. This gives enough room for model uncertainties and unexpected events during the mission without inferring the overall plan. The delta-v consumption of all four satellites as well as the minimal inter-satellite distance per action are depicted in figure 7.1 for the whole proposed mission. It reveals the nearly optimal fuel balancing between the four spacecraft. The figure is divided into the four phases stated before by vertical black lines. With the proposed plan, all objectives in terms of formation configuration of the *NetSat* mission are met. The plan includes one-, two- and three-dimensional phases, each with enough time to conduct detailed analyses fo the configuration properties.

7.2 Further work

Some subsystems, which are not in the scope of this thesis, are only coarsely defined by now. As soon as more detailed models are available, they should be integrated in the software framework. After the integration, all manoeuvres of the mission should be simulated again to obtain more precise delta-v estimates. This accounts in particular to the power and attitude subsystem, since they have the largest influence on the on-board controller. Furthermore, error models for the propagator and controller input variables should be developed. This may have an impact on possible manoeuvres to be flown, if the relative positioning error rises significantly as a consequence of input errors. However, this seems to be unlikely. The input only relies on data which can be obtained via GNSS measurements to a very high degree of accuracy. Moreover, to use the developed controllers on-board a satellite, a detailed stability analysis has to be conducted. Also, formation behaviour in non-nominal mode has to be analysed. Non-nominal events could be, for example, impeded inter-satellite communication, thruster malfunction of a single satellite or the total loss of a spacecraft. To further optimise delta-v consumption, the individual spacecraft could be combined to a MIMO control structure

(see section 2.4.2). The control plant combination would lead to optimal thrust profiles on fleet-level. In the final design of the spacecraft, all competing goals of the satellite subsystems must be combined. Edlerman and Kronhaus (2016) provide a long-term analysis in regard of power constraints and attitude fulfilling for satellite formations using electric propulsion. Long-term controller effectiveness on a fleet level may also be raised with adaptive cooperative control between the members of the formation, as outlined in Chang, Chung, and Blackmore (2010). Another possibility to increase global control optimality is decentralised overlapping feedback between satellite controllers (Stipanović et al., 2004).

TABLE 7.1: Proposed mission plan.

Phase	Days	Dim	Action	delta-v $[ms^{-1}]$			
1	14	-	initially uncontrolled phase	— 0 —			
	1	-	match δa	— 0.15 —			
	2.5	1	mitigate δe and δi	— 1.5 —			
	10	1	go to ATF100k	— 1.5 —			
2	2	1	keep ATF100k	— 0.3 —			
	3	1	go to ATF20k	— 0.4 —			
	14	1	keep ATF20k	— 0.5 —			
	1	1	got to ATF5000	— 0.2 —			
	14	1	keep ATF5000	— 0.12 —			
3	2.5	2	first satellite to PCO1000	0.9	0.02	0.02	0.02
	2.5	2	second satellite to PCO1000	0.2	1.05	0.02	0.02
	2.5	2	third satellite to PCO1000	0.2	0.2	1.05	0.02
	2.5	2	fourth satellite to PCO1000	0.2	0.2	0.2	1.05
	2	2	keep PCO1000	— 0.4 —			
	2.5	2	go to PCO2000	— 0.9 —			
	7	2	keep PCO2000	— 1.0 —			
	2.5	2	go to PCO3000	— 0.9 —			
	1	2	keep PCO3000	— 0.2 —			
	5	2	go to PCO1000	— 1.8 —			
	3	2	keep PCO1000	— 0.24 —			
	2.5	2	first satellite to ATF5000	1.05	0.2	0.2	0.2
	2.5	2	second satellite to ATF5000	0.02	1.05	0.2	0.2
	2.5	2	third satellite to ATF5000	0.02	0.02	1.05	0.2
	2.5	2	fourth satellite to ATF5000	0.02	0.02	0.02	0.9
	14	1	keep ATF5000	— 0.23 —			
4	2	3	first satellite to CWF700	0.53	0.02	0.02	0.02
	2	3	second satellite to CWF700	0.13	0.56	0.02	0.02
	2	3	third satellite to CWF700	0.13	0.13	0.56	0.02
	2	3	fourth satellite to CWF700	0.13	0.13	0.13	0.56
	7	3	keep CWF700	— 0.45 —			
	2	3	first satellite to ATF5000	0.56	0.13	0.13	0.13
	2	3	second satellite to ATF5000	0.02	0.56	0.13	0.13
	2	3	third satellite to ATF5000	0.02	0.02	0.56	0.13
	2	3	fourth satellite to ATF5000	0.02	0.02	0.02	0.53
	2	1	go to ATF20k	— 0.2 —			
	6.5	1	keep ATF20	— 0.17 —			
	150		**End of mission**	**15.31**	**15.49**	**15.49**	**15.31**

Appendix A

Brouwer transformation

This appendix contains the explicit formulation of the mean-to-osculating orbit transformation stated in equation (2.55). The formulation is split into one long-periodic and two short-periodic parts. All input variables have to be mean orbital values. The transformation makes use of the following variables:

$$\eta = \sqrt{1 - e^2} \tag{A.1a}$$

$$\Theta = \frac{1}{1 - 5\cos^2 i} \tag{A.1b}$$

$$\epsilon_1 = \sqrt{q_1^2 + q_2^2} \tag{A.1c}$$

$$\epsilon_2 = q_1 \cos \Theta + q_2 \sin \Theta \tag{A.1d}$$

$$\epsilon_3 = q_1 \sin \Theta - q_2 \cos \Theta \tag{A.1e}$$

The elements of $\boldsymbol{\Delta a_{lp}}\,(\bar{a})$ are:

$$a_{lp} = 0 \tag{A.2a}$$

$$\lambda_{lp} = \frac{q_1 q_2 \sin^2 i}{8a^2\eta^2\,(1+\eta)}\left(1 - 10\Theta\cos^2 i\right)$$
$$+ \frac{q_1 q_2}{16a^2\eta^4}\left(3 - 55\cos^2 i - 280\Theta\cos^4 i - 400\Theta\Theta\cos^6 i\right) \tag{A.2b}$$

$$\theta_{lp} = \lambda_{lp} - \frac{\sin^2 i}{16a^2\eta^4}\left(1 - 10\Theta\cos^2 i\right)$$
$$\left[q_1 q_2\left(3 + 2\frac{\eta^2}{1+\eta}\right) + 2\left(q_1\sin\Theta + q_2\cos\Theta\right) + \frac{\epsilon_1\sin\left(2\theta\right)}{2}\right] \tag{A.2c}$$

$$i_{lp} = \frac{\sin\left(2i\right)}{32a^2\eta^4}\left(1 - 10\Theta\cos^2 i\right)\left(q_1^2 - q_2^2\right) \tag{A.2d}$$

$$q_{1,lp} = -\frac{q_1 \sin^2 i}{16a^2\eta^2}\left(1 - 10\Theta\cos^2 i\right)$$

$$-\frac{q_1 q_2^2}{16a^2\eta^4}\left(3 - 55\cos^2 i - 280\Theta\cos^4 i - 400\Theta\Theta\cos^6 i\right) \tag{A.2e}$$

$$q_{2,lp} = \frac{q_2\sin^2 i}{16a^2\eta^2}\left(1 - 10\Theta\cos^2 i\right)$$

$$+\frac{q_1^2 q_2}{16a^2\eta^4}\left(3 - 55\cos^2 i - 280\Theta\cos^4 i - 400\Theta\Theta\cos^6 i\right) \tag{A.2f}$$

$$\Omega_{lp} = \frac{q_1 q_2\cos i}{8a^2\eta^4}\left(11 + 80\Theta\cos^2 i + 200\Theta\Theta\cos^4 i\right) \tag{A.2g}$$

The elements of $\mathbf{\Delta a_{sp1}}(\bar{\mathbf{a}})$ are:

$$a_{sp1} = \frac{1 - 3\cos^2 i}{2a\eta^6}\left(\epsilon_2^3 - \eta^3\right) \tag{A.3a}$$

$$\lambda_{sp1} = \frac{\epsilon_3\left(1 - 3\cos^2 i\right)}{4a^2\eta^4\left(1 + \eta\right)}\left[(1 + \epsilon_2)^2 + 1 + \epsilon_2 + \eta^2\right]$$

$$+\frac{3\left(1 - 5\cos^2 i\right)}{4a^2\eta^4}\left(\theta - \lambda + \epsilon_3\right) \tag{A.3b}$$

$$\theta_{sp1} = \lambda_{sp1} - \frac{\epsilon_3\left(1 - 3\cos^2 i\right)}{4a^2\eta^4\left(1 + \eta\right)}\left[(1 + \epsilon_2)^2 + \eta\left(1 + \eta\right)\right] \tag{A.3c}$$

$$i_{sp1} = 0 \tag{A.3d}$$

$$q_{1,sp1} = \frac{1 - 3\cos^2 i}{4a^2\eta^4\left(1 + \eta\right)}\left[\left(\epsilon_2^2 + \eta^2\right)\left(q_1 + (1 + \eta)\cos\Theta\right)\right.$$

$$\left.(1 + \epsilon_2)\left[(1 + \eta)\cos\Theta + q_1\left(\eta - \epsilon_2\right)\right]\right] \tag{A.3e}$$

$$-\frac{3q_2\left(1 - 5\cos^2 i\right)}{4a^2\eta^4}\left(\theta - \lambda + \epsilon_3\right)$$

$$q_{2,sp1} = \frac{1 - 3\cos^2 i}{4a^2\eta^4\left(1 + \eta\right)}\left[\left(\epsilon_2^2 + \eta^2\right)\left(q_2 + (1 + \eta)\sin\Theta\right)\right.$$

$$\left.(1 + \epsilon_2)\left[(1 + \eta)\sin\Theta + q_2\left(\eta - \epsilon_2\right)\right]\right] \tag{A.3f}$$

$$+\frac{3q_1\left(1 - 5\cos^2 i\right)}{4a^2\eta^4}\left(\theta - \lambda + \epsilon_3\right)$$

$$\Omega_{sp1} = \frac{3\cos i}{2a^2\eta^4}\left(\theta - \lambda + \epsilon_3\right) \tag{A.3g}$$

The elements of $\boldsymbol{\Delta a_{sp2}}\,(\bar{a})$ are:

$$a_{sp2} = -\frac{3\sin^2 i}{2a\eta^6}\epsilon_2^3\cos(2\theta) \tag{A.4a}$$

$$\lambda_{sp2} = -\frac{3\epsilon_3\sin^2 i\cos(2\theta)}{4a^2\eta^4\,(1+\eta)}\,(1+\epsilon_1)\,(2+\epsilon_2) - \frac{\sin^2 i}{8a^2\eta^2\,(1+\eta)}$$

$$[3\,(q_1\sin\Theta + q_2\cos\Theta) + (q_1\sin(3\theta) - q_2\cos(3\theta))]$$

$$-\frac{3-5\cos^2 i}{8a^2\eta^4}\,[3\,(q_1\sin\Theta + q_2\cos\Theta) + 3\sin(2\theta)$$

$$+\,(q_1\sin(3\theta) - q_2\cos(3\theta))] \tag{A.4b}$$

$$\theta_{sp2} = \lambda_{sp2} - \frac{\sin^2 i}{32a^2\eta^4\,(1+\eta)}\,\big[36q_1q_2 - 4\,(3\eta^2 + 5\eta - 1)$$

$$(q_1\sin\Theta + q_2\cos\Theta) + 12\epsilon_2 q_1q_2 - 32\,(1+\eta)\sin(2\theta)$$

$$-\,(\eta^2 + 12\eta + 39)\,(q_1\sin(3\theta) - q_2\cos(3\theta)) \tag{A.4c}$$

$$+36q_1q_2\cos(4\theta) - 18\,(q_1^2 - q_2^2)\sin(4\theta)$$

$$-3\,(q_1^2 - 3q_2^2)\,q_1\sin(5\theta) + 3\,(3q_1^2 - q_2^2)\,q_2\cos(5\theta)\big]$$

$$i_{sp2} = -\frac{\sin(2i)}{8a^2\eta^4}\,[3\,(q_1\cos\Theta - q_2\sin\Theta) + 3\cos(2\theta)$$

$$+\,(q_1\cos(3\theta) + q_2\sin(3\theta))] \tag{A.4d}$$

$$q_{1,sp2} = \frac{q_2\,(3 - 5\cos^2 i)}{8a^2\eta^4}\,[3\,(q_1\sin\Theta + q_2\cos\Theta) + 3\sin(2\theta)$$

$$+\,(q_1\sin(3\theta) - q_2\cos(3\theta))]$$

$$+\frac{\sin^2 i}{8a^2\eta^4}\,[3\,(\eta^2 - q_1^2)\cos\Theta + 3q_1q_2\sin\Theta$$

$$-\,(\eta^2 + 3q_1^2)\cos(3\theta) - 3q_1q_2\sin(3\theta)] \tag{A.4e}$$

$$-\frac{3\sin^2 i\cos(2\theta)}{16a^2\eta^4}\,\big[10q_1 + (8 + 3q_1^2 + q_2^2)\cos\Theta$$

$$+2q_1q_2\sin\Theta + 6\,(q_1\cos(2\theta) + q_2\sin(2\theta))$$

$$+\,(q_1^2 - q_2^2)\cos(3\theta) + 2q_1q_2\sin(3\theta)\big]$$

$$q_{2,sp2} = -\frac{q_1\left(3 - 5\cos^2 i\right)}{8a^2\eta^4}\left[3\left(q_1\sin\Theta + q_2\cos\Theta\right) + 3\sin\left(2\theta\right)\right.$$

$$\left. + \left(q_1\sin\left(3\theta\right) - q_2\cos\left(3\theta\right)\right)\right]$$

$$\frac{\sin^2 i}{8a^2\eta^4}\left[3\left(\eta^2 - q_2^2\right)\sin\Theta + 3q_1q_2\cos\Theta\right.$$

$$\left. + \left(\eta^2 + 3q_2^2\right)\sin\left(3\theta\right) + 3q_1q_2\cos\left(3\theta\right)\right] \tag{A.4f}$$

$$-\frac{3\sin^2 i\cos\left(2\theta\right)}{16a^2\eta^4}\left[10q_2 + \left(8 + q_1^2 + 3q_2^2\right)\sin\Theta\right.$$

$$+2q_1q_2\cos\Theta + 6\left(q_1\sin\left(2\theta\right) - q_2\cos\left(2\theta\right)\right)$$

$$\left. + \left(q_1^2 - q_2^2\right)\sin\left(3\theta\right) - 2q_1q_2\cos\left(3\theta\right)\right]$$

$$\Omega_{sp2} = -\frac{\cos i}{4a^2\eta^4}\left[3\left(q_1\sin\Theta + q_2\cos\Theta\right)\right.$$

$$\left. +3\sin\left(2\theta\right) + \left(q_1\sin\left(3\theta\right) - q_2\cos\left(3\theta\right)\right)\right] \tag{A.4g}$$

Appendix B

Simplified differential mean to osculation transformation

Elements of the matrix $\mathbf{D_s}$ defined in equation (2.68). All matrix elements which are not stated below are zero. The matrix indices start with zero. Additional variables:

$$\tau_1 = -8a^{-2}\sin^2 i \left(1 - 10\Theta\cos^2 i\right) \tag{B.1a}$$

$$\tau_2 = \left(1 - 3\cos^2 i\right) \tag{B.1b}$$

$$\tau_3 = \left(1 - 5\cos^2 i\right) \tag{B.1c}$$

Long-periodic part of $\mathbf{D_s}$:

$$D_{1,3}^{lp} = \tau_1 \sin\Theta$$

$$D_{1,4}^{lp} = \tau_1 \cos\theta \tag{B.2a}$$

$$D_{3,3}^{lp} = 0.5\tau_1 \tag{B.2b}$$

$$D_{4,4}^{lp} = -0.5\tau_1 \tag{B.2c}$$

Short-periodic(1) part of $\mathbf{D_s}$:

$$D_{0,3}^{sp1} = 3\tau_2 \frac{\cos\Theta}{2a}$$

$$D_{0,4}^{sp1} = 3\tau_2 \frac{\sin\Theta}{2a} \tag{B.3a}$$

$$D_{1,3}^{sp1} = 9\tau_3 \frac{\sin\Theta}{4a^2}$$

$$D_{1,4}^{sp1} = -9\tau_3 \frac{\cos\Theta}{4a^2} \tag{B.3b}$$

$$D_{3,0}^{sp1} = -3\tau_2 \frac{\cos \Theta}{2a^3}$$

$$D_{3,1}^{sp1} = -3\tau_2 \frac{\sin \Theta}{4a^2}$$

$$D_{3,2}^{sp1} = 9\sin(2i) \frac{\cos \Theta}{4a^2} \tag{B.3c}$$

$$D_{3,3}^{sp1} = 3\tau_2 \frac{2 + \cos(2\Theta)}{8a^2}$$

$$D_{3,4}^{sp1} = 3\tau_2 \frac{\sin(2\Theta)}{8a^2}$$

$$D_{4,0}^{sp1} = -3\tau_2 \frac{\sin \Theta}{2a^3}$$

$$D_{4,1}^{sp1} = 3\tau_2 \frac{\cos \Theta}{4a^2}$$

$$D_{4,2}^{sp1} = 9\sin(2i) \frac{\sin \Theta}{4a^2} \tag{B.3d}$$

$$D_{4,3}^{sp1} = 3\tau_2 \frac{\sin(2\Theta)}{8a^2}$$

$$D_{4,4}^{sp1} = 3\tau_2 \frac{2 - \cos(2\Theta)}{8a^2}$$

$$D_{5,3}^{sp1} = 9\cos i \frac{\sin \Theta}{4a^2}$$

$$\tag{B.3e}$$

$$D_{5,4}^{sp1} = -9\cos i \frac{\cos \Theta}{4a^2}$$

Short-periodic(2) part of $\mathbf{D_s}$:

$$D_{0,0}^{sp2} = 3\sin^2 i \frac{\cos(2\Theta)}{2a^2}$$

$$D_{0,1}^{sp2} = 3\sin^2 i \frac{\sin(2\Theta)}{a}$$

$$D_{0,2}^{sp2} = -3\sin(2i)\frac{\cos(2\Theta)}{2a} \tag{B.4a}$$

$$D_{0,3}^{sp2} = -9\sin^2 i \frac{\cos\Theta + \cos(3\Theta)}{4a}$$

$$D_{0,4}^{sp2} = 9\sin^2 i \frac{\sin\Theta - \sin(3\Theta)}{4a}$$

$$D_{1,0}^{sp2} = -(6 - 7\sin^2 i)\frac{\sin(2\Theta)}{4a^3}$$

$$D_{1,1}^{sp2} = (6 - 7\sin^2 i)\frac{\cos(2\Theta)}{4a^2}$$

$$D_{1,2}^{sp2} = -7\sin(2i)\frac{\sin(2\Theta)}{8a^2} \tag{B.4b}$$

$$D_{1,3}^{sp2} = \frac{24 - 47\sin^2 i}{32a^2}\sin\Theta + \frac{\cos^2 i \sin(3\Theta)}{4a^2}$$

$$D_{1,4}^{sp2} = \frac{24 - 47\sin^2 i}{32a^2}\cos\Theta - \frac{\cos^2 i \cos(3\Theta)}{4a^2}$$

$$D_{2,0}^{sp2} = \frac{3\sin(2i)\cos(2\Theta)}{4a^3}$$

$$D_{2,1}^{sp2} = \frac{3\sin(2i)\sin(2\Theta)}{4a^2}$$

$$D_{2,2}^{sp2} = -\frac{3\cos(2i)\cos(2\Theta)}{4a^2} \tag{B.4c}$$

$$D_{2,3}^{sp2} = -\frac{\sin(2i)}{8a^2}(3\cos\Theta + \cos(3\Theta))$$

$$D_{2,4}^{sp2} = \frac{\sin(2i)}{8a^2}(3\sin\Theta - \sin(3\Theta))$$

$$D_{3,0}^{sp2} = \frac{\sin^2 i}{4a^3}(3\cos\Theta + 7\cos(3\Theta))$$

$$D_{3,1}^{sp2} = \frac{3\sin^2 i}{8a^2}(\sin\Theta + 7\sin(3\Theta))$$

$$D_{3,2}^{sp2} = -\frac{\sin(2i)}{8a^2}(3\cos\Theta + 7\cos(3\Theta)) \qquad \text{(B.4d)}$$

$$D_{3,3}^{sp2} = -\frac{3\sin^2 i}{16a^2}(3 + 10\cos(2\Theta) + 3\cos(4\Theta))$$

$$D_{3,4}^{sp2} = \frac{3(3 - 5\cos^2 i)}{8a^2}\sin(2\Theta) - \frac{9\sin^2 i \sin(4\Theta)}{16a^2}$$

$$D_{4,0}^{sp2} = -\frac{\sin^2 i}{4a^3}(3\sin\Theta - 7\sin(3\Theta))$$

$$D_{4,1}^{sp2} = \frac{3\sin^2 i}{8a^2}(\cos\Theta - 7\cos(3\Theta))$$

$$D_{4,2}^{sp2} = \frac{\sin(2i)}{8a^2}(3\sin\Theta - 7\sin(3\Theta)) \qquad \text{(B.4e)}$$

$$D_{4,3}^{sp2} = -\frac{3(3 - 5\cos^2 i)\sin(2\Theta)}{8a^2} - \frac{9\sin^2 i \sin(4\Theta)}{16a^2}$$

$$D_{4,4}^{sp2} = \frac{3\sin^2 i}{16a^2}(3 - 10\cos(2\Theta) + 3\cos(4\Theta))$$

$$D_{5,0}^{sp2} = \frac{3\cos i \sin(2\Theta)}{2a^3}$$

$$D_{5,1}^{sp2} = -\frac{3\cos i \cos(2\Theta)}{2a^2}$$

$$D_{5,2}^{sp2} = \frac{3\sin i \sin(2\Theta)}{4a^2} \qquad \text{(B.4f)}$$

$$D_{5,3}^{sp2} = -\frac{\cos i}{4a^2}(3\sin\Theta + \sin(3\Theta))$$

$$D_{5,4}^{sp2} = -\frac{\cos i}{4a^2}(3\cos\Theta - \cos(3\Theta))$$

Appendix C

DOE to Hill-frame transformation

Elements of the frame conversion matrix $\boldsymbol{\Sigma}\left(\mathbf{a}\right)$ between osculating differential orbital elements and the Hill-frame. All elements not stated below are zero. Matrix indices start with zeros. Additional variables:

$$V_r = \sqrt{\frac{\mu}{p}}\left(q_1 \sin\theta - q_2 \cos\theta\right) \tag{C.1a}$$

$$V_t = \sqrt{\frac{\mu}{p}}\left(1 + q_1 \cos\theta + q_2 \sin\theta\right) \tag{C.1b}$$

$$r = \frac{p}{1 + q_1 \cos\theta + q_2 \sin\theta} \tag{C.1c}$$

Elements of $\boldsymbol{\Sigma}\left(\mathbf{a}\right)$:

$$\Sigma_{0,0} = \frac{r}{a}$$

$$\Sigma_{0,1} = \frac{rV_r}{V_t}$$

$$\Sigma_{0,3} = -\frac{2raq_1}{p} - \frac{r^2 \cos\theta}{p} \tag{C.2a}$$

$$\Sigma_{0,4} = -\frac{2raq_2}{p} - \frac{r^2 \sin\theta}{p}$$

$$\Sigma_{1,0} = -\frac{V_r}{2a}$$

$$\Sigma_{1,1} = \frac{V_t}{p}\left(r - p\right)$$

$$\Sigma_{1,3} = \frac{V_r a q_1}{p} + \frac{r V_t \sin\theta}{p}$$

$$\Sigma_{1,4} = \frac{V_r a q_2}{p} - \frac{r V_t \cos\theta}{p}$$

(C.2b)

$$\Sigma_{2,1} = r$$

$$\Sigma_{2,5} = r \cos i$$

(C.2c)

$$\Sigma_{3,0} = -\frac{3V_t}{2a}$$

$$\Sigma_{3,1} = -V_r$$

$$\Sigma_{3,2} = -\alpha\frac{V_t \sin i \cos i \sin^2\theta}{pr}$$

$$\Sigma_{3,3} = \frac{V_t}{p}\left(3aq_1 + 2r\cos\theta\right)$$

$$\Sigma_{3,4} = \frac{V_t}{p}\left(3aq_2 + 2r\sin\theta\right)$$

$$\Sigma_{3,5} = V_r \cos i + \alpha\frac{V_t \sin^2 i \cos i \sin\theta \cos\theta}{pr}$$

(C.2d)

$$\Sigma_{4,2} = r \sin\theta$$

$$\Sigma_{4,5} = -r \sin i \cos\theta$$

(C.2e)

$$\Sigma_{5,1} = \alpha \frac{V_t \sin i \cos i \sin \theta}{pr}$$

$$\Sigma_{5,2} = (V_t \cos \theta + V_r \sin \theta) \tag{C.2f}$$

$$\Sigma_{5,5} = (V_t \sin \theta - V_r \cos \theta) \sin i + \alpha \frac{V_t \sin i \cos^2 i \sin \theta}{pr}$$

Appendix D

Mean orbital elements state transition matrix

Elements of the state transition matrix for the mean orbital elements $\phi\left(t_o, t_1\right)$. All elements not stated below are zero. Matrix indices start with zeros. Additional variables:

$$V_r = \sqrt{\frac{\mu}{p}}\left(q_1 \sin\theta - q_2 \cos\theta\right) \tag{D.1a}$$

$$V_t = \sqrt{\frac{\mu}{p}}\left(1 + q_1 \cos\theta + q_2 \sin\theta\right) \tag{D.1b}$$

$$\sin\Delta\omega = \sin\left(\dot{\omega}\left(t_1 - t_0\right)\right) \tag{D.1c}$$

$$\cos\Delta\omega = \cos\left(\dot{\omega}\left(t_1 - t_0\right)\right) \tag{D.1d}$$

$$G_\theta = \frac{nR}{V_t} \tag{D.1e}$$

$$G_{q1} = \frac{q_2}{\eta(1+\eta)} + \frac{q_1 V_r}{\eta V_t} - \eta R\frac{a+R}{p^2}\left(q_2 + \sin\theta\right) \tag{D.1f}$$

$$G_{q2} = -\frac{q_1}{\eta(1+\eta)} + \frac{q_2 V_r}{\eta V_t} + \eta R\frac{a+R}{p^2}\left(q_1 + \cos\theta\right) \tag{D.1g}$$

$$K = 1 + G_{q1}\left(q_{10} \sin\Delta\omega + q_{20} \cos\Delta\omega\right) \tag{D.1h}$$

$$- G_{q2}\left(q_{10} \cos\Delta\omega - q_{20} \sin\Delta\omega\right) \tag{D.1i}$$

Elements of $\phi\left(t_o, t_1\right)$:

$$\phi_{0,0} = 1 \tag{D.2a}$$

$$\phi_{1,0} = -\frac{(t_1 - t_0)}{G_\theta} \left[\frac{3n_0}{2a_0} + \frac{7\epsilon n_0}{8a_0 p_0^2} \left(\eta_0 \left(3\cos^2 i_0 - 1 \right) \right. \right.$$

$$\left. \left. + K \left(5\cos^2 i_0 - 1 \right) \right) \right]$$

$$\phi_{1,1} = -\frac{G_{\theta_0}}{G_\theta}$$

$$\phi_{1,2} = -\frac{(t_1 - t_0)}{G_\theta} \frac{\epsilon n_0}{2p_0^2} \sin i_0 \cos i_0 (3\eta_0 + 5K)$$

$$\phi_{1,3} = -\frac{1}{G_\theta} \left(G_{q_{10}} + \cos \Delta\omega G_{q_1} + \sin \Delta\omega G_{q_2} \right) \tag{D.2b}$$

$$+ \frac{(t_1 - t_0) \epsilon a_0 n_0 q_{10}}{G_\theta 4p_0^3} \left[3\eta_0 \left(3\cos^2 i_0 - 1 \right) \right.$$

$$\left. + 4K \left(5\cos^2 i_0 - 1 \right) \right]$$

$$\phi_{1,4} = -\frac{1}{G_\theta} \left(G_{q_{20}} - \sin \Delta\omega G_{q_1} + \cos \Delta\omega G_{q_2} \right)$$

$$+ \frac{(t_1 - t_0) \epsilon a_0 n_0 q_{20}}{G_\theta 4p_0^3} \left[3\eta_0 \left(3\cos^2 i_0 - 1 \right) \right.$$

$$\left. + 4K \left(5\cos^2 i_0 - 1 \right) \right]$$

$$\phi_{2,2} = 1 \tag{D.2c}$$

$$\phi_{3,0} = \frac{7\epsilon n_0}{8a_0 p_0^2} \left(q_{10} \sin \Delta\omega + q_{20} \cos \Delta\omega \right) \left(5\cos^2 i_0 - 1 \right) (t_1 - t_0)$$

$$\phi_{3,2} = \frac{5\epsilon n_0}{2p_0^2} \left(q_{10} \sin \Delta\omega + q_{20} \cos \Delta\omega \right) \left(\sin i_0 \cos i_0 \right) (t_1 - t_0)$$

$$\phi_{3,3} = \cos \Delta\omega - \frac{\epsilon a_0 n_0 q_{10}}{p_0^3} \left(q_{10} \sin \Delta\omega + q_{20} \cos \Delta\omega \right) \tag{D.2d}$$

$$\left(5\cos^2 i_0 - 1 \right) (t_1 - t_0)$$

$$\phi_{3,4} = -\sin \Delta\omega - \frac{\epsilon a_0 n_0 q_{20}}{p_0^3} \left(q_{10} \sin \Delta\omega + q_{20} \cos \Delta\omega \right)$$

$$\left(5\cos^2 i_0 - 1 \right) (t_1 - t_0)$$

$$\phi_{4,0} = -\frac{7\epsilon n_0}{8a_0 p_0^2}\left(q_{10}\cos\Delta\omega - q_{20}\sin\Delta\omega\right)\left(5\cos^2 i_0 - 1\right)(t_1 - t_0)$$

$$\phi_{4,2} = -\frac{5\epsilon n_0}{2p_0^2}\left(q_{10}\cos\Delta\omega - q_{20}\sin\Delta\omega\right)\left(\sin i_0 \cos i_0\right)(t_1 - t_0)$$

$$\phi_{4,3} = \sin\Delta\omega + \frac{\epsilon a_0 n_0 q_{10}}{p_0^3}\left(q_{10}\cos\Delta\omega - q_{20}\sin\Delta\omega\right)$$

$$\left(5\cos^2 i_0 - 1\right)(t_1 - t_0)$$

$$\phi_{4,4} = \cos\Delta\omega + \frac{\epsilon a_0 n_0 q_{20}}{p_0^3}\left(q_{10}\cos\Delta\omega - q_{20}\sin\Delta\omega\right)$$

$$\left(5\cos^2 i_0 - 1\right)(t_1 - t_0)$$

(D.2e)

$$\phi_{5,0} = \frac{7\epsilon n_0 \cos i_0 (t_1 - t_0)}{4a_0 p_0^2}$$

$$\phi_{5,2} = \frac{\epsilon n_0 \sin i_0 (t_1 - t_0)}{2p_0^2}$$

$$\phi_{5,3} = -\frac{2\epsilon n_0 a_0 q_{10} \cos i_0 (t_1 - t_0)}{p_0^3}$$

$$\phi_{5,4} = -\frac{2\epsilon n_0 a_0 q_{20} \cos i_0 (t_1 - t_0)}{p_0^3}$$

$$\phi_{5,5} = 1$$

(D.2f)

Appendix E

Database types

This table lists all available datatypes in the configuration database of the software framework (see section 4.2.2). Each database entry is connected to a specific Java class, which is used when the CSV database is automatically converted to Java source code. The input column specifies all values needed to create a default value for a parameter in the CSV-file, separated by commas. The output column lists all floating-point values which are sent over the network interface when debug output is enabled for a specific parameter. "av" stands for atomic value and is only used for the basic datatypes, all others have short descriptions with naming according to their domain of usage. For further information, refer to the software manual.

TABLE E.1: Available types in the configuration database.

Type	Java class	Input	Output
INTEGER	`Integer`	av	av
DOUBLE	`Double`	av	av
DOUBLE_ARRAY	`Double[]`	x0, x1, ... (up to number of elements for the array)	x0, x1, ...
BOOLEAN	`Boolean`	0 or 1	0 or 1
STRING	`String`	av	-
ABSOLUTE_DATE	`AbsoluteDate`	year, month, day, hour, minute, second (defined in UTC scale)	year, month, day, hour, minute, second (in UTC scale)
ATTITUDE	`Attitude`	date ref. table, date ref. param., q0, q1, q2, q3 (orientation quaternion), vx, vy, vz (spin vector), ax, ay, az (acceleration vector)	q0, q1, q2, q3
KEPLERIAN_ORBIT	`KeplerianOrbit`	a, e, i, oemga, Omega, f, date ref. table, date ref. param,	a, e, i, omega, Omega, f
RELATIVE_ORBIT	`RelativeOrbit`	ada, adex, adey, adix, adiy, adu, abs. orbit ref. table, abs. orbit ref. param., abs. orbit update flag	ada, adex, adey, adix, adiy, adu
RELATIVE_ORBIT_ELEMENTS	`RelativeOrbit Elements`	ada, adex, adey, adix, adiy, adu	ada, adex, adey, adix, adiy, adu
TIMESTAMPED_PVCOORDINATES	`TimeStampedPV Coordinates`	x, y, z (position vector), vx, vy, vz (velocity vector), date ref. table, date ref. param	x, y, z, vx, vy, vz
VECTOR3D	`Vector3D`	x, y, z	x, y, z
INTERVAL_DOUBLE	`Interval <Double>`	lower bound, upper bound	lower bound, upper bound
INTERVAL_INTEGER	`Interval <Integer>`	lower bound, upper bound	lower bound, upper bound
SPLINE_MANOEUVRE	`SplineManoeuvre`	-	-
MOEA_OPTION_DOUBLE	`MoeaOption <Double>`	name, value	-
MOEA_OPTION_INTEGER	`MoeaOption <Integer>`	name, value	-
SUBSYSTEM_ DEFINITION	`Subsystem Definition`	Java class name, active flag, execution interval, unique execution position, verbose flag	-
DMREFERENCE	`DMEntry Reference<?>`	table name, parameter name	-

Bibliography

Alfriend, Kyle T., Hanspeter Schaub, and Dong-Woo Gim (2000). "Gravitational Perturbations, Nonlinearity and Circular Orbit Assumption Effects on Formation Flying Control Strategies". In: vol. AAS 00-012. American Astronautical Society.

Alfriend, Kyle T. et al. (2010). *Spacecraft formation flying: dynamics, control, and navigation*. eng. Elsevier astrodynamics series. OCLC: 699265912. Oxford: Butterworth-Heinemann/Elsevier.

Ardaens, Jean-Sébastien et al. (2008). "Tandem-x autonomous formation flying system". In: *3rd International Symposium on Formation Flying, Missions and Technology*, pp. 23–25.

Armellin, Roberto, Mauro Massari, and Amalia Ercoli Finzi (2004). "Optimal formation flying reconfiguration and station keeping maneuvers using low thrust propulsion". In: *18th International Symposium on Space Flight Dynamics*. Vol. 548. Munich, Germany: Oct, p. 429.

Barza, Radu, Yohko Aoki, and Klaus Schilling (2006). "CubeSat UWE-1–technology tests and in orbit results". In: *57th International Astronautical Congress*.

Bate, Roger R., Donald D. Mueller, and Jerry E. White (1971). *Fundamentals of astrodynamics*. Courier Corporation.

Battin, Richard H. (1999). *An introduction to the mathematics and methods of astrodynamics*. Aiaa.

Bonin, Grant et al. (2015). "CanX–4 and CanX–5 Precision Formation Flight: Mission Accomplished!" In:

Breger, Louis and Jonathan P. How (2005). "J2-modified GVE-based MPC for formation flying spacecraft". In: *AIAA Guid. Navig. Contr. Conf. Exhi*, pp. 1–12.

– (2007). "Gauss's variational equation-based dynamics and control for formation flying spacecraft". In: *Journal of guidance, control, and dynamics* 30.2, pp. 437–448.

Broucke, Roger A. (2003). "Solution of the elliptic rendezvous problem with the time as independent variable". In: *Journal of Guidance, Control, and Dynamics* 26.4, pp. 615–621.

Broucke, Roger A. and Paul J. Cefola (1972). "On the equinoctial orbit elements". In: *Celestial Mechanics* 5.3, pp. 303–310.

Brouwer, Dirk (1959). "Solution of the problem of artificial satellite theory without drag". In: *The Astronomical Journal* 64, p. 378.

Busch, S., P. Bangert, and K. Schilling (2014). "Attitude control demonstration for pico-satellite formation flying by UWE-3". In: *Proceedings of the 4S-Symposium, Mallorca*.

Carter, Thomas E. (1998). "State transition matrices for terminal rendezvous studies: brief survey and new example". In: *Journal of Guidance, Control, and Dynamics* 21.1, pp. 148–155.

Chang, Dong Eui and Jerrold E. Marsden (2003). "Geometric derivation of the Delaunay variables and geometric phases". In: *Celestial Mechanics and Dynamical Astronomy* 86.2, pp. 185–208.

Chang, Insu, Soon-Jo Chung, and Lars Blackmore (2010). "Cooperative control with adaptive graph laplacians for spacecraft formation flying". In: *49th IEEE Conference on Decision and Control (CDC)*. IEEE, pp. 4926–4933.

Chobotov, Vladimir A. (2002). *Orbital mechanics*. Aiaa.

Clohessy, W. H. and R. S. Wiltshire (1960). "Terminal guidance system for satellite rendezvous". In: *Journal of the Aerospace Sciences* 27.9, pp. 653–658.

D'Amico, Simone (2010). *Autonomous formation flying in low earth orbit*. TU Delft, Delft University of Technology.

D'Amico, Simone, J. S. Ardaens, and Robin Larsson (2011). "In-flight demonstration of formation control based on relative orbital elements". In: *4th International Conference on Spacecraft Formation Flying Missions & Technologies*, pp. 18–20.

D'Amico, Simone, Jean-Sebastien Ardaens, and Oliver Montenbruck (2009). "Navigation of formation flying spacecraft using GPS: the PRISMA technology demonstration". In: *Proceedings of the 22nd International Technical Meeting of the Satellite Division of the Institute of Navigation (ION-GNSS'09)*, pp. 2250–2264.

D'Amico, Simone, Eberhard Gill, and Oliver Montenbruck (2006). "Relative orbit control design for the PRISMA formation flying mission". In: *AIAA GNC Conference*.

D'Amico, Simone et al. (2009). "Autonomous formation keeping and reconfiguration for remote sensing spacecraft". In: *21st International Symposium on Space Flight Dynamics*. Vol. 28.

Danzmann, Karsten and LISA Science Team (2003). "LISA—an ESA cornerstone mission for the detection and observation of gravitational waves". In: *Advances in Space Research* 32.7, pp. 1233–1242.

D'Errico, Marco, ed. (2013). *Distributed space missions for Earth system monitoring*. Space technology library. OCLC: ocn794709711. New York : El Segundo, Calif: Springer ; published jointly by Microcosm Press.

Djojodihardjo, Harijono (2014). "The Influence of J2 on Formation Flying of Micro-Satellites in Low Near Equatorial Orbits". In: *Journal of Advances in Information Technology* 5.1.

Edlerman, Eviatar and Igal Kronhaus (2016). "Analysis of Electric Propulsion Capabilities in Establishment and Keeping of Formation Flying Nanosatellites". In: Darmstadt, Germany.

Eiben, Agoston E. and James E. Smith (2003). *Introduction to evolutionary computing*. Vol. 53. Springer.

Escoubet, C. P., M. Fehringer, and M. Goldstein (2001). "Introduction the Cluster mission". In: *Annales Geophysicae*. Vol. 19, pp. 1197–1200.

Eyer, Jesse Koovik (2009). "A dynamics and control algorithm for low earth orbit precision formation flying satellites". PhD thesis. University of Toronto.

Gao, Yang and Xinfeng Li (2010). "Optimization of low-thrust many-revolution transfers and Lyapunov-based guidance". In: *Acta Astronautica* 66.1, pp. 117–129.

Gim, Dong-Woo and Kyle T. Alfriend (2003). "State Transition Matrix of Relative Motion for the Perturbed Noncircular Reference Orbit". en. In: *Journal of Guidance, Control, and Dynamics* 26.6, pp. 956–971.

– (2005). "Satellite Relative Motion Using Differential Equinoctial Elements". en. In: *Celestial Mechanics and Dynamical Astronomy* 92.4, pp. 295–336.

Goodman, John Louis (2006). "History of space shuttle rendezvous and proximity operations". In: *Journal of Spacecraft and Rockets* 43.5, pp. 944–959.

Green, Colonel GB, P. D. Massatt, and N. W. Rhodus (1989). "The GPS 21 primary satellite constellation". In: *Navigation* 36.1, pp. 9–24.

Hartley, Edward N. et al. (2012). "Model predictive control system design and implementation for spacecraft rendezvous". In: *Control Engineering Practice* 20.7, pp. 695–713.

Hipparchus (2016). *Hipparchus 1.0 Java Mathematics Library*. URL: `https://www.hipparchus.org/apidocs/index.html` (visited on 11/04/2016).

Holmes, S. A. and W. E. Featherstone (2002). "A unified approach to the Clenshaw summation and the recursive computation of very high degree and order normalised associated Legendre functions". In: *Journal of Geodesy* 76.5, pp. 279–299.

Hori, Gen-ichiro (1966). "Theory of general perturbation with unspecified canonical variable". In: *Publications of the Astronomical Society of Japan* 18, p. 287.

Jiang, Fanghua, Junfeng Li, and Hexi Baoyin (2007). "Approximate analysis for relative motion of satellite formation flying in elliptical orbits". en. In: *Celestial Mechanics and Dynamical Astronomy* 98.1, pp. 31–66.

Kaplan, Marshall H. (1976). "Modern spacecraft dynamics and control". In: *New York, John Wiley and Sons, Inc., 1976. 427 p.* 1.

Kirschner, Michael, Franz-Heinrich Massmann, and Michael Steinhoff (2013). "GRACE". In: *Distributed Space Missions for Earth System Monitoring*. Springer, pp. 547–574.

Konstantinov, M. S., I. A. Nikolichev, and Min Thein (2016). "Optimization of low thrust Multi-Revolution Orbital Transfers using the Method of Dual Numbers". In:

Lawden, Derek F. (1963). *Optimal trajectories for space navigation*. Butterworths.

Lee, Daero, J. E. Cochran, and J. H. Jo (2007). "Solutions to the variational equations for relative motion of satellites". In: *Journal of Guidance, Control, and Dynamics* 30.3, pp. 669–678.

Lunze, Jan (2012). *Regelungstechnik 2: Mehrgrö\s sensysteme, Digitale Regelung*. Springer-Verlag.

Maessen, D. C. and Eberhard Gill (2010). *Relative orbital element estimation and observability analysis for formation flying satellites using inter-satellite range measurements only*. American Institute of Aeronautics and Astronautics (AIAA).

Maine, Kris, Carrie Devieux, and Pete Swan (1995). "Overview of IRIDIUM satellite network". In: *WESCON/'95. Conference record.'Microelectronics Communications Technology Producing Quality Products Mobile and Portable Power Emerging Technologies'*. IEEE, p. 483.

Maisonobe, L. and P. Parraud (2016). "From low level Toolbox to Orbit Determination: Handling Users Requests in Orekit". In:

Montenbruck, Oliver and Eberhard Gill (2012). *Satellite orbits: models, methods and applications*. Springer Science & Business Media.

Morgan, Daniel et al. (2012). "Swarm-keeping strategies for spacecraft under J2 and atmospheric drag perturbations". In: *Journal of Guidance, Control, and Dynamics* 35.5, pp. 1492–1506.

Myatt, D. R. et al. (2004). "Advanced global optimisation for mission analysis and design". In: *Final Report. Ariadna id* 3, p. 4101.

Nicholas, Austin Kyle (2013). "Attitude and formation control design and system simulation for a three-satellite CubeSat mission". PhD thesis. Massachusetts Institute of Technology.

OREKIT (2016). *OREKIT 8.0 Spaceflight Dynamics Java Library*. URL: `https://www.orekit.org/site-orekit-8.0/apidocs/index.html` (visited on 11/04/2016).

Peterson, Erica, Robert Zee, and Georgia Fotopoulos (2008). "Possible Orbit Scenarios for an InSAR Formation Flying Microsatellite Mission". In:

Petropoulos, Anastassios E. (2005). "Refinements to the Q-law for low-thrust orbit transfers". In: *Advances in the Astronautical Sciences* 120, pp. 963–983.

Polites, Michael E. (1999). "Technology of automated rendezvous and capture in space". In: *Journal of Spacecraft and Rockets* 36.2, pp. 280–291.

Scharf, Daniel P., Fred Y. Hadaegh, and Scott R. Ploen (2004). "A survey of spacecraft formation flying guidance and control. part ii: control". In: *American Control Conference, 2004. Proceedings of the 2004*. Vol. 4. IEEE, pp. 2976–2985.

Schattel, Anne et al. (2016). "Low Thrust Trajectory Optimization for Autonomous Asteroid Rendezvous Missions". In:

Schaub, Hanspeter et al. (2000). "Spacecraft formation flying control using mean orbit elements". In: *Journal of the Astronautical Sciences* 48.1, pp. 69–87.

Schilling, K. et al. (2009). "Small satellite formations for distributed surveillance: system design and optimal control considerations". In: *NATO RTO Lecture Series SCI-209*.

Schilling, Klaus et al. (2015). "NetSat: A Four Pico/Nano.Satellite Mission for Demonstration of Autonomous Formation Flying". In: *Proceedings of the 66th IAC*. Jerusalem, Israel: IAF.

Schmidt, Marco et al. (2008). "Attitude determination for the Pico-Satellite UWE-2". In: *IFAC Proceedings Volumes* 41.2, pp. 14036–14041.

Schweighart, Samuel A. and Raymond J. Sedwick (2001). "Development and analysis of a high fidelity linearized J2 model for satellite formation flying". In: *SM Thesis, Massachusetts Institute of Technology, Dept. Aeronautics and Astronautics*.

Sengupta, Prasenjit (2007). "Dynamics and control of satellite relative motion in a central gravitational field". PhD thesis. Texas A&M University.

Sherrill, Ryan (2013). "Dynamics and Control of Satellite Relative Motion in Elliptic Orbits using Lyapunov-Floquet Theory". In:

Sholomitsky, G. (1977). "Infra-red space interferometer". In: *28th Int. Astro. Fed. Congress, 1977*.

Smith, Dan (1996). "Operations innovations for the 48-satellite globalstar constellation". In: *Proceedings of the 16th AIAA International Communications Satellite Systems Conference*. Vol. 542. Washington, DC: American Institute of Aeronautics and Astronautics.

Stipanović, Dušan M. et al. (2004). "Decentralized overlapping control of a formation of unmanned aerial vehicles". en. In: *Automatica* 40.8, pp. 1285–1296.

Szebehely, Victor and Giorgio EO Giacaglia (1964). "On the elliptic restricted problem of three bodies". In: *The Astronomical Journal* 69, p. 230.

Tillerson, Michael, Gokhan Inalhan, and Jonathan P. How (2002). "Co-ordination and control of distributed spacecraft systems using convex optimization techniques". In: *International Journal of robust and nonlinear control* 12.2-3, pp. 207–242.

Tschauner, J. and P. Hempel (1964). "Optimale Beschleunigungsprogramme für das Rendezvous-Manöver". In: *Astronautica Acta* 10.5-6, p. 296.

Ulybyshev, Yuri (1998). "Long-Term Formation Keeping of Satellite Constellation Using Linear-Quadratic Controller". en. In: *Journal of Guidance, Control, and Dynamics* 21.1, pp. 109–115.

Vallado, David A. and Salvatore Alfano (2011). "Curvilinear Coordinates for Covariance and Relative Motion Operations". In: Girdwood, AK, USA: Analytical Graphics Inc.

Varga, Gábor I. and José M. Sánchez Pérez (2016). "Many-Revolution low-thrust Orbit Transfer Computation using Equinoctial Q-Law including J2 and Eclipse Effects". In: *AIAA/AAS Paper*, pp. 15–590.

Walker, John G. (1984). "Satellite constellations". In: *Journal of the British Interplanetary Society* 37, pp. 559–572.

Walker, M. J. H., B. Ireland, and Joyce Owens (1985). "A set modified equinoctial orbit elements". In: *Celestial mechanics* 36.4, pp. 409–419.

Walter, H. G. (1967). "Conversion of osculating orbital elements into mean elements". In: *The Astronomical Journal* 72, p. 994.

Weisman, R. M., M. Majji, and K. T. Alfriend (2014). "Analytic characterization of measurement uncertainty and initial orbit determination on orbital element representations". In: *Celestial Mechanics and Dynamical Astronomy* 118.2, pp. 165–195.

Weisstein, Eric W. (2016). *Cylindrical Equidistant Projection*.

Yamada, Katsuhiko et al. (2012). "New state transition matrix for formation flying in J2-perturbed elliptic orbits". In: *Journal of Guidance, Control, and Dynamics* 35.2, pp. 536–547.

Yamanaka, Koji and Finn Ankersen (2002). "New State Transition Matrix for Relative Motion on an Arbitrary Elliptical Orbit". en. In: *Journal of Guidance, Control, and Dynamics* 25.1, pp. 60–66.